



저작자표시-비영리-변경금지 2.0 대한민국

이용자는 아래의 조건을 따르는 경우에 한하여 자유롭게

- 이 저작물을 복제, 배포, 전송, 전시, 공연 및 방송할 수 있습니다.

다음과 같은 조건을 따라야 합니다:



저작자표시. 귀하는 원저작자를 표시하여야 합니다.



비영리. 귀하는 이 저작물을 영리 목적으로 이용할 수 없습니다.



변경금지. 귀하는 이 저작물을 개작, 변형 또는 가공할 수 없습니다.

- 귀하는, 이 저작물의 재이용이나 배포의 경우, 이 저작물에 적용된 이용허락조건을 명확하게 나타내어야 합니다.
- 저작권자로부터 별도의 허가를 받으면 이러한 조건들은 적용되지 않습니다.

저작권법에 따른 이용자의 권리는 위의 내용에 의하여 영향을 받지 않습니다.

이것은 [이용허락규약\(Legal Code\)](#)을 이해하기 쉽게 요약한 것입니다.

[Disclaimer](#)

**Master of Environmental Engineering**

**Construction of Highly Efficient Graphitic Carbon Nitride Photocatalyst  
Based on Hard-template Approach Toward Degradation of Various Organic  
Pollutants**

**The Graduate School  
of the University of Ulsan**

**Department of civil and  
Environmental Engineering  
Seyedeh Maliheh Razavi Esfali**

**Construction of Highly Efficient Graphitic-carbon Nitride Photocatalyst  
Based on Hard-template Approach Toward Degradation of Various Organic  
Pollutants**

**Supervisor: Professor Lee, Byong-Kyu**

**A Dissertation**

**Submitted to**

**The Graduate School of the University of Ulsan in partial Fulfillment of the  
Requirements for the Degree of**

**Master of Engineering in Environmental Engineering**

**by**

**Seyedeh Maliheh Razavi Esfali**

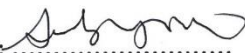
**Department of Civil and Environmental Engineering**

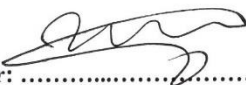
**Ulsan, Korea**


**January 2022**

**Construction of Highly Efficient Graphitic Carbon Nitride Photocatalyst  
Based on Hard-template Approach Toward Degradation of Various Organic  
Pollutants**

This certifies that the master thesis of  
Seyedeh Maliheh Razavi Esfali is approved.

Committee Chairman:   
Prof. Seok-Young Oh

Committee Member:   
Prof. Daeseung Kyung

Committee Member:   
Prof. Byeong-Kyu Lee

Department of Civil and Environmental Engineering

Ulsan, Korea

December, 2021

## Publications: Journals and conference

### List of published publications

Razavi-Esfali, M., Mahvelati-Shamsabadi, T., Fattahimoghaddam, H., & Lee, B. K. (2021). Highly efficient photocatalytic degradation of organic pollutants by mesoporous graphitic carbon nitride bonded with cyano groups. *Chemical Engineering Journal*, 419, 129503. (IF:13.273)



Highly efficient photocatalytic degradation of organic pollutants by mesoporous graphitic carbon nitride bonded with cyano groups

Maliheh Razavi-Esfali<sup>a</sup>, Tahereh Mahvelati-Shamsabadi<sup>a</sup>, Hossein Fattahimoghaddam<sup>a</sup>, Byeong-Kyu Lee<sup>a,\*</sup>

<sup>a</sup> Department of Civil and Environmental Engineering, University of Ulsan, Daehak-ro 93, Nam-gu, Ulsan 44610, Republic of Korea

### Publication ready to submit

A New Strategy for Fabrication of Uniform Washer-Ring-like Graphitic Carbon Nitride Using Hybrid Approach of Supramolecular Precursor and Hard Template for Efficient Photodegradation of Bisphenol A, Maliheh Razavi-Esfali, Byeong-Kyu Lee\*

### List of Conferences

**The 5<sup>th</sup> International Conference on Molecular Simulation (ICMS 2019)**, November 3-6, 2019, Jeju, Korea (As an attendance)

**The 4<sup>th</sup> International Conference on Bioresources, Energy, Environment, and Materials Technology (BEEM2020)**, September 6-9, 2020, Online conference, (Oral presentation)

**The 6<sup>th</sup> International Conference on Nanoscience and Nanotechnology (ICONN 2021)**, February 1-3, 2021, Virtual conference, (Poster presentation)

## Abstract

Annually different kinds of organic pollutants such as dyes, antibiotics, and phenol groups enter into the environment from various industries including pharmacies, food industries, and shrimp farming. These organic pollutants cause serious detrimental effects for humans, animals, and the whole ecosystem. Photocatalytic degradation of organic pollutants is recognized as a highly efficient method in the remediation of wastewater from these organic compounds. The energy source of photocatalysis is solar light which is an abundant, non-toxic, safe, and cheap energy resource. Among various photocatalysts, graphitic carbon nitride (g-C<sub>3</sub>N<sub>4</sub>), a two-dimensional conjugated polymer, has drawn broad attraction because of its several advantages including low in cost, metal-free, visible light active, and high stability. However, engineering a highly efficient g-C<sub>3</sub>N<sub>4</sub> is challenging and still in progress. One way to improve the activity of g-C<sub>3</sub>N<sub>4</sub> is to control its morphology, size and hence enhance its active reaction sites. In this study hard-templating approach was implemented in three different methods. Three different morphologies of graphitic carbon nitride were successfully synthesized with the aim of enhancing porosity, specific surface area, optical properties and generally, increasing photoactivity of graphitic carbon nitride as the photocatalyst. By using silica nanoclusters, mesoporous graphitic carbon nitride was fabricated which had high capability toward degradation of rhodamine B and tetracycline. By utilizing silica microspheres, hierarchical inverse opal graphitic carbon nitride was constructed with enhanced photoactivity in the degradation of rhodamine B and methylene blue. Finally, by combining supramolecular self-assembly approach and using silica as the hard-template, a novel morphology of washer-ring-like g-C<sub>3</sub>N<sub>4</sub> was achieved, with high ability in the degradation of bisphenol a.

*Keywords:* Photocatalysis, graphitic carbon nitride, pollutant degradation

## ACKNOWLEDGMENT

This research project would not have been possible without the support from countless of people. I want to give sincere gratitude to their kindness, patience, and support.

At first, I want to express my thanks to the professors in the Department of Civil and Environmental Engineering. They taught me a lot during the whole master course. Their encouraging words and detailed feedback during courses and seminars have been very crucial and helpful.

I am extremely thankful to my supervisor, Professor Byeong-Kyu Lee for his continuous supports, daily guidance, encouragement, and kindness during my master period. I am extremely grateful that I had the honor to be his master student.

I am grateful for my parents whose constant love and support keep me motivated and hard-worker. My achievements are because they believed in me. My father passed away during this project, but his support was continuous...

My deepest gratitude to my coach and best friend for the support, love, and guidance, not only in research, but also in every aspect of my life.

Then, I would like to thank all my laboratory members. I was fortunate to have been a part of AEERL group. They always provided kind help when I was in difficulties in daily life and always made the laboratory like a big warm home.

Finally, I would like to give my thanks to all my friends who directly and indirectly provided me inspiration and kindness.

## Table of Contents

Abstract.....	v
ACKNOWLEDGMENT.....	vi
List of Figures.....	xii
List of Tables.....	xviii
Chapter 1- Introduction.....	1
1.1 Organic Pollutants in Water.....	1
1.1.1 Persistent Organic Pollutant (Tetracycline).....	2
1.1.2 Organic Dyes (Rhodamine B, Methylene Blue).....	4
1.1.3 Precursors to fabricate polymer compounds (Bisphenol A).....	5
1.2 Different methods for wastewater treatment.....	6
1.3 Principles and mechanism of photocatalysis.....	9
1.4 Graphitic carbon nitride photocatalys.....	15
1.4.1 History of graphitic carbon nitride.....	15
1.4.2 Structure of graphitic carbon nitride.....	16
1.4.3 Different modification strategies for g-C <sub>3</sub> N <sub>4</sub> .....	19
1.4.3.1 Heteroatom doping.....	19
1.4.3.2 Heterojunction with other material.....	21
1.4.3.3 Nanostructure engineering.....	21
1.4.3.4 Defect engineering.....	21



1.5 Hard-template method .....	23
1.6 Research objective and steps .....	24
Chapter 2- Construction of mesoporous g-C <sub>3</sub> N <sub>4</sub> nanoclusters.....	26
2.1 Introduction.....	27
2.2 Experimental section.....	30
2.2.1 Chemicals.....	30
2.2.2 Preparation of g-C <sub>3</sub> N <sub>4</sub> samples .....	30
2.2.3 Characterization .....	31
2.2.4 Evaluation of the photocatalytic performance .....	32
2.3 Results and discussion .....	33
2.3.1 Synthesis mechanism.....	33
2.3.2 Morphologies and porous structure .....	34
2.3.2.1 Scanning Electron Microscopy (SEM) and Transmission Electron Microscopy (TEM) characterizations .....	34
2.3.2.2 Brunauer-Emmett-Teller (BET) analysis.....	35
2.3.3 Crystal structure and chemical composition .....	37
2.3.3.1 X-ray Diffraction (XRD) spectroscopy .....	37
2.3.3.2 Fourier Transform Infrared (FTIR) spectroscopy.....	38
2.3.3.3 Solid-state <sup>13</sup> C Magic Angle Spinning (MAS) NMR measurements .....	39
2.3.3.4 X-ray Photoelectron Spectroscopy (XPS) .....	40

2.3.3.5 Elemental Analysis (EA) .....	42
2.3.3.6 Electron Paramagnetic Resonance (EPR) .....	42
2.3.4 Optical properties and electronic band structure .....	44
2.3.4.1 UV–vis diffuse reflectance spectroscopy (DRS) .....	44
2.3.4.2 XPS valence band and bandgap structure .....	45
2.3.4.3 photoluminescence spectroscopy (PL) .....	47
2.3.5 Photoelectrochemical properties .....	47
2.3.6 Photocatalytic activity for degradation of RhB and TC: .....	48
2.3.7 Stability and reusability of catalysts .....	50
2.3.8 Determination of the main reactive species involved in the photocatalytic degradation	52
2.3.9 Mechanism of enhanced photocatalysis by NC MCN .....	55
2.3.10 Possible mechanism of photocatalytic degradation .....	56
2.3.11 Mineralization analysis .....	61
2.3.12 Toxicity evaluation .....	63
2.4 Conclusion .....	65
Chapter 3- Construction of Hierarchical Inverse Opal g-C <sub>3</sub> N <sub>4</sub> .....	67
3.1 Introduction .....	67
3.2 Experimental section .....	68
3.2.1 Synthesis of materials .....	68
3.2.1.1 Preparation of SiO <sub>2</sub> microspheres .....	68

3.2.1.2 Synthesis of inverse opal g-C <sub>3</sub> N <sub>4</sub> .....	69
3.2.2 Characterization .....	70
2.2.3 Evaluation of the photocatalytic performance .....	71
3.3 Results and discussion .....	72
3.3.1 SEM and TEM images.....	72
3.3.2 BET analysis .....	72
3.3.3 Crystal structure and chemical composition .....	74
3.3.4 Optical properties.....	75
3.4 Photodegradation results.....	76
3.4.1 Photocatalytic degradation of MB .....	76
3.4.2 Photocatalytic degradation of RhB .....	77
3.5 Conclusion .....	78
Chapter 4- A New Strategy for Fabrication of Uniform Washer-Ring-like Graphitic Carbon Nitride .....	
Nitride .....	80
4.1 Introduction.....	81
4.2 Experimental section.....	85
4.2.1 Preparation of silica microspheres .....	85
4.2.2 Preparation of inverse opal g-C <sub>3</sub> N <sub>4</sub> .....	85
4.2.3 Preparation of supramolecular precursor and 3D washer-ring-like g-C <sub>3</sub> N <sub>4</sub> .....	86
4.2.4 Photocatalytic degradation analysis.....	86

4.3 Results and discussion .....	87
4.3.1 Construction mechanism of the inverse opal g-C <sub>3</sub> N <sub>4</sub> .....	87
4.3.2 Construction mechanism of supramolecular precursor.....	88
4.3.3 XRD and FTIR results of supramolecular structure .....	89
4.3.4 Construction of washer-ring-like g-C <sub>3</sub> N <sub>4</sub> .....	91
4.3.5 Specific surface area and porous structure.....	93
4.3.6 Crystal structure and composition analysis.....	95
4.3.7 Optical properties and electronic band structure .....	100
4.3.8 Photoelectrochemical properties .....	105
4.3.9 Photocatalytic degradation assessment .....	107
4.3.10 Stability and recycling analysis .....	108
4.3.11 Detection of the main photogenerated reactive species.....	109
4.3.12 Unraveling the improved photodegradation of the DW CN photocatalyst.....	111
4.3.13 Suggested pathway for the transformation of BPA into byproducts .....	113
4.3.14 Toxicity evaluation and TOC removal analysis.....	118
4.4 Conclusions.....	123
Chapter 5- Conclusion .....	124
5.1 Suggestions .....	127
Chepter 5- Refernces.....	128

## List of Figures

<b>Figure 1-1.</b> The environment pollution caused by hazardous wastes [3].....	2
<b>Figure 1-2.</b> The chemical structure of tetracycline .....	2
<b>Figure 1-3.</b> Aquatic and terrestrial pathways of tetracycline in the ecosystem [6].....	3
<b>Figure 1-4.</b> Various industries that use organic dyes during product fabrication .....	4
<b>Figure 1-5.</b> Industries and related organic pollutant wastes.....	6
<b>Figure 1-6</b> Classification of technologies available for pollutant removal and examples of techniques [13].....	7
<b>Figure 1-7</b> Beautiful Sun.....	9
<b>Figure 1-8</b> Histogram if number of publications on photocatalysis (blue bars) and on photocatalysis with TiO <sub>2</sub> and C <sub>3</sub> N <sub>4</sub> (gray and yellow bars) from 2000 to 2019 [21] .....	10
<b>Figure 1-9</b> Schematic representation of major steps that photocatalysis reactions involve.....	12
<b>Figure 1-10</b> Band gap energies and conduction band (green) and valence band (red) edges positions of different semiconductors with respect to the vacuum level and NHE. The two dashed lines represents the water redox reaction potentials [24].....	14
<b>Figure 1-11</b> Developmental timeline of g-C <sub>3</sub> N <sub>4</sub> photocatalyst .....	15
<b>Figure 1-12</b> : Schematic illustration of (a) The stacked 2D layered structure of g-C <sub>3</sub> N <sub>4</sub> ;(b) s-triazine ; (b) tri-s-triazine units of g-C <sub>3</sub> N <sub>4</sub> [46].....	16

<b>Figure 1-13</b> Main routes for the synthesis of g-C <sub>3</sub> N <sub>4</sub> using different precursors [48].....	17
<b>Figure 1-14</b> , Reaction pathway of graphitic carbon nitride using cyanamide as the precursor [49] .....	18
<b>Figure 1-15</b> The redox potentials of the relevant reactions with respect to the estimated position of the g-C <sub>3</sub> N <sub>4</sub> band edges at pH 7 [46] .....	19
<b>Figure 1-16</b> ; Various modification strategies for g-C <sub>3</sub> N <sub>4</sub> -based photocatalyst [46] .....	20
<b>Figure 1-17</b> A schematic of nanocasting steps including infilling of a hollow (A1) or particulate (B1) template or coating (C1) of a template followed by removal of the template to leave inverse (A2) or hollow (B2, C2) replicas. ....	23
<b>Figure 1-18</b> Framework of this research .....	24
<b>Figure 1-19</b> A schematic representation of hard-templating method .....	25
<b>Figure 2-1</b> Synthesis procedure of NC MCN.....	31
<b>Figure 2-2</b> . SEM images of (a) SiO <sub>2</sub> clusters, (b) NC MCN, (c) Bulk CN; TEM images of (d, e, f, g, h) NC MCN .....	35
<b>Figure 2-3</b> . (a) N <sub>2</sub> adsorption/desorption isotherms (b) The corresponding pore size distribution curves of NC MCN and Bulk CN.....	36
<b>Figure 2-4</b> . X-ray diffraction (XRD) patterns.....	37
<b>Figure 2-5</b> . FTIR spectra of prepared catalysts.....	38
<b>Figure 2-6</b> . NMR spectra of as-obtained catalysts.....	39
<b>Figure 2-7</b> XPS spectra of Bulk CN and NC MCN samples, (a) survey; (b) C1s; (c) N1s. (d) EPR spectra of NC MCN and Bulk CN.....	41
<b>Figure 2-8</b> EPR spectra of NC MCN and Bulk CN .....	43
<b>Figure 2-9</b> Schematic atomic model of Bulk CN and NC MCN .....	43

<b>Figure 2-10</b> UV-Vis diffuse reflectance spectra of synthesized samples .....	44
<b>Figure 2-11</b> The corresponding $(\alpha hv)^2$ vs $h\nu$ plots of Bulk CN and NC MCN .....	46
<b>Figure 2-12</b> XPS valence band spectra (a) Bulk CN, (b) NC MCN; (c) Corresponding band edge positions of both catalysts.....	46
<b>Figure 2-13.</b> PL spectra of Bulk CN and NC MCN.....	47
<b>Figure 2-14.</b> (a) photocurrent response; (b) EIS Nyquist plots of as-prepared samples.....	48
<b>Figure 2-15.</b> Photocatalytic degradation curves of (a) Rhodamine B degradation, (b) Tetracycline degradation; pseudo-first-order kinetics curves of photocatalytic degradation for (c) Rhodamine B, (d) Tetracycline.....	50
<b>Figure 2-16.</b> Photocatalytic stability of NC MCN in the degradation of TC within eight cycles	51
<b>Figure 2-17.</b> SEM image of (a) Unused NC MCN and (b) used NC MCN.....	52
<b>Figure 2-18.</b> XRD patterns of fresh NC MCN and used NCMCN .....	52
<b>Figure 2-19.</b> (a) TC photodegradation percent using NC MCN in the presence of different scavengers; EPR spectra recorded with NC MCN under dark and visible light illumination depicting (b) DMPO $\cdot O_2^-$ adducts in methanol solution, (c) DMPO $\cdot OH$ adducts in aqueous solution.....	54
<b>Figure 2-20.</b> Schematic illustration of TC and RhB photocatalytic degradation over the NC MCN .....	56
<b>Figure 2-21.</b> LC-MS chromatograms of (a) TC; and produced intermediates at (b) photodegradation reaction time 15 min;(c) photodegradation reaction time 30 min;(d) comparison of TC intensity without reaction and after 15 min reaction time .....	59
<b>Figure 2-22.</b> Proposed intermediate production pathways during photodegradation of TC.....	60

<b>Figure 2-23.</b> (a) Removal of TOC as a function of time for tetracycline degradation using as-prepared photocatalysts, Spectra of TCs photodegradation solutions at different reaction time: (b) -60 to 0 min; (c) 0-30 min; (d) 30-90 min .....	62
<b>Figure 2-24.</b> Molecular structures of the tetracycline .....	62
<b>Figure 2-25.</b> Toxicity assessment results of TC intermediates produced under photocatalytic degradation using NC MCN (a) acute toxicity LD <sub>50</sub> ; (b) Bioaccumulation factor; (c) developmental toxicity (d) mutagenicity .....	64
<b>Figure 3-1.</b> Schematic illustration of SiO <sub>2</sub> microsphere synthesis .....	68
<b>Figure 3-2.</b> Schematic illustration of inverse opal g-C <sub>3</sub> N <sub>4</sub> synthesis.....	69
<b>Figure 3-3.</b> SEM and TEM images of synthesized samples .....	73
<b>Figure 3-4.</b> (a) N <sub>2</sub> adsorption/desorption isotherms (b) The corresponding pore size distribution curves Bulk CN.....	73
<b>Figure 3-5.</b> (a) X-ray diffraction (XRD) patterns, (b) FTIR spectra.....	75
<b>Figure 3-6.</b> (a) UV–Vis diffuse reflectance spectra; (b) the corresponding $(\alpha h\nu)^2$ vs $h\nu$ plots of prepared samples.....	76
<b>Figure 3-7.</b> (a) UV–Vis absorbance spectra of MB; (b) Photocatalytic degradation curves of MB .....	77
<b>Figure 3-8.</b> (a) UV–Vis absorbance spectra of RhB; (b) Photocatalytic degradation curves of RhB .....	78
<b>Figure 4-1.</b> The SEM images of (a) SiO <sub>2</sub> microspheres with an average size of 300 nm, (b, c) IO CN, (d) Bulk CN; TEM images of (e, f) IO CN .....	88
<b>Figure 4-2.</b> SEM images of (a) pure melamine, (b, c) supramolecular precursor after 24 h hydrothermal reaction time .....	89



<b>Figure 4-3.</b> (a) FTIR spectra of pure melamine and the supramolecular precursor; (b) XRD patterns of pure melamine and supramolecular precursor .....	90
<b>Figure 4-4.</b> The SEM images of (a, b) SM CN; (c, d, e, f) DW CN .....	92
<b>Figure 4-5.</b> TEM images of DW CN.....	92
<b>Figure 4-6.</b> Schematic representation of the synthesis IO CN, supramolecular precursor, DW CN, and SM CN.....	93
<b>Figure 4-7.</b> (a) N <sub>2</sub> adsorption-desorption isotherms; (c) The correlated pore size distribution plots of as-prepared samples.....	94
<b>Figure 4-8.</b> (a) XRD diffraction patterns, (b) FTIR spectra, (c) NMR spectra of as-prepared catalysts.....	96
<b>Figure 4-9.</b> High resolution XPS spectra of as-prepared catalysts, (a) survey; (b) N1s; (c,d) C1s .....	98
<b>Figure 4-10.</b> Schematic atomic model of triazine structure of g-C <sub>3</sub> N <sub>4</sub> with and without defects .....	100
<b>Figure 4-11.</b> UV-vis diffuse reflectance pattern of prepared photocatalysts .....	101
<b>Figure 4-12.</b> Optical band gaps of the as-synthesized g-C <sub>3</sub> N <sub>4</sub> catalysts achieved by Tauc plots .....	102
<b>Figure 4-13.</b> XPS valence band spectra of as-prepared catalysts .....	104
<b>Figure 4-14.</b> Schematic illustration of band edge positions of synthesized catalysts .....	104
<b>Figure 4-15.</b> PL spectra of synthesized samples .....	105
<b>Figure 4-16.</b> (a) photocurrent response; (b) EIS Nyquist plots of synthesized samples .....	106

<b>Figure 4-17.</b> (a) Comparison of the photodegradation efficiency of as-prepared photocatalysts toward degradation of BPA; (b) pseudo-first-order kinetic plots of BPA photodegradation for all 4 samples.....	108
<b>Figure 4-18.</b> Photocatalytic stability of DW CN in the degradation of BPA repeated for six cycles.....	109
<b>Figure 4-19.</b> SEM image of used DW CN.....	109
<b>Figure 4-20.</b> BPA photodegradation percent utilizing DW CN and in the existence of various scavengers.....	111
<b>Figure 4-21.</b> Schematic representation of BPA photodegradation using 3D ring-like DW CN	113
<b>Figure 4-22.</b> LC-MS chromatograms of (a) BPA; (b) after 15 min; (c) after 30 min; (d) after 45 min; € after 60 min; (d) after 75 min photodegradation reaction time .....	115
<b>Figure 4-23.</b> Comparison of BPA intensity before the reaction and after 15, 30, 45, and 60 min photocatalytic reaction obtained based on LC-MS chromatograms.....	115
<b>Figure 4-24.</b> Proposed BPA photodegradation routes by the DW CN photocatalyst.....	116
<b>Figure 4-25.</b> The predicted toxicity measurements of BPA and its photodegradation intermediates using ECOSAR.....	120
<b>Figure 4-26.</b> Toxicity analysis results (a) developmental toxicity; (b) mutagenicity; (c) bioaccumulation factor of BPA and produced intermediates .....	122
<b>Figure 4-27.</b> Removal of TOC as a function of time for BPA degradation using DW CN.....	122

## List of Tables

<b>Table 1-1:</b> Main advantages and disadvantages of various Advanced Oxidation Processes [17].	8
<b>Table 2-1.</b> BET surface area, average BJH pore size, and pore volume of NC MCN and Bulk CN .....	36
<b>Table 2-2.</b> XPS N1s deconvolution result of Bulk CN and NC MCN.....	41
<b>Table 2-3.</b> Elemental analysis for Bulk CN and NC MCN.....	42
<b>Table 3-1</b> BET results .....	74
<b>Table 4-1</b> BET results .....	95
<b>Table 4-2</b> XPS N1s deconvolution result of SM CN and DW CN. ....	98
<b>Table 4-3.</b> XPS N1s deconvolution result of Bulk CN and IO CN.....	99
<b>Table 4-4</b> Elemental analysis for Bulk CN, IO CN, SM CN, and DW CN .....	100
<b>Table 4-5</b> Products detected by LC-MS.....	117
<b>Table 4-6</b> Acute toxicity obtained using ecological structure activity relation- ships (ECOSAR) model.....	120
<b>Table 4-7</b> Chronic toxicity obtained predicted by ecological structure activity relation- ships (ECOSAR) model.....	121

<b>Table 4-8</b> Summary of toxicity assessment indices produced by quantitative structure-activity relationship (QSAR) models.....	121
---	-----

# Chapter 1- Introduction

## 1.1 Organic Pollutants in Water

Life of plants, animals, human and the whole ecosystem depends on water. Rapid growing of worldwide population along with industrialization give rise to the increased demand of water consumption. There is a limitation in the accessible usable water resources, and higher than one-third of them is being used for industrial, agricultural, and residential utilization [1]. Thus, even the limited accessible clean water turned to the wastewater, as a result of the existence of various pollutants and contaminants including persistent organic pollutants, dyes, etc. Therefore, the availability and accessibility of fresh and high-quality water became a crucial and controversial problem all around the world, recently [2]. In here, four important pollutants that are very hazardous for the environment are explained.



**Figure 1-1.** The environment pollution caused by hazardous wastes [3]

### 1.1.1 Persistent Organic Pollutant (Tetracycline)

Persistent organic pollutants (POPs) are among toxic organic materials that have distinct physical and chemical characteristics. When they are released into the environment, they persist to stay unchanged for a long time and travel long distances over water, before being converted into less hazardous chemicals [4]. Thus it is highly probable that these materials bio-accumulate in the food chain and end up in wildlife and animal bodies, resulting in adverse health impacts [5]. Tetracycline derivatives, a recognized class of antibiotics, is a type of POP that have been considerably utilized in the fabrication of human and veterinary medicine because it has low fabrication prices and high quality.[4]. Tetracycline is composed of four connected rings with hydroxyl, methyl, ketone, and dimethylamino functional groups [6] as shown in Figure 1-2.

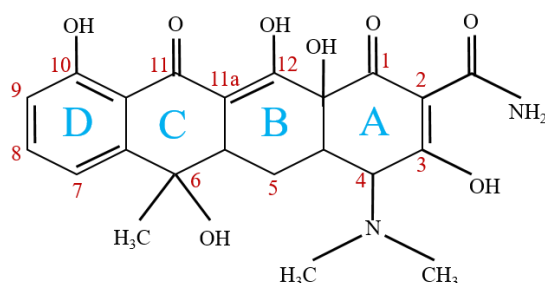


**Figure 1-2.** The chemical structure of tetracycline

Although TC possess different advantages for human and animal health, their widespread usage causes considerable fluctuations in environmental microflora. Metabolization of TC is hard for human and animal digestion set-up, and when this medicine is used, only small part of it could get absorbed by human and animal bodies and large amount of these antibiotics can be released into water streams (ground-water, surface-water, wastewater) as un-metabolized parent chemical. Besides that, hospitals, pharmaceutical factories, and livestock also play an important role in the augmentation of TC in the wastewater systems. Figure 1-3 represents the aquatic and terrestrial pathways of tetracycline in the ecosystem.

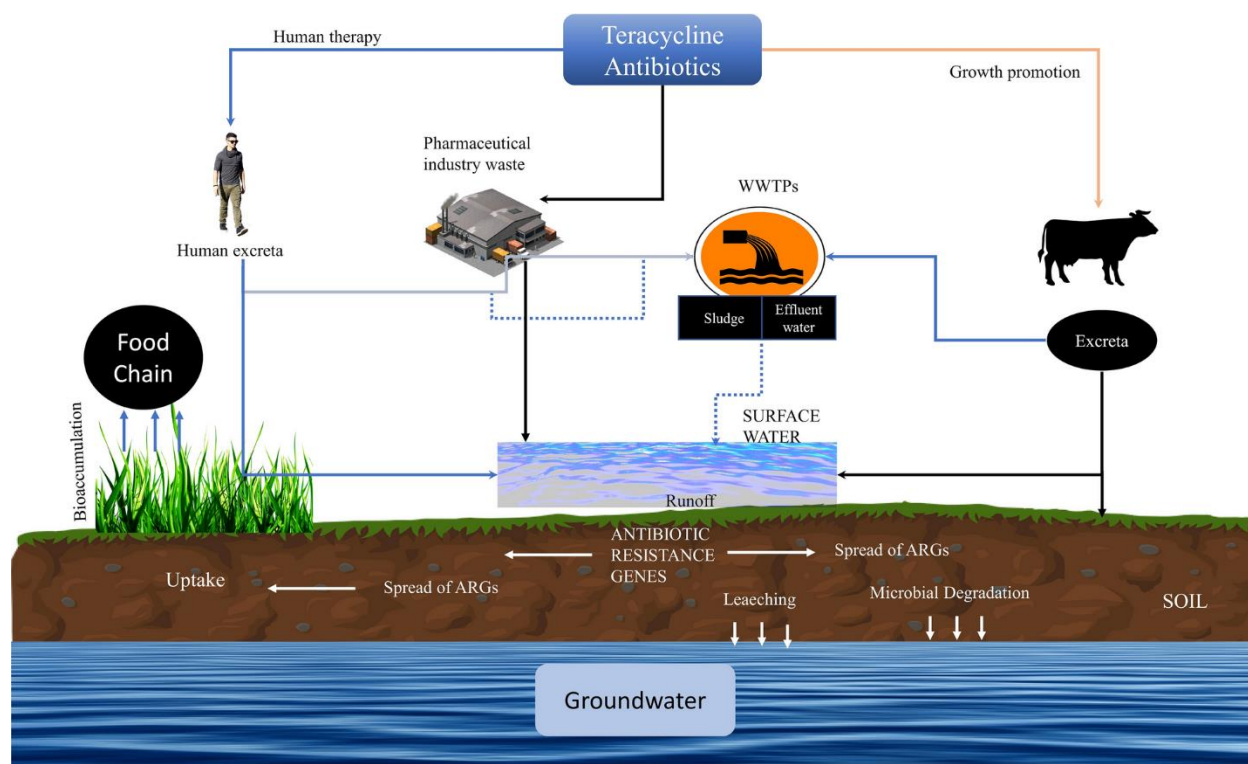


**Figure 1-3.** Aquatic and terrestrial pathways of tetracycline in the ecosystem [6]

Tetracycline is persistent and difficult to degrade in the environment, thus is detected in wastewater, surface water, groundwater, sludge, and sediments notably [6]. prolonged hazardous impacts of

TC would result in ecological imbalance because of low degradation of TC in the current treatment processes. It is of great importance to consider TCs as an important environmental contamination as it considerably affects human wellness because of the expansion of bacterial resistance.

### 1.1.2 Organic Dyes (Rhodamine B, Methylene Blue)

Organic dyes are another type of organic pollutants that are extensively utilized in different industries such as textiles, papers, leathers, food, and cosmetics industries (Figure 1-4). More than 10000 kinds of dyes are commercially utilized and the annual fabrication is more than 0.7 billion tons [7]. Discharge of synthetic dyes from washing cycles of industries into natural water bodies causes serious environmental troubles because they are highly toxic and are accompanied by production of several potential carcinogens.

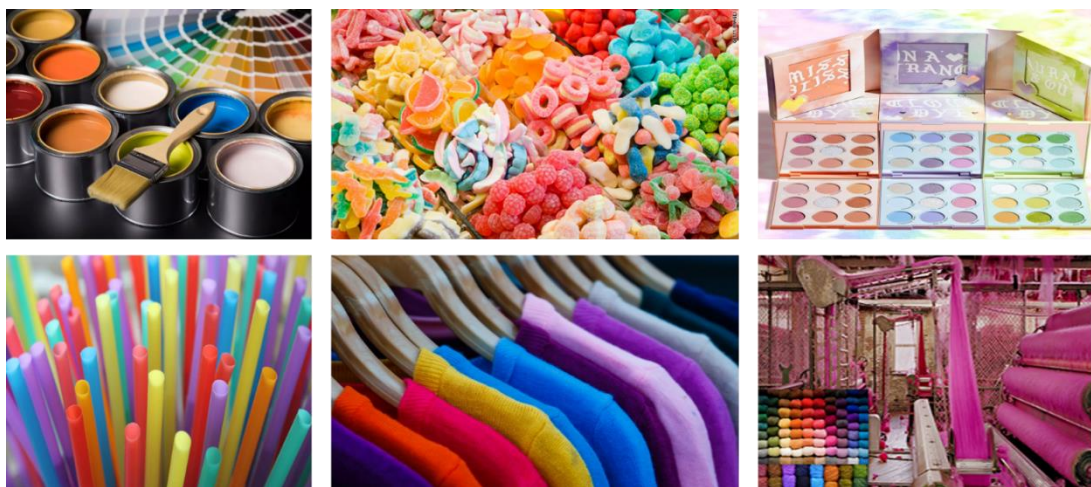


**Figure 1-4.** Various industries that use organic dyes during product fabrication

Rhodamine B (RhB), an organic dye with beautiful red–orange color and low-cost, is commonly used in textile and food manufacturing. According to a declaration from the European Food Safety Authority (EFSA), RhB was evaluated as potentially both carcinogenic and genotoxic, and detrimental for humans, animals, as well as the whole ecosystem [8].



Methylene blue with the chemical formula  $C_{16}H_{18}N_3SCl$  is green and solid at room temperature and becomes blue after being dissolved in water. Like RhB, this dye also has enormous industrial applications. When this chemical is released to the water bodies, it absorbs light because of having dark blue color, and so block underneath water environment, and so the beneath water never achieve light. This is detrimental for aquatic life and ecosystem. Furthermore, smelling of MB might result in breath hazards and direct contact may cause hazardous injuries to human eyes, burning, nausea, vomiting, hyperhidrosis, and mental disorders [9].

### **1.1.3 Precursors to fabricate polymer compounds (Bisphenol A)**

Bisphenol A (2,2-bis(4-hydroxyphenyl) propane, BPA) is a well-known precursor that is widely used in the fabrication of polymer compounds, including polycarbonates, epoxy resins, etc. [10]. The widespread use of BPA in plastic products and the inappropriate disposal and waste management made this chemical ubiquitous in numerous water systems. As a result, BPA is frequently detected in industrial and municipal wastewater [11]. In addition, BPA has previously been reported to be a typical endocrine disruptor (EDC). Furthermore, even low levels of exposure to this chemical are accompanied by adverse health effects on aquatic wildlife and human beings [12]. Figure 1-5 shows different industries that uses four target pollutants, in their production, treatment, or meditation processes.



**Figure 1-5.** Industries and related organic pollutant wastes

## 1.2 Different methods for wastewater treatment

Thus all these industries produce wastewater containing mentioned contaminants and release them to the environment which cause severe health effects for the whole ecosystem. To deal with the unfortunate water scarcity, treatment and recycling of water streams is of great significance and the need to develop efficient methods of treating wastewater and removing these hazardous pollutants is beyond question.

To address this issue, several methods are available. Generally, conventional wastewater treatment includes a collection of physical, chemical and/or biological procedures to eliminate organic pollutants from effluents. A multitude of techniques categorized in conventional methods, established recovery processes and emerging removal methods can be utilized [13] as shown in Figure 1-6. Each method has its own disadvantages in terms of cost, feasibility, efficiency, practicability, reliability, environmental impact, operation difficulty, pre-treatment requirements and the formation of potentially toxic by-products. Many of these methods such as adsorption, ion-exchange, biomass, filtration have been often suffering from limitations such as low removal

efficiencies, incomplete degradation to nontoxic substances, and long removal times with the necessity of post-treatment [14].

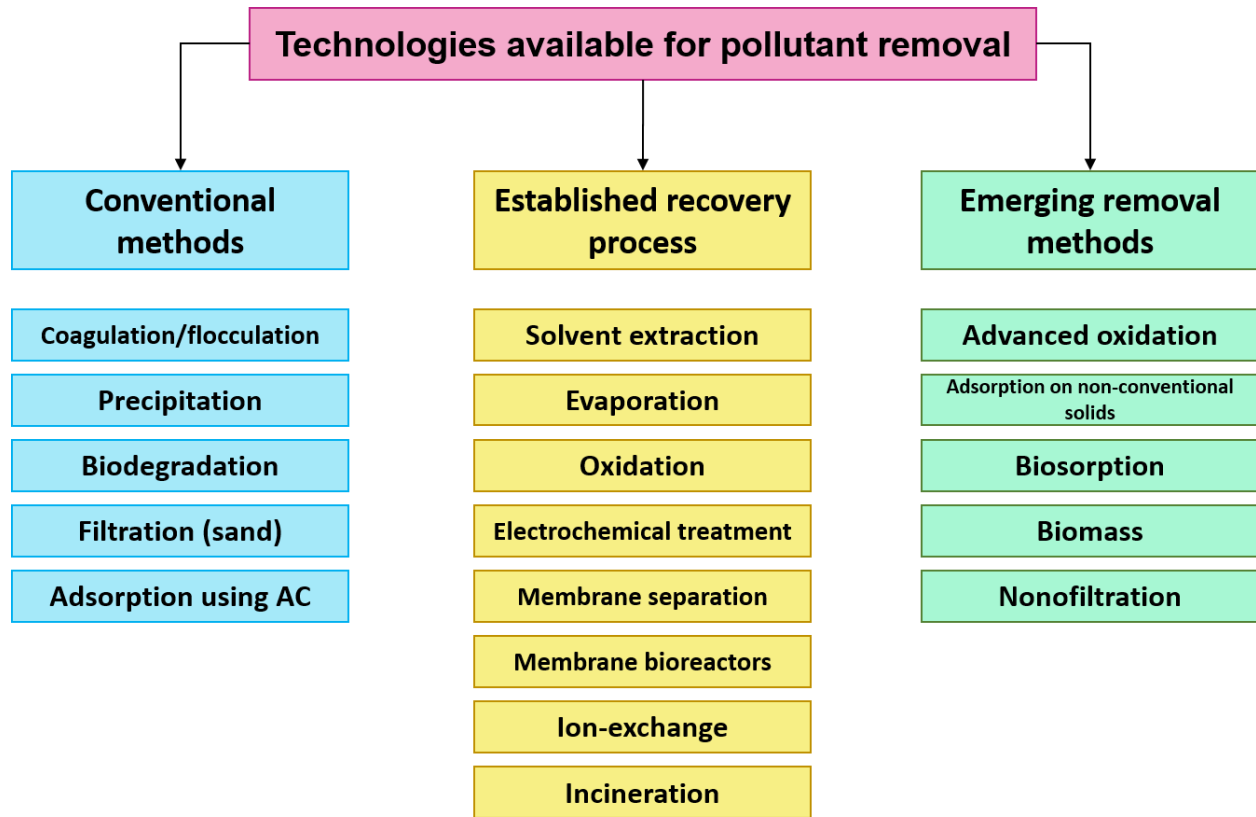


**Figure 1-6** Classification of technologies available for pollutant removal and examples of techniques [13]

In recent years, as an alternative to nondestructive water treatment methods, efficient advanced oxidation processes (AOPs) were used to remove a wide range of industrial pollutants in aqueous solutions. AOPs are based on the in-situ production of highly active radical species aimed at degrading organic compounds [15, 16]. Table 1-1 summarizes the advantages and disadvantages of the advanced oxidation processes methodologies that are applicable in wastewater treatment [17]. Among these AOPs, photocatalytic degradation by semiconductor catalysts has been

considered a notable method to deal with hazardous contaminants because it is simple in design, renewable, low in cost, nontoxic, and environmentally benign treatment technology [18]. Semiconductor photocatalysts contain potential capability in environmental wastewater remediation and solar energy conversion since the initiative research of Fujishima and Honda who used TiO<sub>2</sub> for hydrogen generation by water photoelectrolysis in 1972 [19]. Every year, approximately an amount of  $3 \times 10^{24}$  J energy is delivered to the surface of our planet from sun, which is 4 orders of magnitude higher than the energy requirement of people in every spot of the universe [20]. Sunlight is ubiquitous, clean, and harmless, thus, efficient harvesting and transformation of sunlight using photocatalysts could solve too many of challenges we face in different energy and environmental sectors. In the following section, basic principles of photocatalysis and mechanism of photocatalytic degradation of organic pollutants is explained.

**Table 1-1:** Main advantages and disadvantages of various Advanced Oxidation Processes [17].

AOP	Advantage(s)	Disadvantage(s)
Ozonation	Powerful oxidation technique oxidizes a large number of organic and inorganic materials.	More complex technology and requires high capital/operational cost. High electric consumption.
UV	An effective method that typically does not leave any byproducts which are harmful to the environment.	Less effective if the wastewater has high amounts of particulates which can absorb UV light.
UV/H <sub>2</sub> O <sub>2</sub>	An effective technique in the oxidation and mineralization of most organic pollutants. Ease of formation of ·OH radicals.	Less effective, when the wastewater has high absorbance. High operational cost.
O <sub>3</sub> /UV/H <sub>2</sub> O <sub>2</sub>	Most effective process due to the fast generation of ·OH radicals. Can treat a wide variety of contaminants.	Needs to compete with high turbidity, solid particles, and heavy metal ions in the aqueous stream. High operational cost.
Fenton reaction	Simple process.	Production of sludge iron waste and handling

	Easy availability of chemicals.	the waste pose logistical problems.
Photo-Fenton reaction	Reduction of sludge iron waste compared to original Fenton reaction. Effective and fast degradation.	Needs a controlled pH medium for better performance.
	Long-term stability at high temperature.	Could form byproducts that can be harmful to the environment.
Photocatalysis	Resistance to attrition. Low-cost and environmentally benign treatment technology.	Requires efficient catalysts that can absorb in the visible region.

### 1.3 Principles and mechanism of photocatalysis



**Figure 1-7** Beautiful Sun

“Here comes the sun, and I say it’s alright” the line from beautiful Beatles’ song.

Our existence as well as having sustainable world, depends on the sun. Until the sun shines in the sky, there is always hope to heal a universe which is going through more and more pollution (water, air, and soil), and also higher demands for energy. Every year, approximately an amount of  $3 \times 10^{24}$

J energy is delivered to the surface of our planet from sun, which is 4 orders of magnitude higher than the energy requirement of people in every spot of the universe [20]. In this regard, many researchers and scientists have always tried to harvest the sun in an efficient way. Among all these efforts, in 1972, Fujishima and Honda began a journey by publishing a paper in which they used  $\text{TiO}_2$  for hydrogen generation by water photoelectrolysis [19]. This was a starting point of a long adventure on semiconductor photocatalysis reactions. From that day forward, many researchers entered this expedition and invested a huge amount of time, resources, and intellectual exercise to profoundly explore the process of photocatalyst. Accordingly, the fast-growing number of finding on photocatalysis comes as no surprise, that are together with an increased number of publications with an annual exponential growth. (Figure 1-8). In the field of environmental wastewater treatment, by using sunlight, photocatalysis process can directly decompose many organic pollutants into small nontoxic molecules,  $\text{CO}_2$ , and  $\text{H}_2\text{O}$  and mitigate pollution. Thus, Photocatalysis is a green and cost-effective method, that completely fulfills the prerequisites of sustainable advancements for our modern society and profound investigation of its potential application is highly essential.

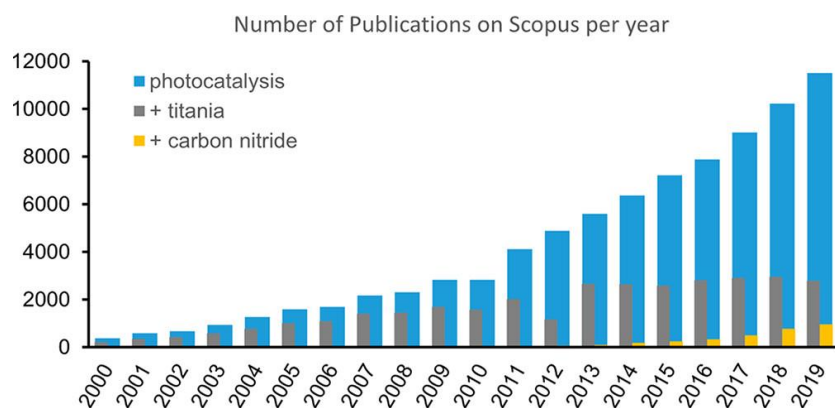


**Figure 1-8** Histogram if number of publications on photocatalysis (blue bars) and on photocatalysis with  $\text{TiO}_2$  and  $\text{C}_3\text{N}_4$  (gray and yellow bars) from 2000 to 2019 [21]

In a semiconductor as photocatalyst, the energy band structure is composed of valence band (VB) which is full of electrons, and higher energy conduction band (CB) that is free of electrons. The size of distance among VB and CB is named band gap, which is specific characteristic of every individual semiconductor. Photocatalysis reaction can be started upon absorption of photons with energy ( $E=h\nu$  which E is the energy of photon, h is plank constant, and  $\nu$  is the frequency) equal or higher than the semiconductor band gap. After absorption of photons, the electrons ( $e^-$ ) in the valence band are promoted to the conduction band and leave a hole ( $h^+$ ) in the VB. The excited electrons in the CB and the holes in the VB can either recombine, get trapped in surface states, or react with electron donors or acceptors at or in the immediate vicinity of the semiconductor surface. This capability to donate and accept electrons, can cause redox reactions at a surface and is the fundamental principle of heterogeneous photocatalysis [22].

Generally speaking, the photocatalysis process contains seven main steps, that could be essentially categorized in four major parts:

**Part 1:** light harvesting and photon absorption (step 1)

**Part2:** Charge excitation (step 2)

**Part 3:** photogenerated charge separation and transportation (steps 3, 4, and 5)

**Part 4:** Redox reactions between photogenerated charges and surface chemical species (steps 6, 7)

These steps are schematically represented in Figure 1-9.

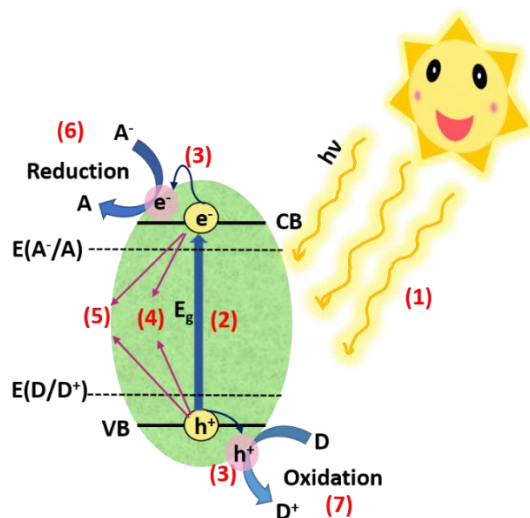


**Figure 1-9** Schematic representation of major steps that photocatalysis reactions involve

The photo-generated holes ( $h^+$ ) are strongly active and has high oxidation power that can oxidize adsorbed  $H_2O$  and  $OH^-$  on the surface of semiconductor to hydroxyl radicals ( $\bullet OH$ ). These hydroxyl radicals with high oxidation potential will further react with pollutants and oxidize them into smaller byproducts. Simultaneously, the hole ( $h^+$ ) also can grab the electrons from organic pollutants adsorbed on the surface of photocatalyst, and decompose them to smaller molecules [22]. Thus, based on mentioned series of oxidation reactions, the organic pollutant adsorbed on the surface of photocatalyst would be degraded into small intermediates and finally to water and carbon dioxide. On the other hand, the electrons in the conduction band have strong reduction ability and cause some reduction reactions to happen. These electrons can participate in  $CO_2$  reduction and reduce them to hydrocarbons, useful chemicals for various industries.  $CO_2$  is a greenhouse gas, and conversion of this gas to applicable materials is so beneficial for our environment. Series of redox reactions that happen in the presence of photocatalyst are shown in the following equations [23]:



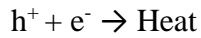
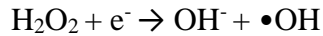
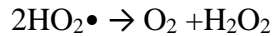
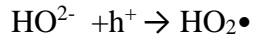
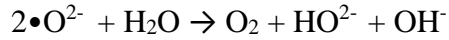
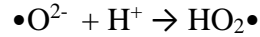
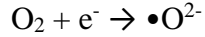
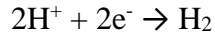
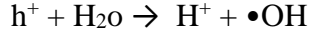
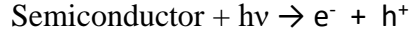
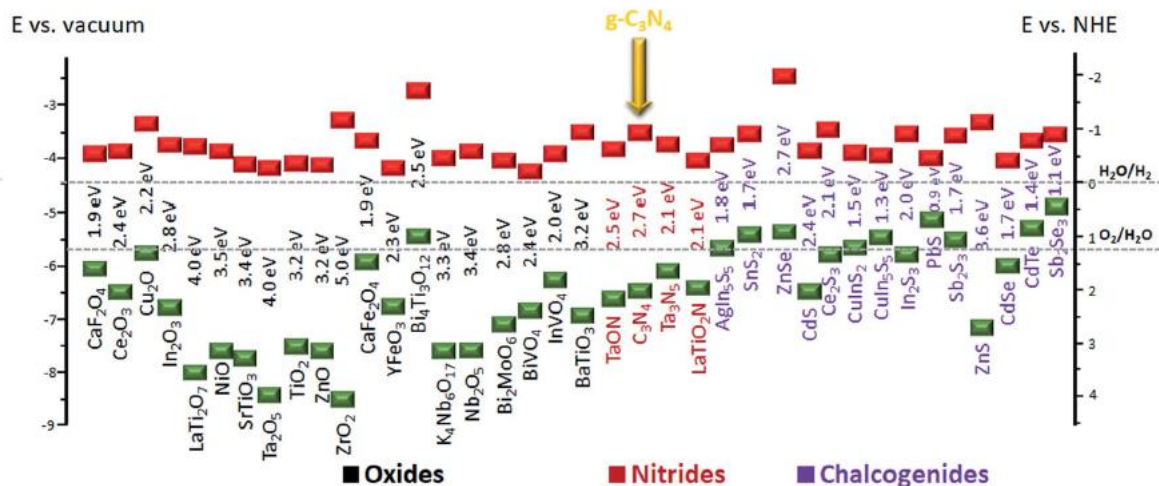


Figure 1-10 shows the bandgaps and the VB and CB positions of some oxides, nitrides and chalcogenides semiconductor photocatalysts, which are appropriate for different applications [24]. Between the various studied photocatalysts, TiO<sub>2</sub> semiconductor, has been considered numerously as an outstanding photocatalyst in different applications including degradation of various volatile organic compounds (VOCs), dyes and water contaminants as well as hydrogen and oxygen evolution reactions (HER and OER), CO<sub>2</sub> reduction and conversion to hydrocarbon fuels and some other energy-related applications [25-27]. Approximately half of the papers connected to photocatalyst or photocatalysis includes using TiO<sub>2</sub> semiconductor. Nevertheless, TiO<sub>2</sub> photocatalysts are only active under UV-light, due to having a wide bandgap, which is higher than 3.0 eV. This intrinsic characteristic inhibits its additional pragmatic applications. The reason is that the UV light only accounts for lower than 5% of the entire solar irradiation, and the

considerable segment of the solar energy spectrum (54.1%) is in the visible region. At the same time, other various inorganic metal oxides (including ZnO [26-28], SnO<sub>2</sub> [29, 30], ZrO<sub>2</sub> [31, 32], NiO [33, 34]) also have aforementioned optical absorption limitation. Metal sulfides such as ZnS is vulnerable to photocathode corrosion, which influences its function and lifetime and is hence not the excellent photocatalytic semiconductor. Consequently, the construction of an efficient polymeric semiconductor which is active under visible-light irradiation is of great necessity and urgency and has stimulated modern scientists for further research [35-37]. Among numerous reported photocatalysts, graphitic carbon nitride (g-C<sub>3</sub>N<sub>4</sub>), has been considered to be a promising candidate to fulfill the mentioned prerequisites which will be scrutinized in the next section.



**Figure 1-10** Band gap energies and conduction band (green) and valence band (red) edges positions of different semiconductors with respect to the vacuum level and NHE. The two dashed lines represents the water redox reaction potentials [24].

## 1.4 Graphitic carbon nitride photocatalys

### 1.4.1 History of graphitic carbon nitride

At 1830, by pyrolysis of mercury (II) thiocyanate, Jöns Jakob Berzelius achieved a polymeric material and stated it as heptazines. At 1834, Hestus von Liebig called the polymer substance as ‘melon’ [38]. Many years later, at 1922, Edward Curtis Franklin figured out that when melon goes through calcination, a carbon nitride polymer is achieved, which he named it as  $(C_3N_4)_x$ . Nevertheless, because of the lack of advanced characterization techniques at that time, Edward just expressed the possible structure of  $(C_3N_4)_x$ , without real corroboration and confirmation of this structure [39]. Later on, at 1937, Linus Pauling by using X-ray spectroscopy confirmed that Liebig’s melon is a polymeric substance composed of tri-s-triazine backbone bonded with amine groups [40]. At 1980, Ramachandra S. Hosmane synthesized heptazine  $C_6N_7H_3$  [41]. After a decade, in 1990, by comparison of the hardness of  $\beta$ - $C_3N_4$  with that of diamond using theoretical investigation, the studies on  $C_3N_4$  was resumed. From then on, various allotropes of carbon nitride including  $\alpha$ - $C_3N_4$ ,  $\beta$ - $C_3N_4$ , graphitic- $C_3N_4$ , cubic- $C_3N_4$ , and pseudo-cubic- $C_3N_4$  were discovered and each of them have different properties. All of them contain covalently bonded carbon and nitrogen which is a strong bond [42, 43].

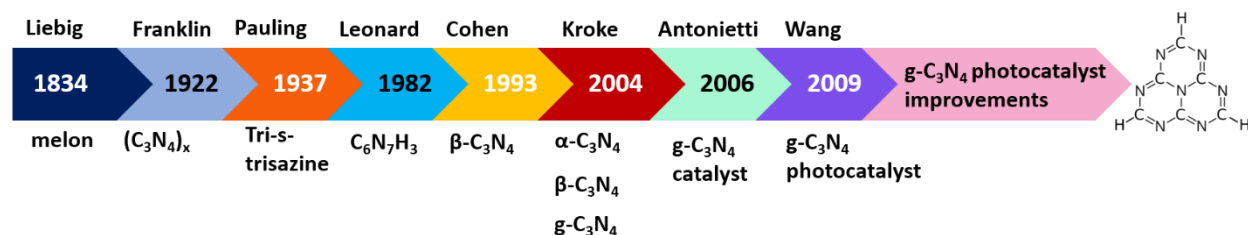


**Figure 1-11** Developmental timeline of  $g$ - $C_3N_4$  photocatalyst

Among different allotropes of carbon nitride, graphitic phase ( $g\text{-C}_3\text{N}_4$ ) has the most stable structure at room temperature. This allotrope was initially used as an effective metal-free catalyst in Friedel-Crafts reactions to activate benzene by Markus Antonietti's group [44]. Three years after this pioneering research, Dr. Xinchun Wang utilized  $g\text{-C}_3\text{N}_4$  as a polymeric photocatalyst in  $\text{H}_2$  evolution reaction for the first time [45]. This was a milestone in the field of photocatalysis and played a significant role in the advancement of artificial photosynthesis.

#### 1.4.2 Structure of graphitic carbon nitride

$g\text{-C}_3\text{N}_4$  is a conjugated polymer and has graphitic-like layered structure composed of  $sp^2$  hybridized bonded carbon and nitrogen.  $g\text{-C}_3\text{N}_4$  is constructed from  $\text{C}_3\text{N}_4$  rings that are bonded to each other by nitrogen atoms in two different forms of s-triazine or tri-s-triazine units, as shown in Figure 1-12.

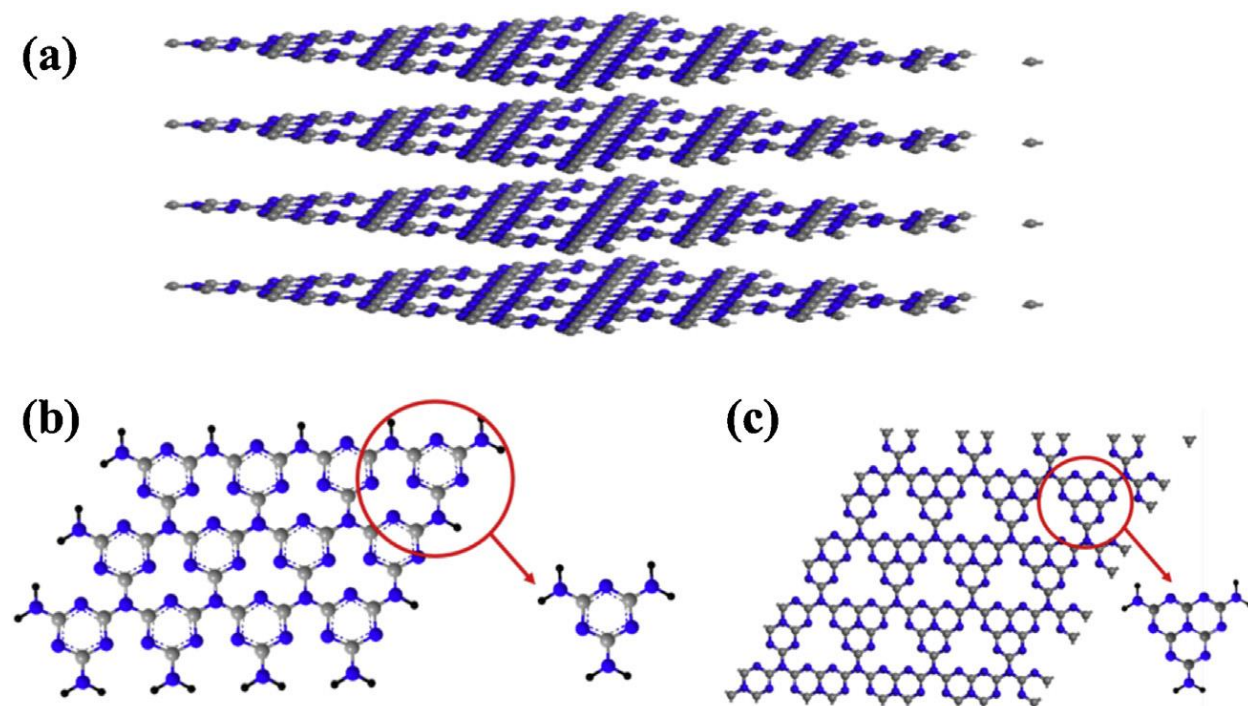


**Figure 1-12** : Schematic illustration of (a) The stacked 2D layered structure of  $g\text{-C}_3\text{N}_4$ ; (b) s-triazine ; (c) tri-s-triazine units of  $g\text{-C}_3\text{N}_4$  [46]

The atoms in the layers are positioned in honeycomb arrangement with strong covalent bonds, and the force among the two dimensional (2D) layers is the weak van der Waals force [24]. Different C and N-rich precursors including melamine, cyanamide, dicyandiamide, urea, thiourea, and so on have been used for the synthesis of g-C<sub>3</sub>N<sub>4</sub> (Figure 1-13 ) [47]. The final optical, electrical and morphological structure of g-C<sub>3</sub>N<sub>4</sub> is greatly influenced by the type of initial precursor, which will be discussed in detail in future chapters. Figure 1-14 shows the reaction pathway of graphitic carbon nitride started from cyanamide as the precursor.

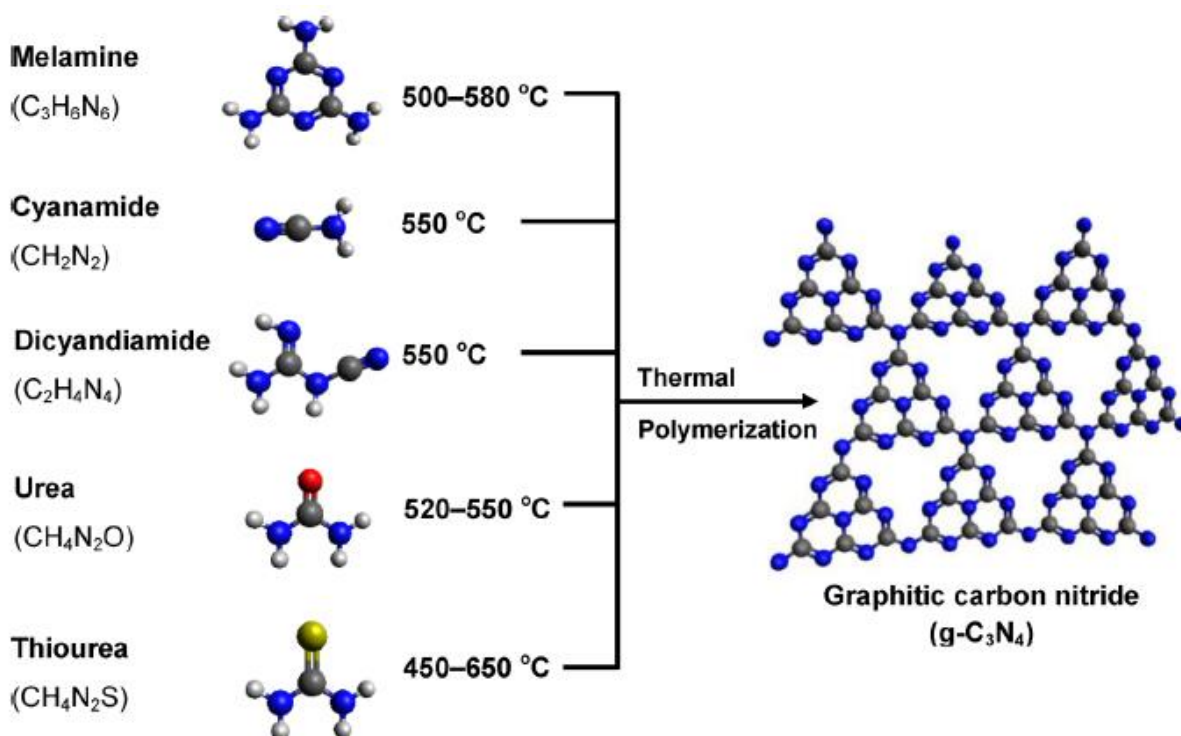


**Figure 1-13** Main routes for the synthesis of g-C<sub>3</sub>N<sub>4</sub> using different precursors [48]

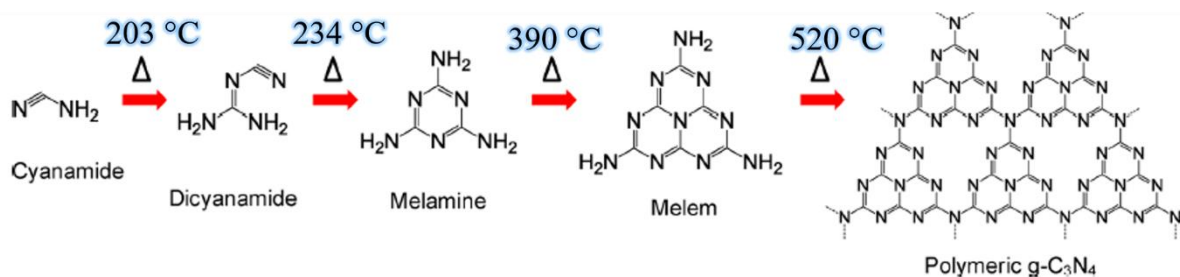


**Figure 1-14,** Reaction pathway of graphitic carbon nitride using cyanamide as the precursor [49]

Up to now  $g\text{-C}_3\text{N}_4$  has gained extensive attention in many fields like water splitting [50], photodegradation of environmental organic pollutants [51], organic synthesis [52], and  $\text{CO}_2$  reduction [53] due to having several advantages. Nevertheless, conventional bulk  $g\text{-C}_3\text{N}_4$  has been usually limited by unfavorable photocatalysis efficiency because of some drawbacks. As depicted in Figure 1-15, the advantages of  $g\text{-C}_3\text{N}_4$  are its strong reduction ability because of the position of conduction band, having the bandgap of 2.7 eV which make it active under visible light, extreme stability, non-toxicity, facile fabrication, and low-cost preparation. Nevertheless, conventional bulk  $g\text{-C}_3\text{N}_4$  has been usually limited by unfavorable photocatalysis efficiency because of the high recombination rate of photoinduced charges, small specific surface area, and insufficient solar light absorption [46].

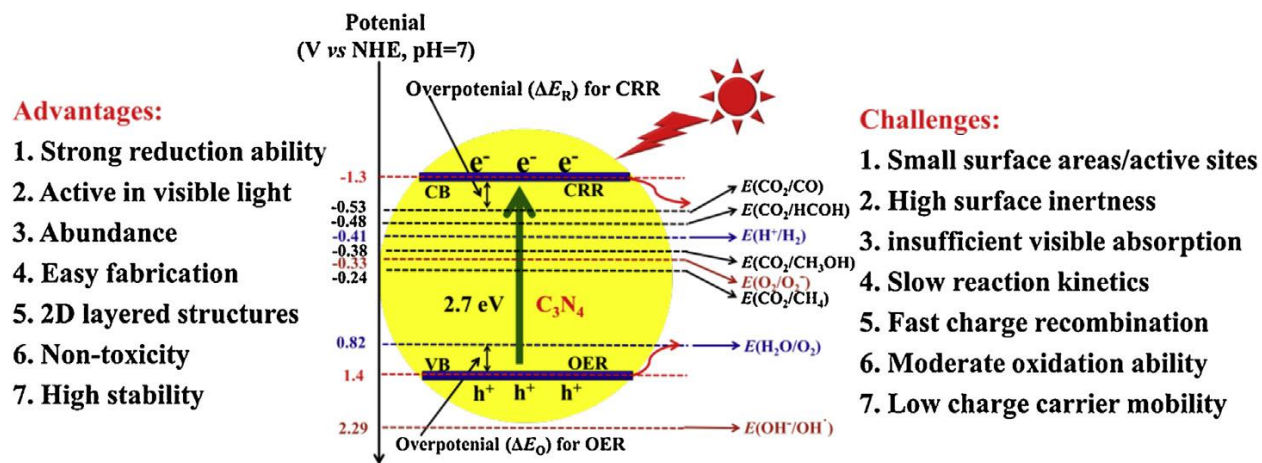


**Figure 1-15** The redox potentials of the relevant reactions with respect to the estimated position of the g-C<sub>3</sub>N<sub>4</sub> band edges at pH 7 [46]

Different modification approaches have been explored to deal with the above deficiencies and enhance the photocatalytic performance of g-C<sub>3</sub>N<sub>4</sub>. A brief explanation of some important modification strategies is explained in the following section.

### **1.4.3 Different modification strategies for g-C<sub>3</sub>N<sub>4</sub>**

For the abovementioned arguments, precise attention must be given to the fabrication of g-C<sub>3</sub>N<sub>4</sub> to attain the optimum and efficient photocatalytic activity. Figure 1-16 summarizes some important strategies that have been employed by researchers and scientists to enhance the properties of g-C<sub>3</sub>N<sub>4</sub>.

#### **1.4.3.1 Heteroatom doping**

Doping atoms into g-C<sub>3</sub>N<sub>4</sub> has been extensively investigated for different applications of pollutant degradation, H<sub>2</sub> evolution, and CO<sub>2</sub> reduction. Generally speaking, doping can be divided into two categories of metal doping and non-metal doping. The presence of metal ions in the g-C<sub>3</sub>N<sub>4</sub> structural unit, can serve as an electron sink for photogenerated electron and hole, extending the recombination time of e<sup>-</sup> and h<sup>+</sup>, hence enhancing the photocatalytic activity of g-C<sub>3</sub>N<sub>4</sub>. As an example, Tonda et al used ferric chloride as the source of Fe metal, and synthesized Fe-Doped graphitic carbon nitride (g-C<sub>3</sub>N<sub>4</sub>). The Fe dopant presented as being in the +3 oxidation state and could notably affect the electronic and optical properties of g-C<sub>3</sub>N<sub>4</sub> [54]. Based on their conclusion,

2 mol% Fe-doped  $g\text{-C}_3\text{N}_4$  represented almost 7 times and 4.5 times higher photoactivity in comparison with pure  $g\text{-C}_3\text{N}_4$ . Potassium-doped  $g\text{-C}_3\text{N}_4$  was synthesized through the thermal polymerization of dicyandiamide and KI. It was reported that the doped potassium can increase the photocatalytic activity by lowering the valence band and decreasing the photogenerated charge recombination [55]. Other metal doping such as Zr-doped and W-doped graphitic carbon nitride were also prepared to enhance the photocatalytic activity of  $g\text{-C}_3\text{N}_4$ .

In the case of non-metal doping, different dopant elements such as oxygen, sulfur, phosphorous, iodine, nitrogen, fluorine, and boron were utilized. As an example, Oxygen-doped  $g\text{-C}_3\text{N}_4$  was fabricated using hydrothermal treatment and hydrogen peroxide as the dopant precursor [56]. XPS studies showed that oxygen was doped into the lattice and then formed N–C–O, resulting to notable changes in the physicochemical characteristics. Subsequently, increased photodegradation and photocatalytic hydrogen evolution were achieved.

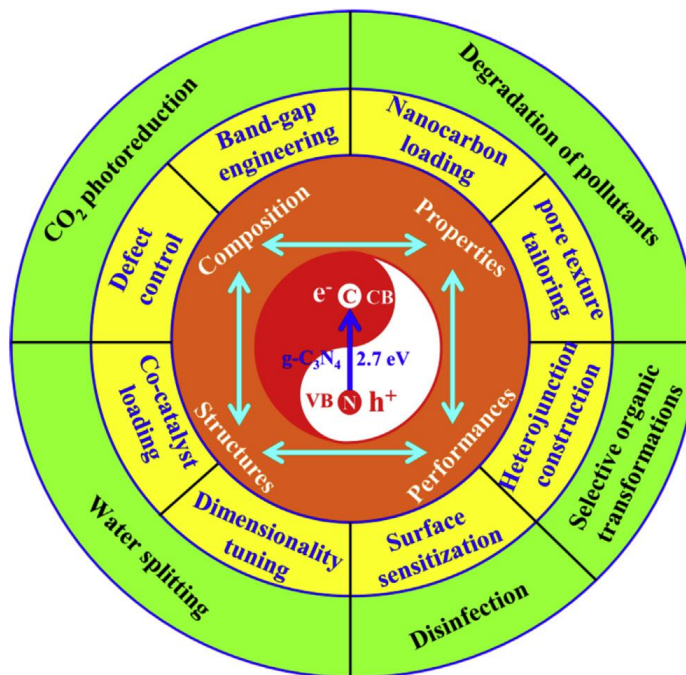


**Figure 1-16;** Various modification strategies for  $g\text{-C}_3\text{N}_4$ -based photocatalyst [46]



#### **1.4.3.2 Heterojunction with other material**

After the absorption of light and electron-hole photogeneration, the migration of charge carriers to the surface and further redox reactions compete with the  $e^-/h^+$  recombination in the bulk or surface of g-C<sub>3</sub>N<sub>4</sub> photocatalyst. To avoid the fast recombination of electron and holes, heterojunction strategy which is combination of g-C<sub>3</sub>N<sub>4</sub> with other semiconductor materials could be very helpful. The coupling of g-C<sub>3</sub>N<sub>4</sub> and another semiconductor unit with different bandgap and electronic properties leads to a new electronic structure after hybridization. In other ways, band bending is fabricated at the interface of the heterojunction nanocomposites because of the potential alteration among two sides. This causes a built-in electric field inside a space charge region to particularly depart and transfer the photogenerated electrons and holes [57].

#### **1.4.3.3 Nanostructure engineering**

Normally, in comparison to the bulk counterparts, nano-structured g-C<sub>3</sub>N<sub>4</sub> photocatalyst with manipulated dimensions and configurations could possess many obvious benefits for visible-light photoreactions. Nanostructured graphitic carbon nitride mostly has higher specific surface area, shorter photocharge migration length, and tunable electronic structure, compared to the bulk sample. The design of nanostructures includes the construction of nanosphere [58], nanotubes [59, 60], nanorods [48, 61], nanosheets [62], nanoclusters [8], and porous hierarchical structure [63]. Up to now, templating and template-free approaches were employed to create nanostructure g-C<sub>3</sub>N<sub>4</sub>.

#### **1.4.3.4 Defect engineering**

Vacancy engineering as an efficacious way to enhance the photocatalytic activity of semiconductors without introducing foreign elements. Forming defects into semiconductor is

usually along with bond breaking and reforming, lattice distortion and electron localization, which changes the band, electronic structure and material properties of photocatalysts [64]. Vacancies are common point defects in photocatalytic semiconductors. Photocatalyst with disordered structure can form vacancy defects. Different researchers used vacancy engineering strategy to improve the photoactivity of various semiconductors including  $\text{TiO}_2$  [65],  $\text{WO}_3$  [66],  $\text{SrTiO}_3$  [67] and  $\text{ZnS}$  [68]. Introducing vacancy and defects into the structure of photocatalyst supplies some essential advantages: (1) vacancies considerably influence the band structure of the photocatalyst. Overly, with the existence of vacancies, defect induction sites with weaker bonding reduce the splitting between bonding and antibonding orbitals, thus generate electronic states inside the bandgap [69]. The electronic states reduce bandgaps or act as midgap states for the photoexcitation of electrons and therefore broaden the light absorption range; (2) the electron states induced by defects provide an important way for the energetic relaxation of photogenerated charge carriers within the energy bandgap, thereby affecting the dynamics of charge carriers. Surface vacancy defects can be used as electron or hole capture centers, greatly inhibiting electron-hole recombination and facilitating the migration of photogenerated charges driven by a built-in field from body to surface [84–88]; (3) the formation of vacancy defects can further reduce the coordination number of the neighboring atoms, which makes them to be much more reactive sites. Generally, the existence of vacancy defects could strongly affect the electronic structure of the catalyst, thereby affecting the activity of the reaction site [89]. As a result, vacancy acts as an active site, enhancing the adsorption of reactants, facilitate the removal of electrons from the material to the adsorbent, and even directly participating in specific photocatalytic reactions

## 1.5 Hard-template method

Hard templating methods have been widely applied to a range of ‘soft’ and ‘hard’ materials, including g-C<sub>3</sub>N<sub>4</sub>. Hard templating, also known as ‘nanocasting’, involves filling or coating of a rigid template with a precursor material, treatment of the precursor to form the desired material and finally removal of the template to create a replica. Templated materials can take a range of forms including hollow materials from coating a template, or inverse materials from infilling of voids within a template (Figure 1-17). The essential difference between hard and soft templating methods is that soft methods rely on the cooperative assembly between the surfactant and inorganic phase, not replicating a certain surfactant structure. Compared with soft templating methods, the product of using hard template are relatively easy to control, since templates have fixed structures.

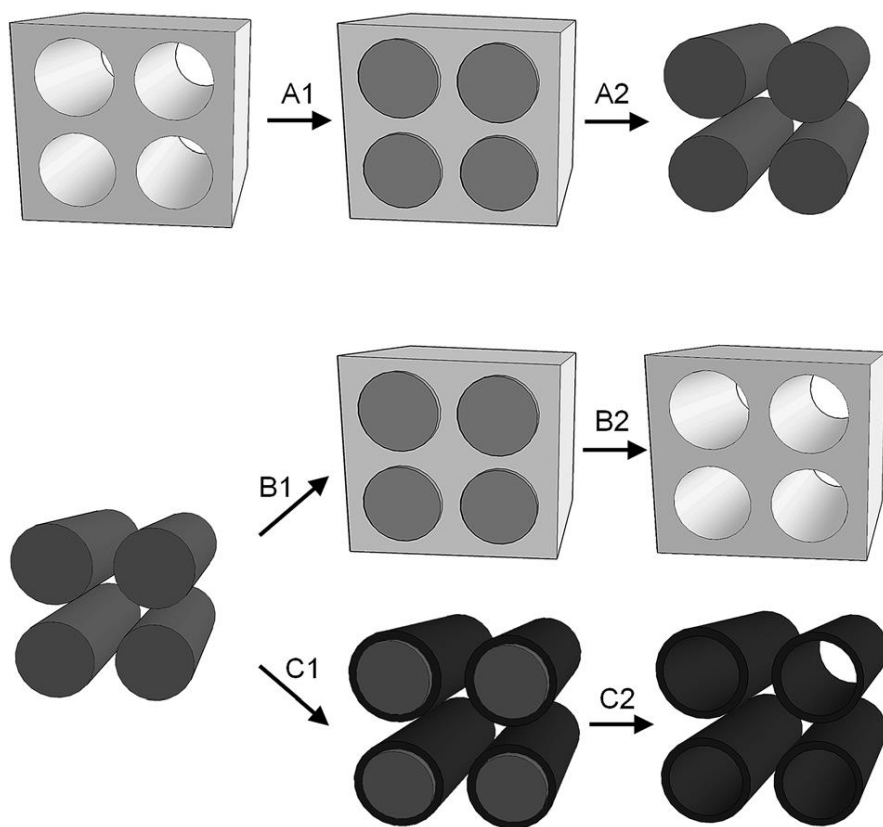


**Figure 1-17** A schematic of nanocasting steps including infilling of a hollow (A1) or particulate (B1) template or coating (C1) of a template followed by removal of the template to leave inverse (A2) or hollow (B2, C2) replicas.

## 1.6 Research objective and steps

This research aimed at developing a highly efficient graphitic carbon nitride photocatalyst for photodegradation of aqueous organic pollutants of RhB, MB, BPA, and TC. The framework and steps that was conducted in this project is represented in Figure 1-18 and explained below.

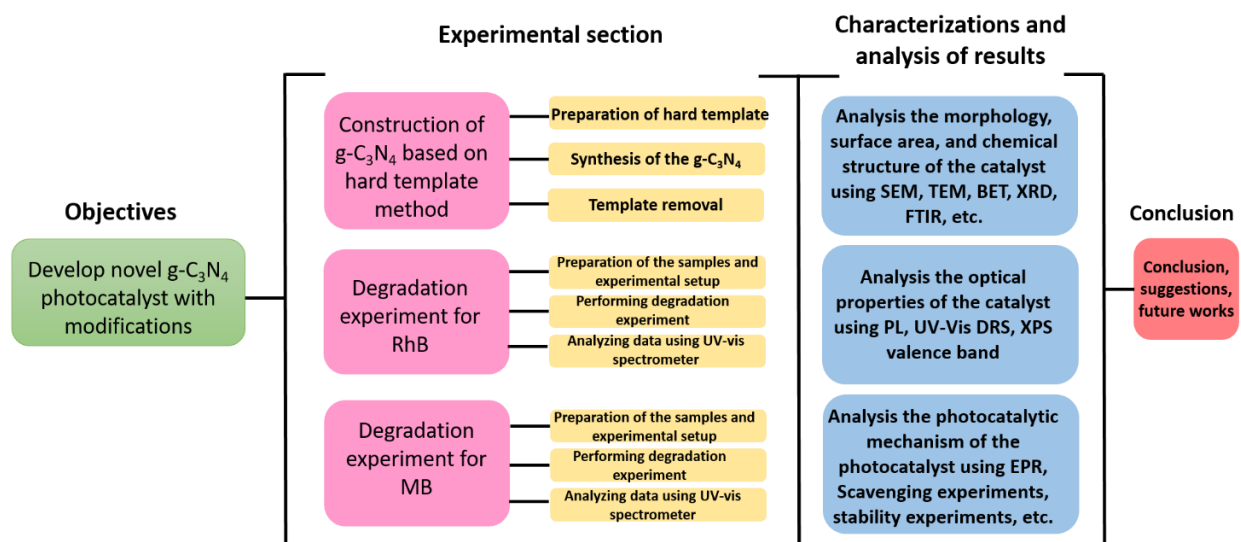


**Figure 1-18** Framework of this research

**The objective:** The objective of this research project was to construct a highly efficient g-C<sub>3</sub>N<sub>4</sub> photocatalyst that has the ability to degrade organic pollutants in a short time.

**Experimental section:** In this section, the synthesis process of the photocatalyst was conducted.

In order to fabricate an efficient g-C<sub>3</sub>N<sub>4</sub> photocatalyst, we conducted hard template method. In this method, as is presented in the Figure 1-19, the first step is the preparation of the template. The second step is mixing the template with the precursor, the fourth step is synthesis of the catalyst, and the final step is removal of the template.

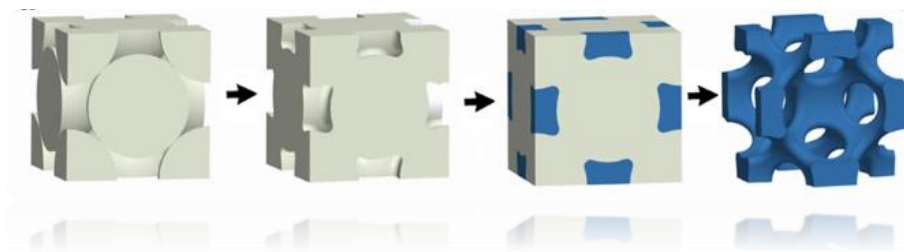


**Figure 1-19** A schematic representation of hard-templating method

Then, prepared organic pollutants in various concentrations to analyze the performance of the synthesized photocatalysts toward degradation of them.

**Characterization and analysis of the results:** In this step, we performed various characterizations to analyze the properties of the synthesized samples. We conducted SEM, TEM, and BET to analyze the morphology and porosity of the samples. XRD, FTIR, XPS, NMR, elemental analysis should be used to investigate the crystallinity and chemical structure of the samples. To scrutinize the optical properties, we conducted PL, UV-Vis DRS. And then we will check the the degradation mechanism using scavenging experiments, EPR and etc.

# **Chapter 2- Construction of mesoporous g-C<sub>3</sub>N<sub>4</sub> nanoclusters**

In this section, by using SiO<sub>2</sub> clusters as a template, mesoporous graphitic carbon nitride nanoclusters (NC MCN) were fabricated as a high-activity photocatalyst. The confined growth of carbon nitride in the presence of SiO<sub>2</sub> clusters introduced extra structural defects to the carbon nitride framework including nitrogen vacancies and cyano groups, which was confirmed by employing different characterization analyses. These structural defects created midgap states below the conduction band, which improved light-harvesting efficiency and suppressed electron-hole recombination. Thus, NC MCN showed high photocatalytic activity toward degradation of

both tetracycline and rhodamine B under visible light irradiation. Complete degradation of 15 ml solution of 15 ppm tetracycline was achieved in 30 min compared to the bulk catalyst (taking more than 3 h). Furthermore, NC MCN demonstrated high stability after reusing for 8 consecutive photodegradation cycles. The total organic carbon concentration at different reaction time showed a rising and falling trend, which illustrate photodegradation process, i.e. adsorption, photodegradation, and mineralization. By liquid chromatography-mass spectroscopy analysis, the produced intermediates during the tetracycline degradation were proposed, which showed the formation of smaller molecules in just 15 min. The toxicity of the intermediates was analyzed using quantitative structure-activity relationship estimation and the outcomes exhibited that the toxicity of the solution reduced as the reaction time increased. This comprehensive study from photodegradation process to mineralization of TC demonstrated NC MCN as a promising photocatalyst for sustainable treatment of wastewater

## 2.1 Introduction

One important strategy to boost the visible light photocatalytic effectiveness of  $g\text{-C}_3\text{N}_4$  is the introduction of porosity into the structure of the material. Introducing porosity is along with enlarging the surface area, reachable channels, and active sites leading to enhancing the photogenerated charge separation, molecular mass transfer, and surface reaction [70]. Therefore, different researches have focused on synthesizing porous  $g\text{-C}_3\text{N}_4$ . Zhang et al. reported an approach of thermal polymerization by using a supramolecular precursor to achieve 2D porous structure graphitic carbon nitride with enlarged surface area and improved efficiency toward hydrogen evolution [71]. Liu et al. synthesized porous nanoplate graphitic carbon nitride in few

layers, utilizing thermal etching along with gas-driven exfoliation of bulk g-C<sub>3</sub>N<sub>4</sub> which enhanced the activity of photocatalyst in RhB degradation [72]. Additionally, recent studies proposed that implanting nitrogen defects into the lattice structure of g-C<sub>3</sub>N<sub>4</sub> could remarkably intensify photocatalytic activity in different applications of bisphenol A degradation [73], hydrogen evolution [74] as well as CO<sub>2</sub> reduction [75]. That is mainly because defect sites tend to trap photogenerated electrons and promote charge carrier separation. Therefore, to prepare N-deficient g-C<sub>3</sub>N<sub>4</sub> with a higher H<sub>2</sub> evolution rate compared to the bulk catalyst, the molten salt post-treatment method was conducted by Liu et al [76]. Furthermore, Xue et al. prepared a g-C<sub>3</sub>N<sub>4</sub> with abundant nitrogen vacancies and cyano groups by alkali-assisted heat treatment of urea which showed excellent photocatalytic N<sub>2</sub> fixation activity in comparison to the bulk sample [77].

These studies inspired us to direct our research on fabricating nanostructure porous graphitic carbon nitride with nitrogen vacancies to simultaneously enhance active sites, light absorption efficiency, and charge separation capability of the catalyst. For the sake of achieving this objective, template-based methods are appropriate candidates that allow us to control the structure and morphology of catalysts. Chen et al. successfully constructed Cyano-rich mesoporous carbon nitride nanospheres by using mesoporous SiO<sub>2</sub> nanospheres as sacrificial templates and cyanamide as a precursor [73]. Liang et al. synthesized nitrogen defects modified mesoporous g-C<sub>3</sub>N<sub>4</sub> by employing the silica gel template method and mixing with cyanamide [74]. Although these studies could successfully construct the mesoporous structure by introducing vacancies, the main drawback associated with their synthesis lies in the fact that the cyanamide precursor is highly toxic, flammable, and expensive, thus limiting its usage in large-scale manufacturing [78]. On contrary, melamine that has been exploited as a nitrogen-rich precursor to synthesize g-C<sub>3</sub>N<sub>4</sub> in recent years is non-toxic, stable, and readily available at low cost [79]. Moreover, to the best of



our knowledge, comprehensive investigation of mesoporous g-C<sub>3</sub>N<sub>4</sub> with vacancies in the application of organic pollutants degradation especially tetracycline is rarely conducted, despite its high necessity. So, more research in this field is crucial to further promote the photocatalytic activity of mesoporous g-C<sub>3</sub>N<sub>4</sub> and investigate the possible applications of this promising catalyst.

Inspired by the above-mentioned considerations, in this study we used a new method to construct mesoporous graphitic carbon nitride nanoclusters with nitrogen vacancies and bonded with cyano groups by using silica nanoclusters as the sacrificial template and melamine as the precursor. By adopting the silica nanoclusters template, the growth of g-C<sub>3</sub>N<sub>4</sub> planes was confined during thermal polymerization and favorable defects were introduced into the structure. The existence of structural defects and their role in enhanced photocatalytic activity were confirmed by different characterization analyses. Various experimental characterizations were implemented to precisely analyze morphological, structural, and optical characteristics of synthesized catalysts. The photoactivity of as-prepared photocatalysts was evaluated for tetracycline (TC) and rhodamine B (RhB) degradation under visible light irradiation. The mesoporous g-C<sub>3</sub>N<sub>4</sub> nanoclusters showed superior activity toward degradation of both pollutants in comparison to Bulk g-C<sub>3</sub>N<sub>4</sub> because of having a porous structure, higher surface area which provided more active sites, and the existence of defects that highly suppressed the recombination of photogenerated charge carriers. Furthermore, as complete mineralization of organic pollutants during the photocatalytic reaction is difficult, as a result of partial oxidization, some intermediates will be produced. In some cases, the produced intermediates possess higher toxicity and risk to the human and environment. Thus, investigating the total organic carbon (TOC) and identifying produced intermediates and the toxicity associated with them is of great importance. Herein, the TOC concentration and mineralization capability of as-prepared catalysts were investigated, and possible intermediates of

TC that were produced in different photocatalytic reaction times were predicted using LC-MS analysis. Moreover, the toxicity of these produced intermediates was investigated by quantitative structure-activity relationship (QSAR) prediction.

## **2.2 Experimental section**

### **2.2.1 Chemicals**

Melamine, rhodamine B, triethanolamine, silver nitrate, isopropyl alcohol, 5,5-dimethyl-1-pyrroline N-oxide, were obtained from Chemicals & Metals Company of Daejung, Ltd. (Gyeonggi-Do, Korea). Colloidal silica dispersions (12 nm, Ludox HS-40, 40% wt.% suspension in water), tetracycline, p-Benzo-quinone were purchased from Sigma-Aldrich. All used chemicals and reagents were of analytical grade and utilized as delivered without any more purification. In all experiments, distilled water was used.

### **2.2.2 Preparation of g-C<sub>3</sub>N<sub>4</sub> samples**

To prepare mesoporous g-C<sub>3</sub>N<sub>4</sub>, colloidal silica dispersion (12 nm, Ludox HS-40, 40% wt.% suspension in water) was dried in an oven at 100 °C for 12 h and then grounded in mortar. The obtained SiO<sub>2</sub> cluster template (1.5 g) was mixed with melamine (1.5 g) thoroughly and transferred to a crucible. After that, the mixture was heated in the air from room temperature to 550 °C in 4 h and kept at this temperature for 3 h. The resultant yellow g-C<sub>3</sub>N<sub>4</sub>/SiO<sub>2</sub> hybrids were added to 40 mL of 10% HF solution for 24 h to remove the silica template. The suspension then went through centrifugation, washed with distilled water several times until the pH reached 7, and then finally

dried at 70 °C in the oven. The resulting catalyst was denoted as NC MCN. As a reference sample, bulk g-C<sub>3</sub>N<sub>4</sub> was synthesized by calcination of 1.5 g melamine with the same heat treatment as the previous one (Bulk CN). A schematic representation of synthesis process is shown in Figure 2-1.

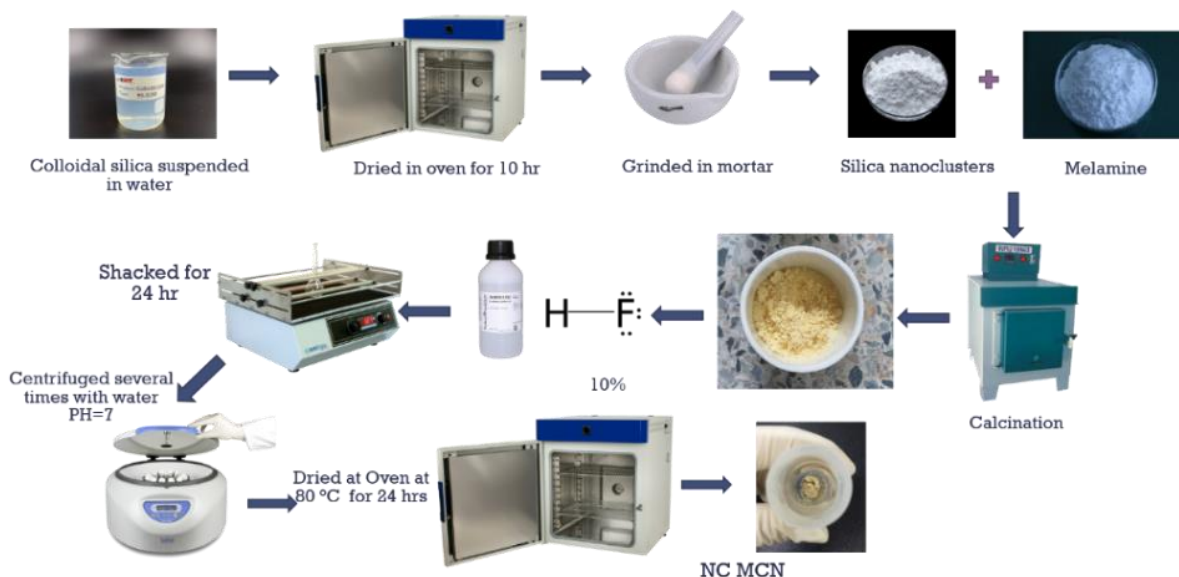


**Figure 2-1** Synthesis procedure of NC MCN

### 2.2.3 Characterization

The verification of the morphology of the samples was conducted using field emission scanning electron microscopy (FE-SEM) and transmission electron microscopy (TEM). The powder X-ray diffraction (XRD) patterns of the as-prepared samples were obtained with a Bruker/D8 (Advance model) diffractometer in the  $2\theta$  range of 10.0 to 80° using steps of 0.1-degree operating with Cu K $\alpha$  radiation as the X-ray source. Fourier transform infrared (FTIR) spectra were obtained utilizing Varian 670/620 spectrometer to investigate structural characterization. Solid-state <sup>13</sup>C magic angle spinning (MAS) nuclear magnetic resonance (NMR) spectra of catalysts were recorded on a

Bruker NVMRS 600 MHz solid-state NMR spectrometer at room temperature. The surface chemical compositions were determined with X-ray photoelectron spectroscopy (XPS) utilizing a Thermo Fisher Scientific spectrometer equipped with a monochromated Al-K $\alpha$  X-ray source. UV-vis diffuse reflection spectroscopy (UV-vis DRS) was performed using a Carry 5000 UV-vis DRS-Agilent-Model spectrophotometer in a spectral range of 200–800 nm. The photoluminescence (PL) spectra were recorded using Cary Eclipse (Model NF900 (FLS920)) photoluminescence detector with a 340 nm excitation wavelength. The Brunauer-Emmett-Teller (BET) surface areas and the distribution of pores of the samples were analyzed by N<sub>2</sub> porosimetry using Micromeritics Instruments (Model ASAP2020 Analysis). The electrochemical impedance spectroscopy (EIS) was investigated in the frequency range of 0.05 Hz to 100 kHz at 0.6 V (vs. Ag/AgCl) in Na<sub>2</sub>SO<sub>4</sub> solution under light illumination. To obtain the concentration of the organic pollutants at different time intervals, UV-vis spectroscopy equipment (Thermo Fisher Scientific, model: G10S UV-Vis) was employed. Electron paramagnetic resonance (EPR) was conducted using a Bruker model EMX-12 spectrometer with  $f=9.64$  GHz. To estimate the intermediates and the probable transform pathways of TC degradation, liquid chromatography-mass spectroscopy (LC-MS) was used.

#### **2.2.4 Evaluation of the photocatalytic performance**

To obtain the photocatalytic performance of the as-synthesized g-C<sub>3</sub>N<sub>4</sub> samples for degradation of TC and RhB, the experiments were conducted under visible light irradiation, and for the light source, a 300 W xenon lamp (with installed UV cut-off filter and an IR water filter ( $400 < \lambda < 800$  nm)) was used. Typically, before the photocatalytic test, 15 mg of the catalyst was mixed with 15 mL aqueous solution of the organic pollutant (TC or RhB) with a concentration of 15 mgL<sup>-1</sup>. Before irradiation, the mixture was stirred for 15 min in the dark situation to allow the solution

and the catalyst to attain adsorption-desorption equilibrium. Afterward, the light turned on and the mixture was irradiated while stirring. During the photocatalytic reaction, the solution was withdrawn every 15 min and centrifuged at the speed of 4000 rpm for 10 min, and the remaining concentration of the pollutant was measured and determined using a UV-Vis spectrometer. The following equation shows the photocatalytic degradation efficiency (PDE) of TC and RhB.

$$\text{PDE} = (C_0 - C_n) / C_0 \times 100\% \quad (1)$$

Where  $C_0$  ( $\text{mgL}^{-1}$ ) is the starting concentration of RhB and TC, and  $C_n$  is the concentration of pollutant after the irradiation time of  $t$ .

## **2.3 Results and discussion**

### **2.3.1 Synthesis mechanism**

Ludox colloidal silica suspensions contain nano-size (around 12 nm), discrete, spherical silica particles dispersed in water. While dispersing, the particles are electrostatically stabilized and there is no reaction with each other without any producing agglomeration [80, 81]. When this suspension is dewatered without stirring, the nano-sized silica particles become unstable and connect until making bigger clusters with randomized shapes [82]. The surface of these clusters is non-flat composed of small (12 nm)  $\text{SiO}_2$  nanoparticles. By mixing melamine with  $\text{SiO}_2$  clusters followed by calcination, polymerization occurs in the narrow spaces between silica clusters. In also, confining and limiting the growth of g- $\text{C}_3\text{N}_4$  planes result in incomplete polymerization and construction of defects in the structure of the sample.

## 2.3.2 Morphologies and porous structure

### 2.3.2.1 Scanning Electron Microscopy (SEM) and Transmission Electron Microscopy (TEM) characterizations

To explore the morphology and microscopic structure of silica clusters and synthesized materials, SEM and TEM were implemented. The SEM image of SiO<sub>2</sub> clusters after drying is displayed in Figure 2-2a which illustrates the formation of silica clusters (through sticking and aggregation of small silica nanoparticles). After mixing the SiO<sub>2</sub> clusters with melamine, during the calcination process, the growth of g-C<sub>3</sub>N<sub>4</sub> planes was confined and controlled based on the shape of silica clusters. Figure 2-2b represents the obtained morphology of the NC MCN. On the contrary, it could be seen from Fig. 2-2c that the g-C<sub>3</sub>N<sub>4</sub> synthesized without using silica clusters, displays very stacked-layered morphology. By using TEM images, the internal structure and morphology of the NC MCN could be furthermore investigated, which confirms the construction of small clusters and mesoporous architecture (Figures 2-2 d, e, and f). Figure 2-2 g and h show the HRTEM fringes of NC MCN with 0.33 nm inter-planer spacing [83].

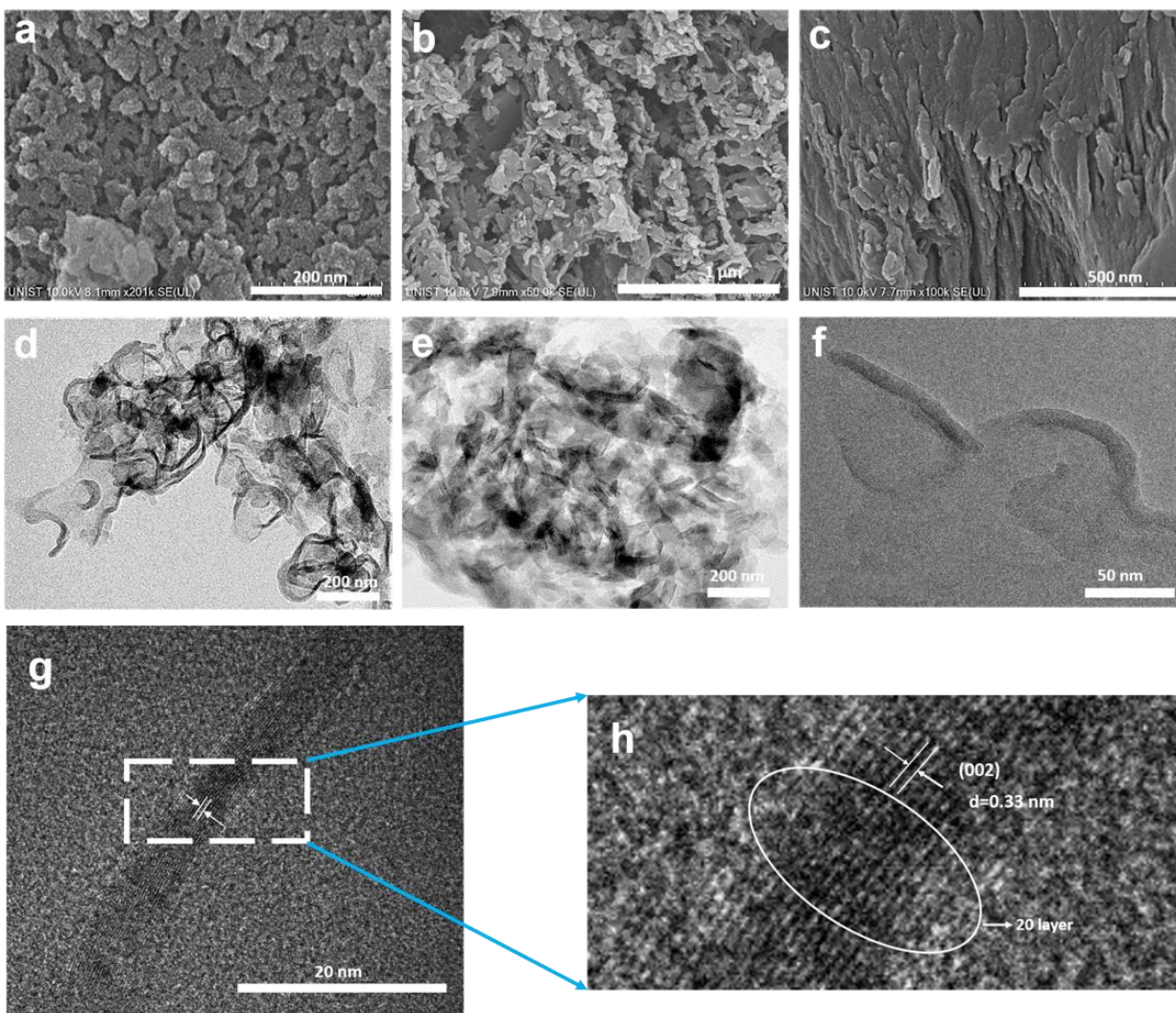


**Figure 2-2.** SEM images of (a) SiO<sub>2</sub> clusters, (b) NC MCN, (c) Bulk CN; TEM images of (d, e, f, g, h) NC MCN

### 2.3.2.2 Brunauer-Emmett-Teller (BET) analysis

To further investigate the surface properties and porosity of the catalysts, the nitrogen adsorption-desorption measurements were conducted (Figure 2-3). The obtained plot of both catalysts revealed a typical IV-type isotherm with an H3 hysteresis loop in the range of 0.4-0.95 P/P<sub>0</sub> based on the International Union of Pure and Applied Chemistry (IUPAC) classification [84], confirming the presence of mesoporous structure. The BJH pore size distribution also clearly exhibits that NC

MCN possesses very abundant mesopores in the range from 2 to 20 nm compared with the Bulk CN. Besides, the pores larger than 20 nm until 80 nm exist in the sample, which is due to the reverse replica of silica clusters with various sizes. The BET specific surface area, pore diameter, and pore volume of the samples are summarized in Table 2-1. Consistently, NC MCN exhibited a specific surface area of  $51.34 \text{ m}^2 \text{ g}^{-1}$  and pore volume of  $0.226 \text{ cm}^3 \text{ g}^{-1}$ , which are much higher than those of Bulk CN ( $21.49 \text{ m}^2 \text{ g}^{-1}$ ,  $0.126 \text{ cm}^3 \text{ g}^{-1}$ ). These data illustrate that using clusters of silica as hard templates could significantly produce a mesoporous structure with enhanced surface area and enlarged pore volume.

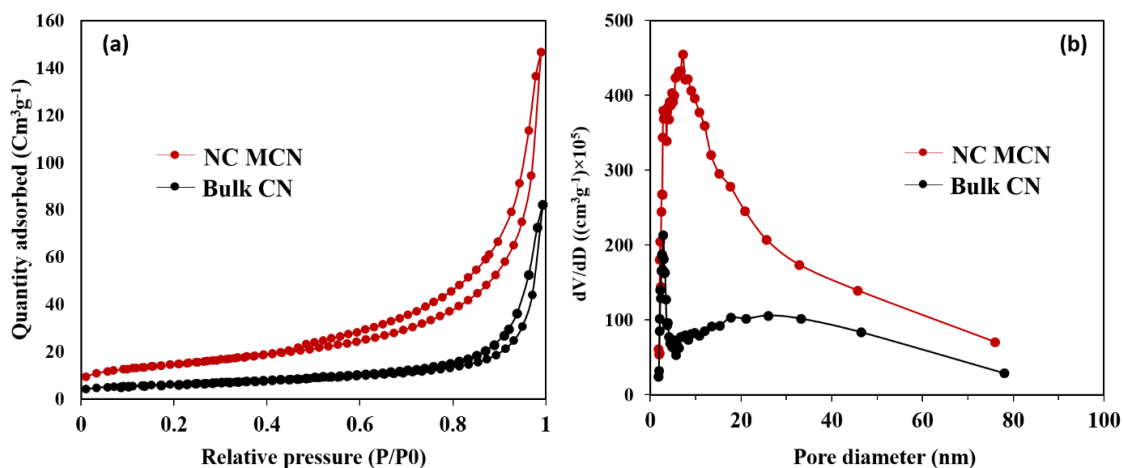


**Figure 2-3.** (a)  $\text{N}_2$  adsorption/desorption isotherms (b) The corresponding pore size distribution curves of NC MCN and Bulk CN

**Table 2-1.** BET surface area, average BJH pore size, and pore volume of NC MCN and Bulk CN

Sample	Pore volume ( $\text{cm}^3 \text{ g}^{-1}$ )	Pore diameter (nm)	BET surface area ( $\text{m}^2 \text{ g}^{-1}$ )
NC MCN	0.226	17.66	51.34
Bulk CN	0.126	23.63	21.49



### 2.3.3 Crystal structure and chemical composition

#### 2.3.3.1 X-ray Diffraction (XRD) spectroscopy

The chemical composition and crystal structure of the synthesized catalysts were studied by employing X-ray diffraction (XRD) analysis. As exhibited in Figure 2-4, the representative XRD pattern of the bulk CN shows two diffraction peaks located at around  $27.4^\circ$  and  $13.1^\circ$ , which can be indexed as the (002) and (100) reflections. These peaks can be ascribed to the interplanar stacking of carbon nitride layers and in-plane structural packing motifs, respectively [85, 86]. Also, the XRD pattern of the NC MCN has depicted the almost same diffraction patterns as those of the bulk sample, confirming that the typical crystal structure of  $g\text{-C}_3\text{N}_4$  is well preserved. Meanwhile, the peak intensity of both (002) and (100) planes in the NC MCN XRD pattern demonstrate an obvious reduction, indicating that the growth of basic layers of  $g\text{-C}_3\text{N}_4$  was confined because of using silica clusters as hard template [87]. Also, this peak has shifted to a larger angle, slightly from  $27.4^\circ$  to  $27.6^\circ$ , indicating a smaller stacking distance between layers due to the favorable defects [88, 89].

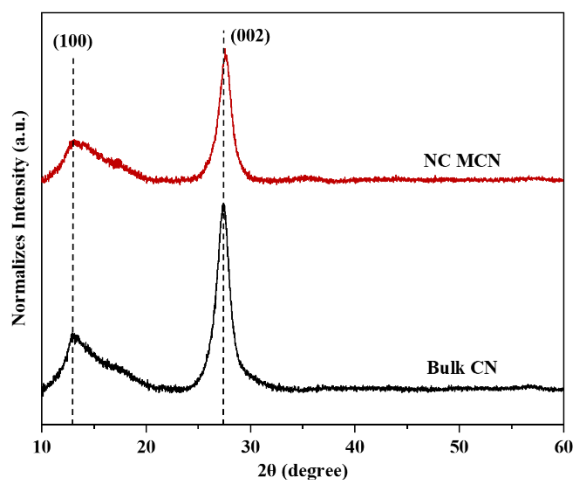


**Figure 0-4.** X-ray diffraction (XRD) patterns

### 2.3.3.2 Fourier Transform Infrared (FTIR) spectroscopy

Figure 2-5 represents the FT-IR spectra of the as-obtained g-C<sub>3</sub>N<sub>4</sub> samples which further confirm the construction of g-C<sub>3</sub>N<sub>4</sub> after removing the template. The peak located at 809 cm<sup>-1</sup> is attributed to the s-triazazine ring [90]. The group peaks in the region of 1000-1700 cm<sup>-1</sup> correspond to the stretching vibration modes of C-N heterocycles [91]. The presence of these peaks suggests the well-retention of the g-C<sub>3</sub>N<sub>4</sub> backbone in both samples. The broad peaks around 3000-3500 cm<sup>-1</sup> are ascribed to terminal amino groups and surface adsorbed water molecules [92]. The more pronounced peaks in this area may be related to the presence of more -NH<sub>2</sub> groups and H<sub>2</sub>O molecules that both of them show the higher active surface sites for the NC MCN sample compared to the bulk CN. Interestingly, the FT-IR spectra of NC MCN show a clear peak at around 2177 cm<sup>-1</sup>, which can be due to the asymmetric stretching vibration of terminal cyano groups (C≡N) [73, 89].

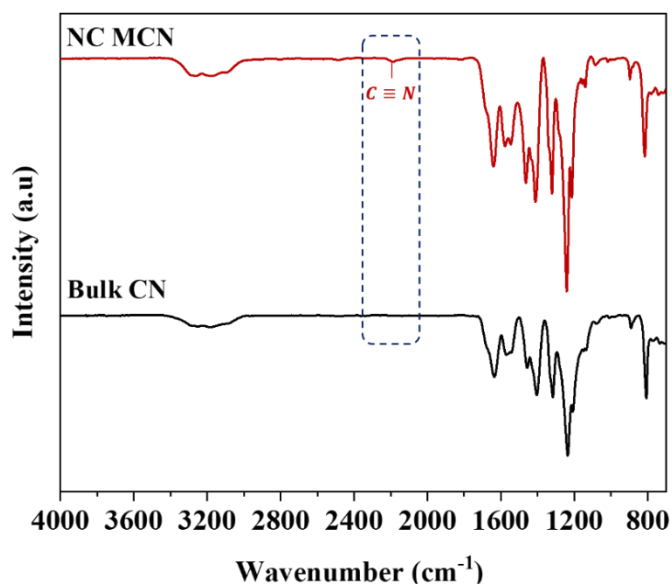


**Figure 0-5.** FTIR spectra of prepared catalysts

### 2.3.3.3 Solid-state $^{13}\text{C}$ Magic Angle Spinning (MAS) NMR measurements

Solid-state  $^{13}\text{C}$  magic angle spinning (MAS) NMR measurements were carried out to attain more deep insight into newly formed ( $\text{C}\equiv\text{N}$ ) groups. As shown in the Figure 2-6, the NMR spectra of both NC MCN and Bulk CN demonstrate distinct peaks at 156.5 ppm and 164.7 ppm attributed to carbon atoms of  $\text{C}_{3\text{N}}$  (C3) and  $\text{C}_{2\text{N-NHX}}$  (C2) in the heptazine units, respectively[93]. As for NC MCN, two clear peaks at 128.8 and 170.8 ppm were detected, which are corresponded to  $\text{C}\equiv\text{N}$  groups (C4) and the neighbor carbon atoms close to cyano groups (C1)[94, 95]. Consistent with FT-IR results, NMR analysis further confirms the formation of cyano groups in the NC MCN, while preserving the primary tri-s-triazine-based graphitic carbon nitride frameworks.

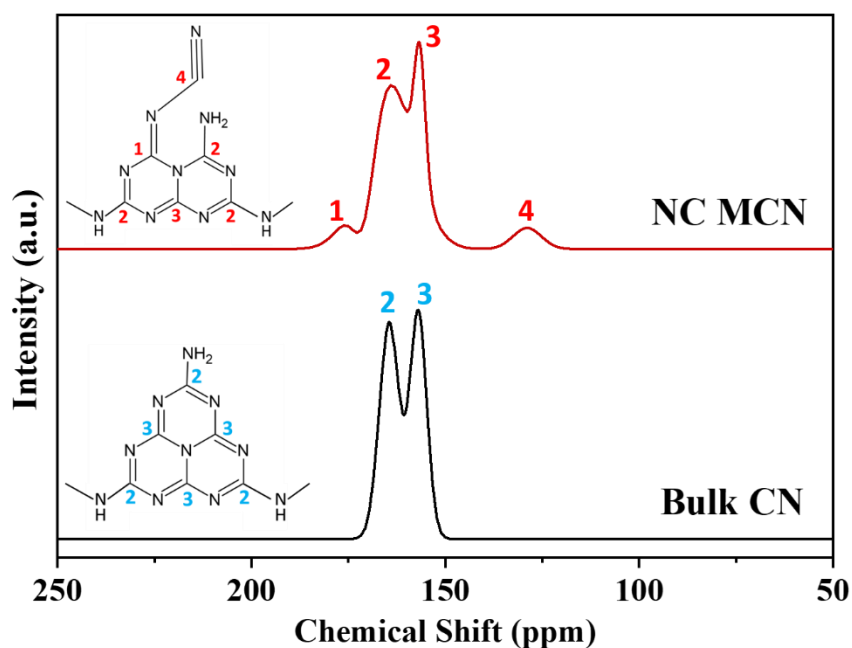
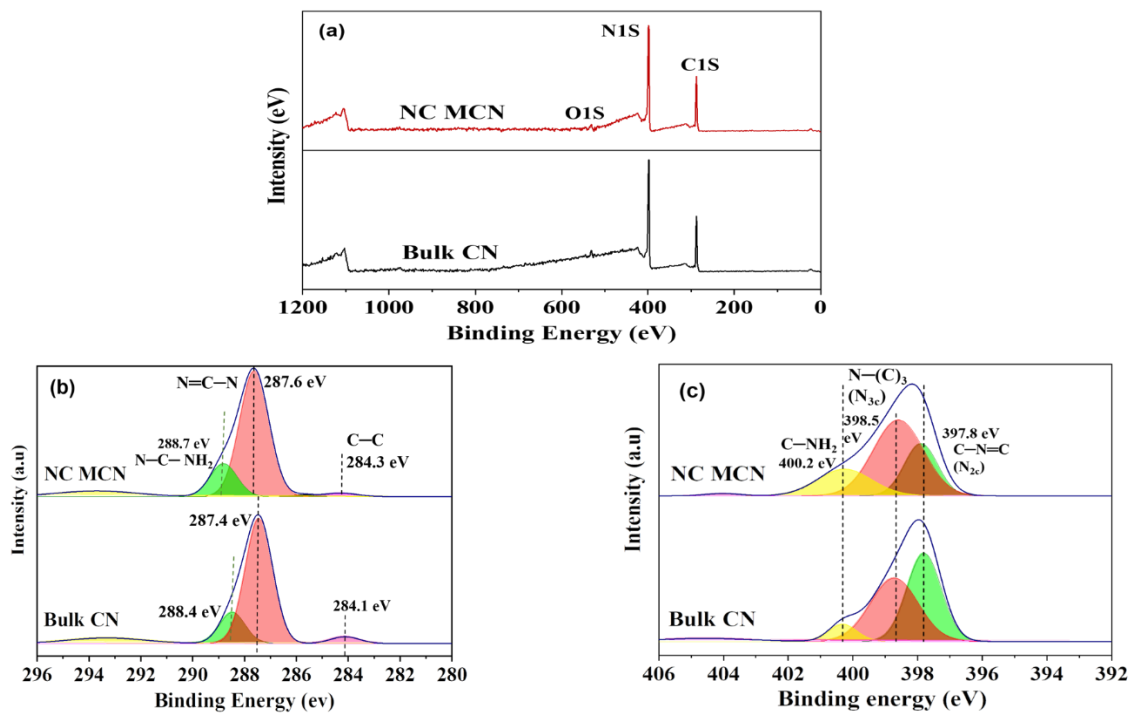


Figure 0-6. NMR spectra of as-obtained catalysts

#### 2.3.3.4 X-ray Photoelectron Spectroscopy (XPS)

X-ray photoelectron spectroscopy (XPS) was employed to gain more insights into the binding state and surface chemical compositions of the catalysts. As shown in Figure 2-7 a, the survey spectra of both NC MCN and Bulk CN show three peaks corresponding to C1s, N1s, and O1s signals which confirm the existence of C, N, and O in the structure, respectively. Figure 2-7 b shows the high-resolution C1s. The XPS data of both samples could be fitted to three peaks, however, their specific peak position and intensity were different. The C–C peak is assigned to the adventitious carbon (the graphitic form carbon C-C/C=C), the N=C–N peak corresponded to the sp<sup>2</sup> hybridized carbon in the triazine ring, and N–C–NH<sub>2</sub> is related to the edges of tri-s-triazine [96]. As depicted in Figure 2-7 c, the N1s core electron spectrum is deconvoluted into three peaks located at 397.8, 398.5, 400.2, which are associated with nitrogen species of sp<sup>2</sup> carbon in triazine units (–C=N–, N<sub>2c</sub>), tertiary amine groups (–N–(C)<sub>3</sub>, N<sub>3c</sub>), and terminal amino groups (C–NH<sub>2</sub>), respectively [97].

Based on the deconvolution results of N1s, the peak area of different N species was calculated and showed in Table 2-2. It can be observed that the peak area ratio N<sub>2c</sub> to N<sub>3c</sub> has decreased from 0.99 in Bulk CN to 0.45 in NC MCN. The reduction of N<sub>2c</sub>/N<sub>3c</sub> demonstrates the loss of N atoms in the triazine unit structure that can be a sign of nitrogen vacancies in the as-prepared NC MCN.



**Figure 2-7** XPS spectra of Bulk CN and NC MCN samples, (a) survey; (b) C1s; (c) N1s. (d) EPR spectra of NC MCN and Bulk CN

**Table 2-2.** XPS N1s deconvolution result of Bulk CN and NC MCN

	Bulk CN			NC MCN		
	N <sub>2C</sub> C-N=C	N <sub>3C</sub> N-(C) <sub>3</sub>	N <sub>CH</sub> C-NH <sub>2</sub>	N <sub>2C</sub> C-N=C	N <sub>3C</sub> N-(C) <sub>3</sub>	N <sub>CH</sub> C-NH <sub>2</sub>
<b>Peak/eV</b>	<b>397.79</b>	<b>398.7</b>	<b>400.3</b>	<b>397.8</b>	<b>398.5</b>	<b>400.2</b>
<b>FWHM</b>	<b>1.05</b>	<b>1.47</b>	<b>0.87</b>	<b>1.02</b>	<b>1.55</b>	<b>1.69</b>
<b>Area</b>	<b>4423.37</b>	<b>4441</b>	<b>705.53</b>	<b>2520</b>	<b>5578</b>	<b>2143</b>
<b>Peak area ratio (N<sub>2C</sub>/N<sub>3C</sub>)</b>		<b>0.99</b>			<b>0.45</b>	
<b>Peak area ratio (N<sub>CH</sub>/N<sub>3C</sub>)</b>		<b>0.15</b>			<b>0.38</b>	

### 2.3.3.5 Elemental Analysis (EA)

To further verify the presence of nitrogen-vacancy in the triazine unit structure of NC MCN, elemental analysis (EA) was employed. As shown in Table 2-3, the  $N_{\text{total}}/C_{\text{total}}$  atomic ratios show the nitrogen deficiency of NC MCN in comparison to the Bulk CN.

**Table 2-3.** Elemental analysis for Bulk CN and NC MCN

<b>Sample</b>	<b>C (wt.%)</b>	<b>N (wt.%)</b>	<b><math>N_{\text{total}}/C_{\text{total}}</math> (wt.%)</b>
<b>Bulk CN</b>	<b>34.70</b>	<b>60.06</b>	<b>1.73</b>
<b>NC MCN</b>	<b>31.50</b>	<b>54.36</b>	<b>1.72</b>

### 2.3.3.6 Electron Paramagnetic Resonance (EPR)

Additional evaluation of the presence of surface vacancies in the NC MCN was conducted using EPR measurements (Figure 2-8). Both the NC MCN and Bulk CN show an EPR signal with a computed  $g$  value of 2.003, which is derived from unpaired electrons on the  $sp^2$ -carbon atoms of aromatic rings [98]. Noticeably, enhanced EPR signal intensities of NC MCN compared to Bulk CN were observed which could be attributed to the existence of nitrogen vacancies in the structure of NC MCN [99]. The introduction of nitrogen vacancies could provide extra unpaired electrons for neighboring  $sp^2$ -carbon atoms in the  $\pi$ -conjugated triazine rings of NC MCN [96]. Therefore, all experimental results of XPS, elemental analysis, and EPR confirm the generation of nitrogen vacancies in the NC MCN. For more clarification, the schematic atomic model of Bulk CN and NC MCN is presented in Fig 2-9 which shows the position of different nitrogen species, nitrogen-vacancy, and cyano groups.

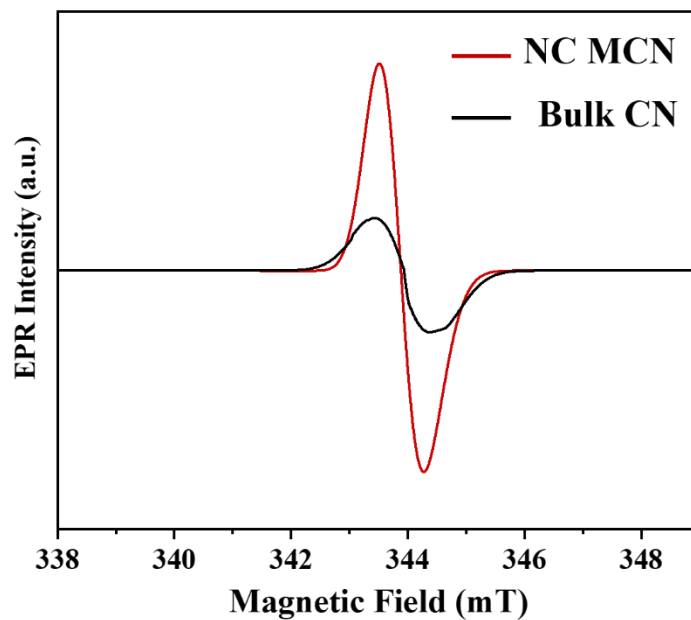


Figure 2-8 EPR spectra of NC MCN and Bulk CN

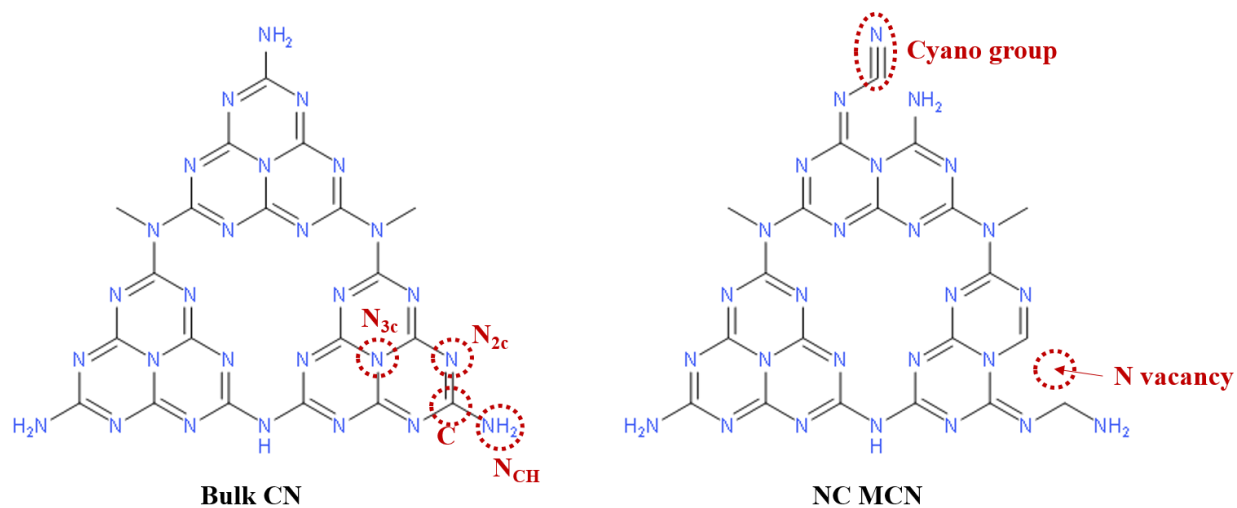
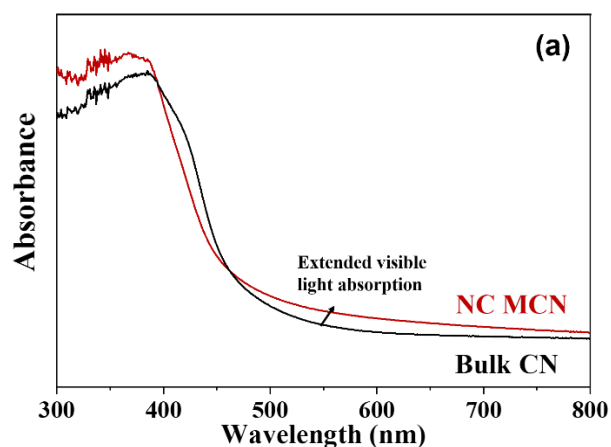


Figure 2-9 Schematic atomic model of Bulk CN and NC MCN

## 2.3.4 Optical properties and electronic band structure

### 2.3.4.1 UV-vis diffuse reflectance spectroscopy (DRS)

To gain more insights into the changes in the light-harvesting capacity and bandgap energy of the catalysts obtained after the introduction of nitrogen vacancies, UV-Vis DRS and XPS valence band determination were conducted. As shown in Figure 2-10, the absorption edge for Bulk CN and NC MCN are located at 500 and 480 nm, respectively, indicating they are visible light-responsive. The higher absorption intensity of NC MCN in the visible light region can be ascribed to the generation of mid-gap states because of the presence of nitrogen vacancies. Also, it can be due to the multiple scattering effects in the porous structure of the catalyst [77]. As compared to the Bulk CN, an obvious tail (Urbach tail) was observed in the visible light region of NC MCN, which is correlated to the electronic states within the bandgap, known as midgap states, due to the imperfection of the structure. These midgap states result in the construction of sub-bandgaps lower than the main bandgap. Furthermore, the obvious blue shift in the absorption edge of NC MCN compared with the Bulk CN shows the enlargement of bandgap due to the quantum confinement effect as a result of the nanostructure formation [96].



**Figure 2-10** UV-Vis diffuse reflectance spectra of synthesized samples



#### 2.3.4.2 XPS valence band and bandgap structure

To calculate the bandgap energies ( $E_g$ ) and transition energy (from valence band (VB) position to the midgap states), the Kubelka-Munk function was used. As shown in Figure 2-11, compared to the Bulk CN with the bandgap of 2.72 eV, the bandgap of NC MCN was enlarged to 2.8 eV. Furthermore, based on the Kubelka-Munk method, the mid-gap state energy ( $E_m$ ) was estimated to be 2.63 eV. This is in agreement with previous works which mentioned that the midgap states at 0.5-1.0 eV beneath the conduction band minimum are presented in the structure of g- $C_3N_4$  when there are cyano groups and nitrogen vacancies in the structure [100].

The XPS valence band spectra of as-prepared samples are shown in Figure 2-12 a and b. Based on the spectra, the VB position of catalysts is obtained approximately which is 1.5 eV for Bulk CN and 1.8 eV for NC MCN. According to the obtained data from Figure 2-12 b and combined with the VB position calculated from XPS valence band spectra, CB positions, and the band edge of midgap states could be approximately identified. A schematic illustration describing the electronic band configuration of Bulk CN and NC MCN is displayed in Figure 2-12 c. Two main aspects of NC MCN catalyst which directly contribute to its enhanced performance of photodegradation can be observed from this figure. The first one is the more positive value of VB (1.8eV) for NC MCN compared with Bulk CN (1.5eV), which results in the higher oxidation capacity of the produced holes. Secondly, because of the existence of midgap states under the CB of NC MCN, the catalyst can utilize visible light with a longer wavelength to stimulate electrons to the midgap states. Meanwhile, the midgap states can reduce the charge recombination probability at the ground state by temporarily trapping the excited electrons[77].

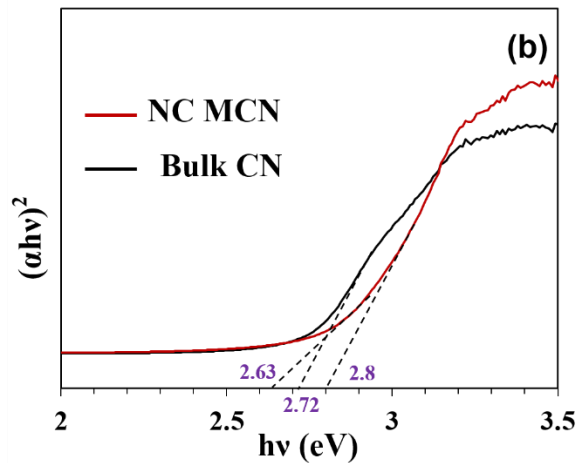


Figure 2-11 The corresponding  $(\alpha hv)^2$  vs  $h\nu$  plots of Bulk CN and NC MCN

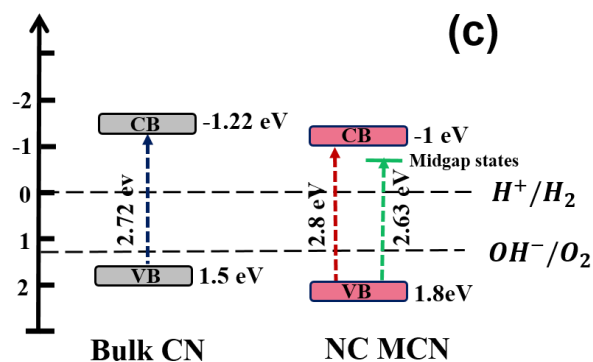
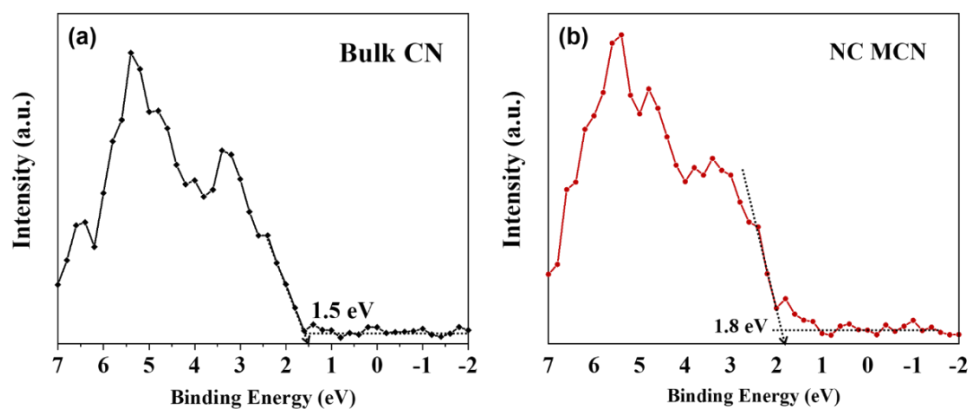
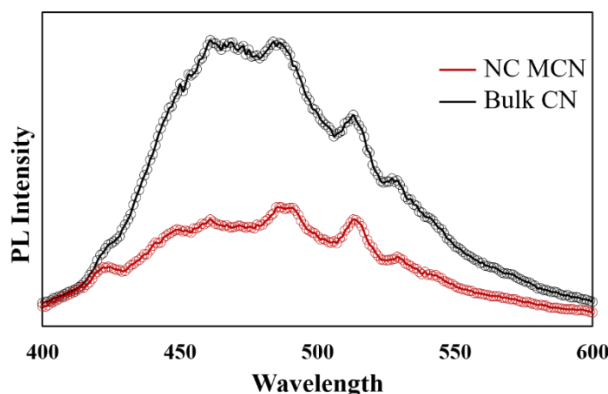


Figure 2-12 XPS valence band spectra (a) Bulk CN, (b) NC MCN; (c) Corresponding band edge positions of both catalysts

### 2.3.4.3 photoluminescence spectroscopy (PL)

Steady-state photoluminescence spectroscopy (PL) is a mighty technique to reveal the charge separation efficiency of the catalyst. As presented in Figure 2-13, the PL spectrum of NC MCN displays much lower intensity compared to Bulk CN, indicating that the reactive recombination of photogenerated electron-hole pairs can be substantially precluded after introducing nitrogen defects. This might happen as the defects introduce midgap states into the structure of NC MCN, which play the role of trapping sites for photogenerated electrons, hence enhancing charge separation.



**Figure 2-13.** PL spectra of Bulk CN and NC MCN

### 2.3.5 Photoelectrochemical properties

Photo-excited charge separation is a crucial factor in the photocatalytic process. To further assess the impact of structural defects on the separation of electron-hole pairs and their transition efficiency, transient photocurrent response of NC MCN and Bulk CN deposited on fluoride-tin oxide (FTO) electrodes were conducted. As demonstrated in Fig. 8a, under repeated on and off cycles of irradiation, NC MCN exhibits higher photocurrent density compared to Bulk CN, demonstrating that nitrogen vacancies enhanced the separation and transfer efficiency of

photogenerated charge carriers[96]. The EIS measurements also reveal similar results. As shown in Fig. 8b, the arc diameter of the Nyquist plot for NC MCN is much smaller than Bulk CN, indicating that NC MCN had much smaller interfacial resistance in charge transfer which favors higher separation and transfer of charge carriers [101]. These results along with PL plots confirm that the existence of defects in the structure of NC MCN decreased recombination of photoinduced charge carriers by introducing midgap states that could be trapping sites for photogenerated electrons.

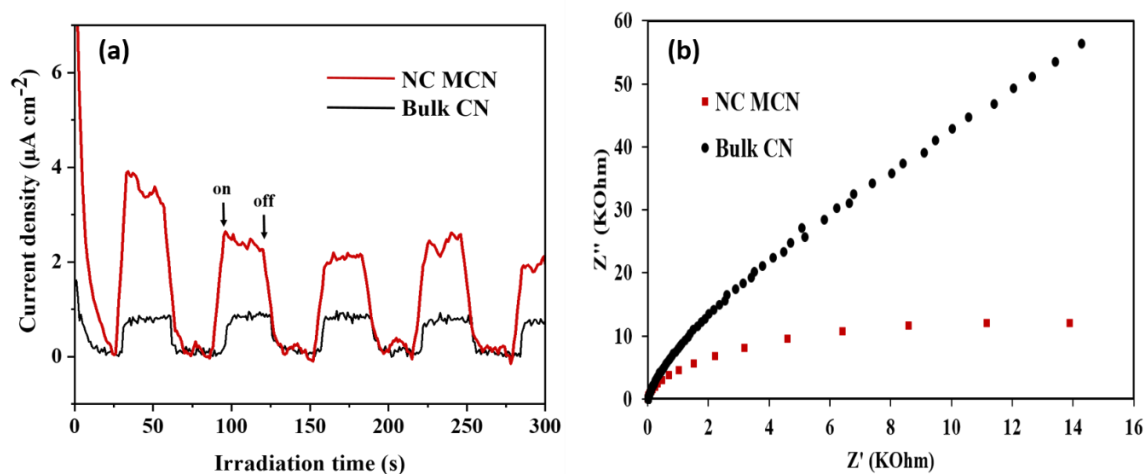


**Figure 2-14.** (a) photocurrent response; (b) EIS Nyquist plots of as-prepared samples

### 2.3.6 Photocatalytic activity for degradation of RhB and TC:

To evaluate the photocatalytic performance of the as-prepared g-C<sub>3</sub>N<sub>4</sub> samples, RhB and TC were selected as the target pollutants. The photocatalytic degradation of the pollutants was conducted under visible light irradiation.

As shown in Figure 2-15, the blank experiments (photolysis) that were induced by visible light turned out negligible degradation of the pollutants as their concentration remained unchanged, confirming that the TC and RhB removal in the presence of the tested catalysts was mainly attributed to the photocatalytic degradation. The function of adsorption and photocatalysis reaction was analyzed individually. In the term of adsorption capacity, after 30 min reaction in the dark condition, NC MCN showed significant enhancement of adsorption in compared to Bulk CN under the same condition, and then adsorption-desorption equilibrium of suspension was acquired completely. It can be observed that the degradation efficiency of Bulk CN for RhB is very low and it takes too much time to completely remove RhB from the solution (Figure 2-15 a). Meanwhile, NC MCN reduced this time significantly, and complete degradation of RhB was achieved within 30 min under visible light irradiation. TC degradation was also studied in the ensuing investigations as shown in Figure 2-15 b. The TC degradation capability of Bulk CN was very poor, with only a small amount of adsorption and a slow elimination rate. However surprisingly, NC MCN showed a very high photocatalytic activity with a degradation rate of more than 70% within 15 min and complete degradation within 30 min, which was proved using LC-MS analysis (section 3.10). Additionally, the photocatalytic degradation data of both pollutants obtained within 25 min was fit to pseudo-first-order kinetic reaction and is computed by Eq. (2)[101].

$$\ln(C_0/C_n) = kt \quad (2)$$

Where  $k$  is the first-order kinetic rate constant ( $\text{min}^{-1}$ ),  $C_0$  and  $C_n$  are the concentration of pollutants at reaction time 0 min and  $n$  min, respectively [101]. In the kinetic plot of RhB degradation represented in Figure 2-15 c, it is obvious that the reaction rate constant of NC MCN ( $0.099 \text{ min}^{-1}$ ) is about 3.9 times higher than that of Bulk CN ( $0.025 \text{ min}^{-1}$ ). The same results were obtained for TC degradation where the reaction rate constant of NC MCN increased about 3.4 times in

comparison to Bulk CN, as shown in Figure 2-15 d. Consequently, NC MCN showed much higher efficiency and capability in the removal of RhB and TC from the solution. The considerably improved photocatalytic performance of NC MCN can be attributed to its larger specific surface area, porous structure, and introduction of nitrogen defects into its structure.

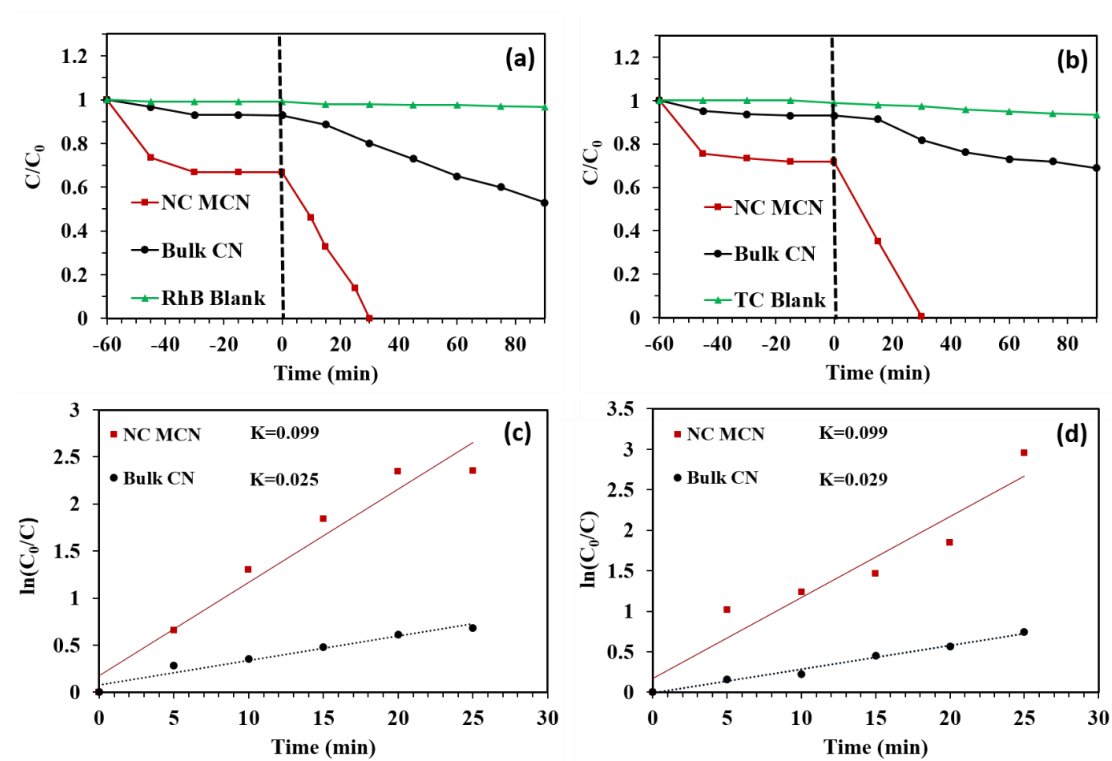


**Figure 2-15.** Photocatalytic degradation curves of (a) Rhodamine B degradation, (b) Tetracycline degradation; pseudo-first-order kinetics curves of photocatalytic degradation for (c) Rhodamine B, (d) Tetracycline

### 2.3.7 Stability and reusability of catalysts

In the process of analyzing the capability of the catalyst for practical applications, its stability and reusability are of considerable importance. Therefore, to investigate the reusability of NC MCN

under visible light irradiation, eight consecutive recycling experiments were performed in the same situation. As demonstrated in Figure 2-16, no apparent deactivation of the NC MCN detected and the TC removal rate did not change noticeably even after eight cycle degradation. Furthermore, as a comparison, the SEM image of the used catalyst was taken and shown in Figure 2-17. It is obvious that the morphology of the NC MCN did not change after its usage. The XRD spectra of the recycled sample are also depicted in Figure 2-18, demonstrating the retained structure of NC MCN after several times utilization. The above result successfully represents that NC MCN has high reusability and stability, and can be used as a stable and efficient photocatalyst for practical application of pollutants photodegradation under visible light irradiation.

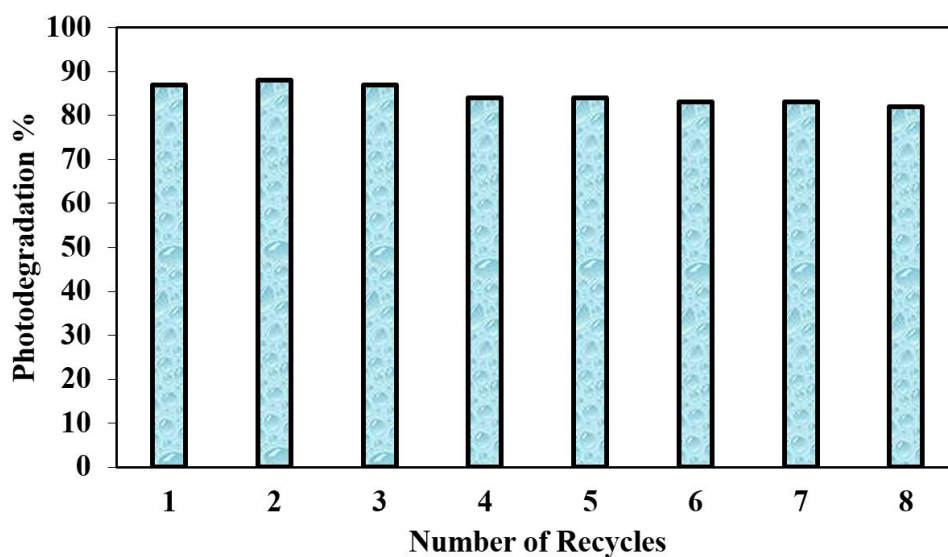


**Figure 2-16.** Photocatalytic stability of NC MCN in the degradation of TC within eight cycles

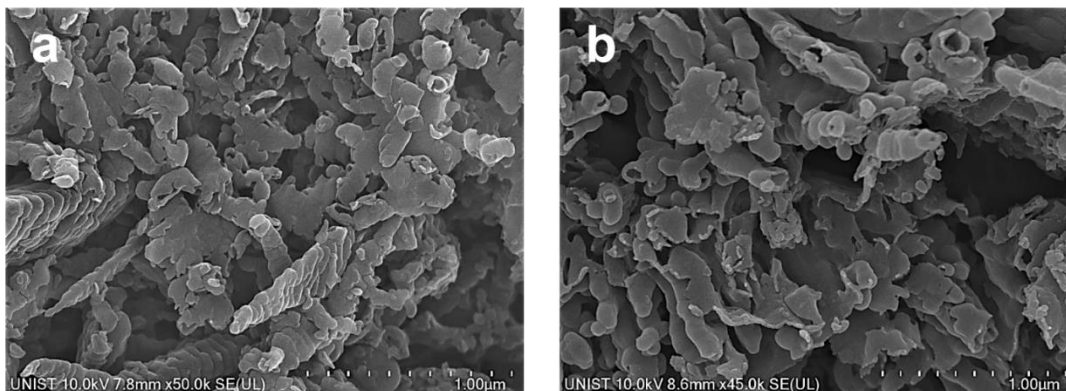


**Figure 2-17.** SEM image of (a) Unused NC MCN and (b) used NC MCN

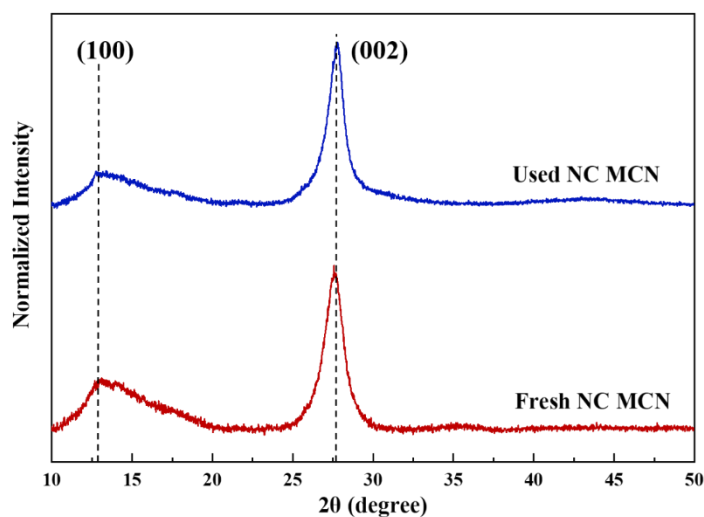


**Figure 2-18.** XRD patterns of fresh NC MCN and used NCMCN

### 2.3.8 Determination of the main reactive species involved in the photocatalytic degradation

Generally speaking, a sequence of reactive species including holes ( $h^+$ ), electrons ( $e^-$ ), superoxide radicals ( $\cdot O_2^-$ ), and hydroxyl radicals ( $\cdot OH$ ) could participate in the process of photocatalytic pollutant degradation. To elucidate the predominant photogenerated reactive species that participated in the degradation of TC over the NC MCN catalyst, a set of comparative experiments



was conducted by selectively adding several scavengers during the photodegradation experiment. Triethanolamine (TEA), isopropyl alcohol (IPA), benzoquinone (BQ), and AgNO<sub>3</sub> were used as the scavengers for (h<sup>+</sup>), (•OH), (•O<sub>2</sub><sup>-</sup>), and (e<sup>-</sup>), respectively. As shown in Fig. 10a, compared to the performance of the catalyst without using scavengers, the degradation of TC was only weakly inhibited after adding AgNO<sub>3</sub>, suggesting that electrons (e<sup>-</sup>) are not the main active species in the photocatalytic process. Also after adding IPA, around 10% reduction in the activity of NC MCN was observed, which shows the minor role of hydroxyl radicals (•OH) in the photodegradation process. However, the photodegradation activity decreased in the presence of TEA and BQ, indicating the leading roles of photogenerated holes (h<sup>+</sup>) and superoxide radicals (•O<sub>2</sub><sup>-</sup>) in the photocatalytic degradation of the TC. Further investigation of the main reactive species was conducted using EPR spin-trap technology. EPR spectra were recorded under the condition of dark and 10 min visible light irradiation using 5,5-dimethyl-1-pyrroline N-oxide (DMPO) as the radical trapping agent. As depicted in Fig. 10b and c, no specific spectrum was observed under dark conditions. However, the apparent signals of the adduct DMPO-•O<sub>2</sub><sup>-</sup> and DMPO-•OH were detected after 10 min visible light irradiation. These results confirm the presence of •OH and •O<sub>2</sub><sup>-</sup> during the photocatalytic process [102]. Meanwhile, compared to the •OH, a higher intensity of •O<sub>2</sub><sup>-</sup> was achieved, which demonstrates the dominating role of superoxide radicals. This is consistent with active species trapping experimental results. Based on the above information, the possible photocatalytic equations can be presented in Eq (3) to (8).



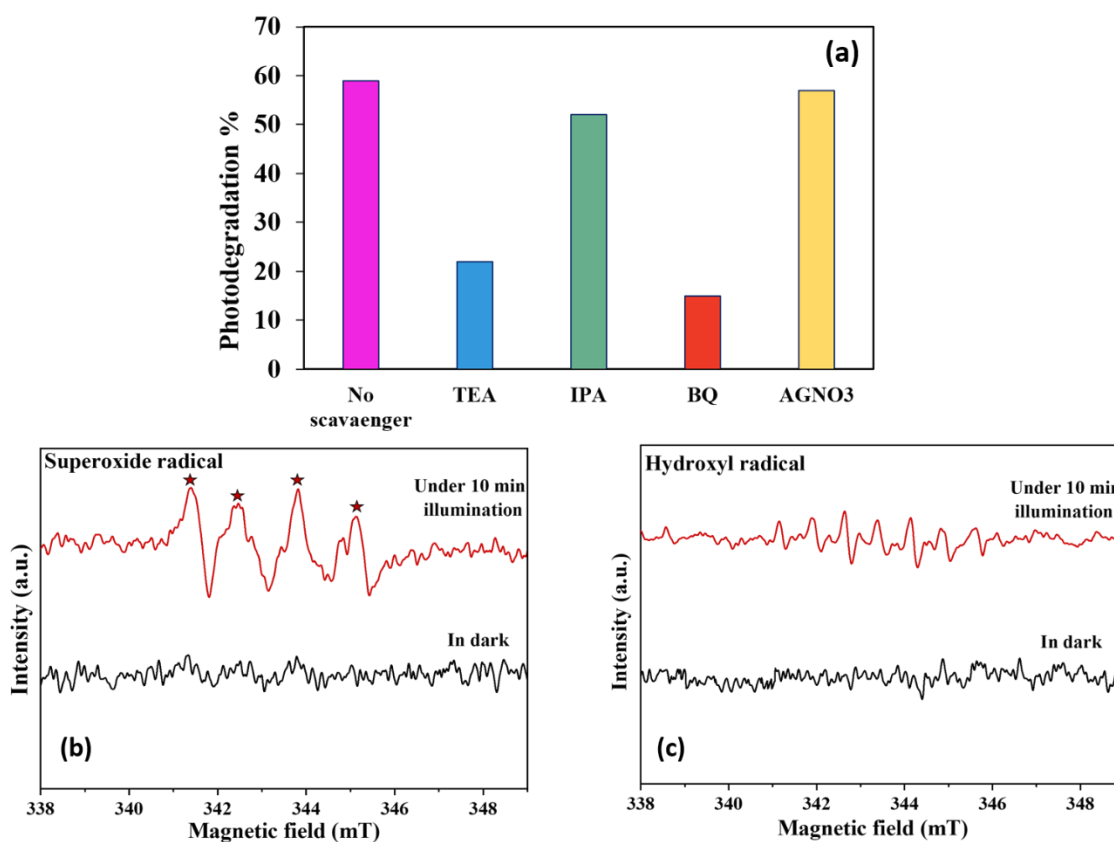


**Figure 2-19.** (a) TC photodegradation percent using NC MCN in the presence of different scavengers; EPR spectra recorded with NC MCN under dark and visible light illumination depicting (b) DMPO  $\cdot\text{O}_2^-$  adducts in methanol solution, (c) DMPO  $\cdot\text{OH}$  adducts in aqueous solution

### **2.3.9 Mechanism of enhanced photocatalysis by NC MCN**

Based on the above outcomes, a mechanism is suggested for the enhanced photocatalytic activity of NC MCN toward the degradation of TC and RhB (Figure 2-20). The process of photocatalytic reactions involves four sequential steps including (i) light-harvesting; (ii) charge excitation and electron-hole pairs generation; (iii) the separation and surface transfer of electron-hole pairs; (iv) surface adsorption and oxidation-reduction reactions. Therefore, in designing NC MCN with excellent photocatalytic ability, integrated engineering has been performed to optimize all these four stages.

Firstly, the higher specific surface area along with the porous structure of NC MCN provides abundant exposed active sites for the surface reactions as well as enhanced mass transfer process, which results in efficient photodegradation of RhB and TC [73]. Furthermore, the mesoporous structure of NC MCN results in more efficient light-harvesting and utilization through the higher accessible surface area compared to the bulk sample [74].

Secondly, the existence of abundant cyano groups and nitrogen vacancies in the structure of NC MCN substantially boost the light-harvesting and charge separation [74, 76, 77]: 1) These structural defects introduced midgap states within the bandgap, below the conduction band. In the presence of midgap states, besides excitation to the conduction band, electrons can also be excited to the midgap states by absorption of photons with longer wavelengths. Thus, the resulting visible light-harvesting ability has been improved significantly. 2) The mid-gap energy states under the conduction band of NC MCN can trap the electrons excited to the conduction band and also prevents their recombination with holes in the valence bands, consequently decreasing the recombination rate of photogenerated charges. The trapped electrons then will react with dissolved

oxygen in the water to fabricate superoxide radicals, which played a leading role in RhB and TC degradation.

Finally, the VB edge potential of NC MCN is more positive compared to the bulk one, implying that this catalyst has a much better oxidation ability, thus leading to higher photodegradation capability.

Therefore, it could be confirmed that the as-synthesized NC MCN in this study, exhibited distinguished activity in all four steps, which resulted in the remarkable photocatalytic activity in the degradation of TC and RhB.

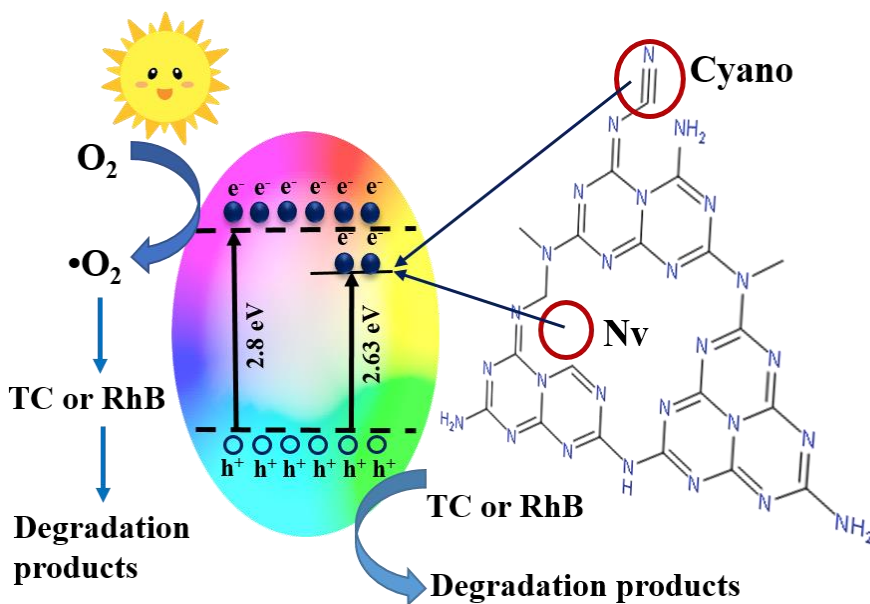


Figure 2-20. Schematic illustration of TC and RhB photocatalytic degradation over the NC MCN

### 2.3.10 Possible mechanism of photocatalytic degradation

To identify the plausible degradation pathway and produced intermediates during the photocatalysis process at different irradiation times, LC-MS techniques were employed. Figure 2-21 1, b, and c show the LC-MS spectra of the parent TC and photocatalytic degradation products after 15 min and 30 min irradiation ( $\lambda \geq 400$  nm). From the spectra, it can be observed in Figure 2-21 d that the intensity of the TC signal (with  $m/z=445$ ) at an elution time of 2.8 min, decreased enormously after 15 min illumination and almost disappeared after 30 min, indicating the decomposition of TC structure. The plausible TC photodegradation pathways are proposed and demonstrated in Figure 2-22. The product TC with  $m/z$  445 corresponded to the molecular weight of tetracycline which can be possibly degraded from three main pathways.

**Pathway I:** Due to the low energy of the N-C bond, P1 ( $m/z=433$ ) was derived from TC fragmentation via loss of one N-methyl group from dimethylamino [103]. Then oxidation of P1 results in the formation of P2 ( $m/z=431$ ). Further degradation led to the loss of another methyl group and the generation of the intermediate P3 ( $m/z=417$ ) [104]. Moreover, dehydration of C6 and replacement of the acylamino by the carbinol group at C<sub>2</sub> the intermediate of P4 ( $m/z=392$ ) has appeared. The photodegradation via pathway I can be simply summarized in the terms of molecular weight as follow: 445→433→431→417→392.

**Pathway II:** This pathway was initiated with ammonia loss from the TC backbone leading to the production of P5 ( $m/z=446$ ) [105] following by dehydration and production of P6 ( $m/z=410$ ). Next, it can be confirmed that the intermediate P7 ( $m/z=362$ ) was derived due to the destruction of methyl groups. Using molecular weight, the photodegradation pathway II could be expressed as follow: 445→446→410→362.

**Pathway III:** This pathway is induced by preferential reaction of C11a-C12 double bond with active radicals and a rearrangement with the hydroxyl at the position of C<sub>12</sub>, giving birth to P8

( $m/z=461$ )[106]. Then further oxidation of double bond C<sub>2</sub>-C<sub>3</sub> of P8 structure resulted in the production of P9 ( $m/z=477$ ) [107]. Subsequently, P10 ( $m/z=449$ ) was generated by losing methyl groups from P9. Next, the ring of P10 was opened due to the breaking of N-CH<sub>3</sub> and C-NH<sub>2</sub> as the C-N bond has a relatively high electron concentration (corresponding low bond energy) and the peak of small molecule P11 ( $m/z=309$ ) raised [108]. The possible degradation pathway III can be briefly showed utilizing molecular weight as follows: 445→461→477→449→309. Further proceeding of reactions for all three pathways resulted in the formation of small organic molecules such as products with  $m/z=279$ , 249, 232, 195, 168, 150, 118, through a series of open-ring reactions and the loss of functional groups. Eventually, these small molecules were oxidized and decomposed into H<sub>2</sub>O and CO<sub>2</sub>.

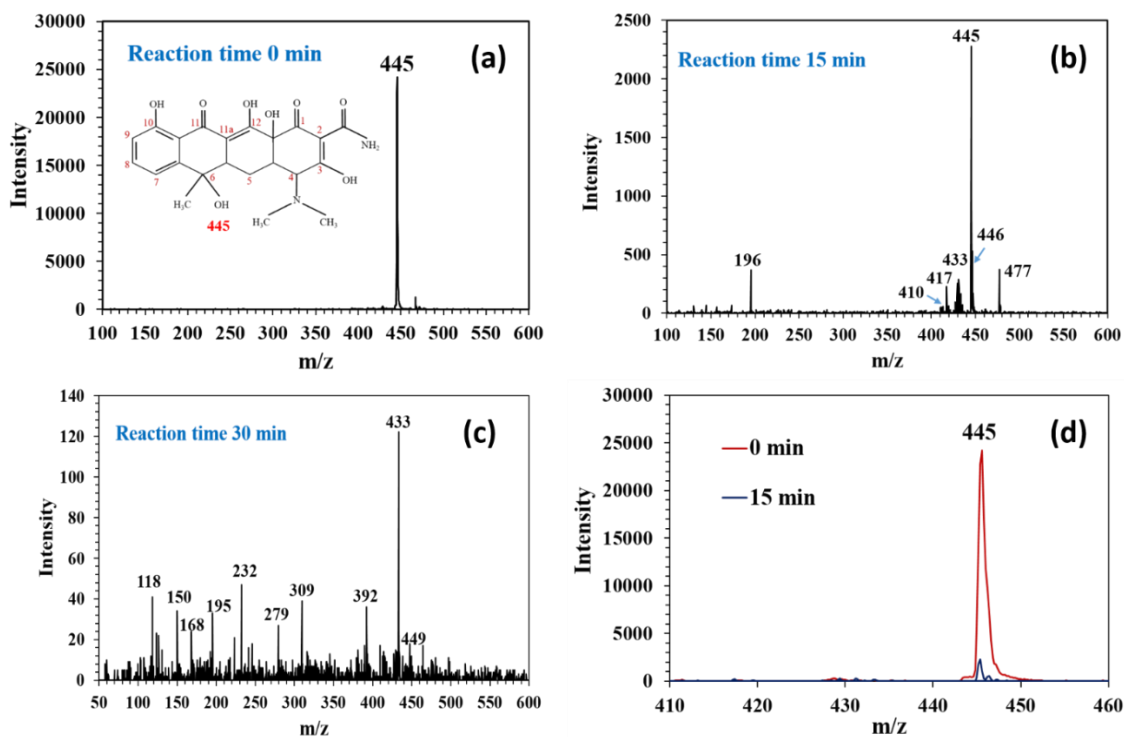


**Figure 2-21.** LC-MS chromatograms of (a) TC; and produced intermediates at (b) photodegradation reaction time 15 min;(c) photodegradation reaction time 30 min;(d) comparison of TC intensity without reaction and after 15 min reaction time

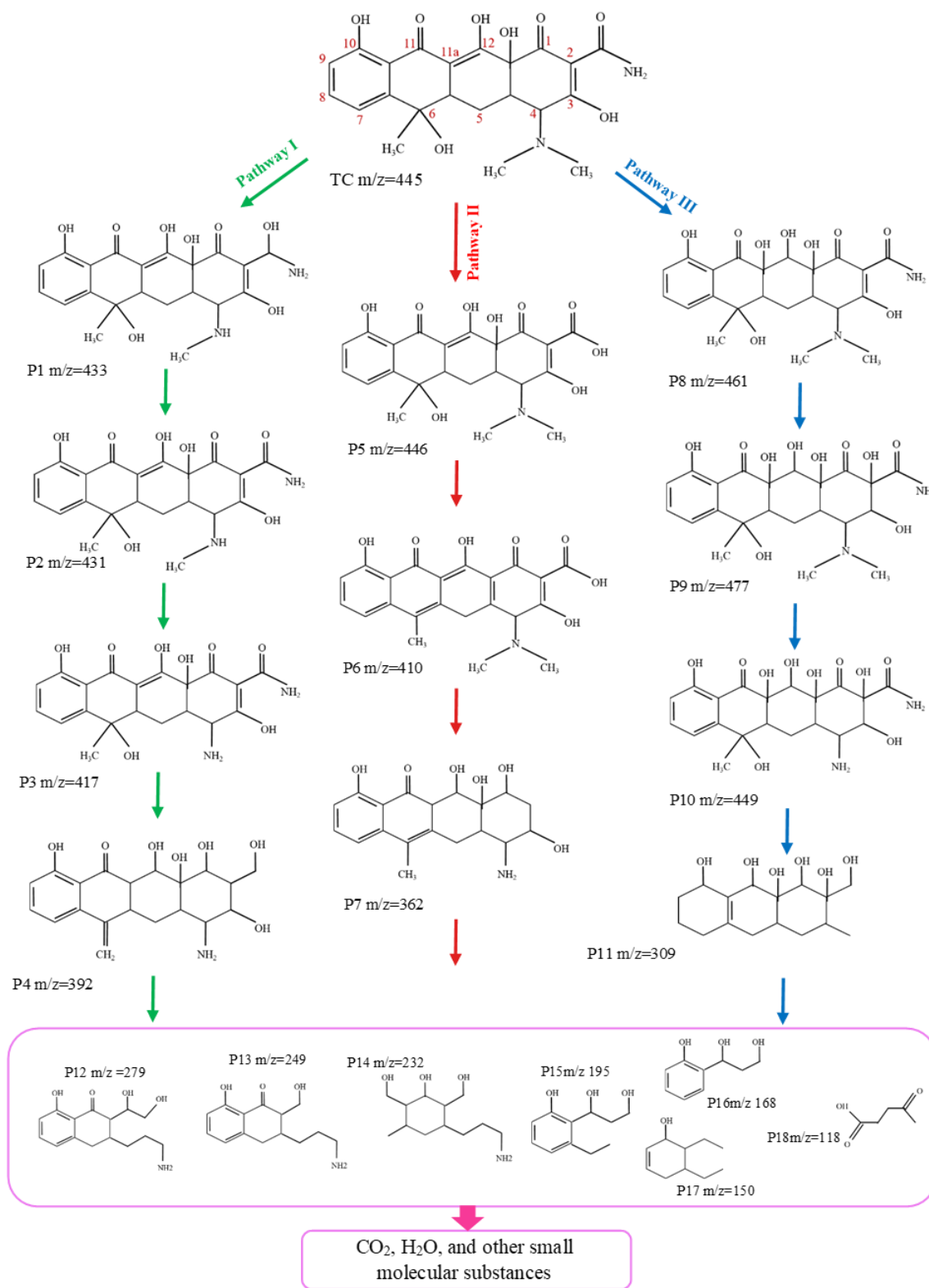


**Figure 2-22.** Proposed intermediate production pathways during photodegradation of TC



### 2.3.11 Mineralization analysis

To investigate the mineralization ability of catalysts, the reduction of TOC during the TC photodegradation process over NC MCN and Bulk CN was recorded. As is shown in Figure 2-23, for Bulk CN, the TOC removal rate was so slow in which after 90 min irradiation, TOC concentration was decreased by 20%. For NC MCN however, more than 70% of TOC removed after 90 min irradiation with an increasing and then decreasing trend. It should be noted that the TOC removal from the solution only happens when TC is physically eliminated from the solution, either by adsorption, or complete mineralization to carbon dioxide or water [109]. For more clarification, the spectra of TC photodegradation in different reaction time were analyzed. After a 60 min-reaction in the dark, the TC concentration was decreased and similarly, TOC of the solution was reduced by 20% which is due to the adsorption of TC on the NC MCN (Figure 2-23 b). Then after 30 min irradiation, the TOC increased by about 16%. As shown in the spectra of TC after 30 min irradiation in Figure 2-23 c, the absorption peak at the wavelength 300-400 nm was completely disappeared, while the absorbance of the solution at the wavelength 200-275 increased [110]. There are four connected rings in the TC structure (Figure 2-24), in which ring A represents absorption band at 250-300 nm, and rings BCD contribute to absorption bands of 250-300 nm and 340-380 nm [111]. Accordingly, the destruction of the BCD rings resulted in the 300-400 nm peak disappearance, and the intermediate products caused the enhancement in the absorption bands at 200-275 nm. Thus, although after the 30 min irradiation the TC structure completely degraded, small molecules were produced and entered into the solution, which caused the enhancement of TOC [110]. By prolonging the reaction time, the absorbance of the solution reduced (Figure 2-23 c) and TOC decreased very much (Figure 2-23 a), which showed high mineralization capability of NC MCN in comparison to the Bulk CN.

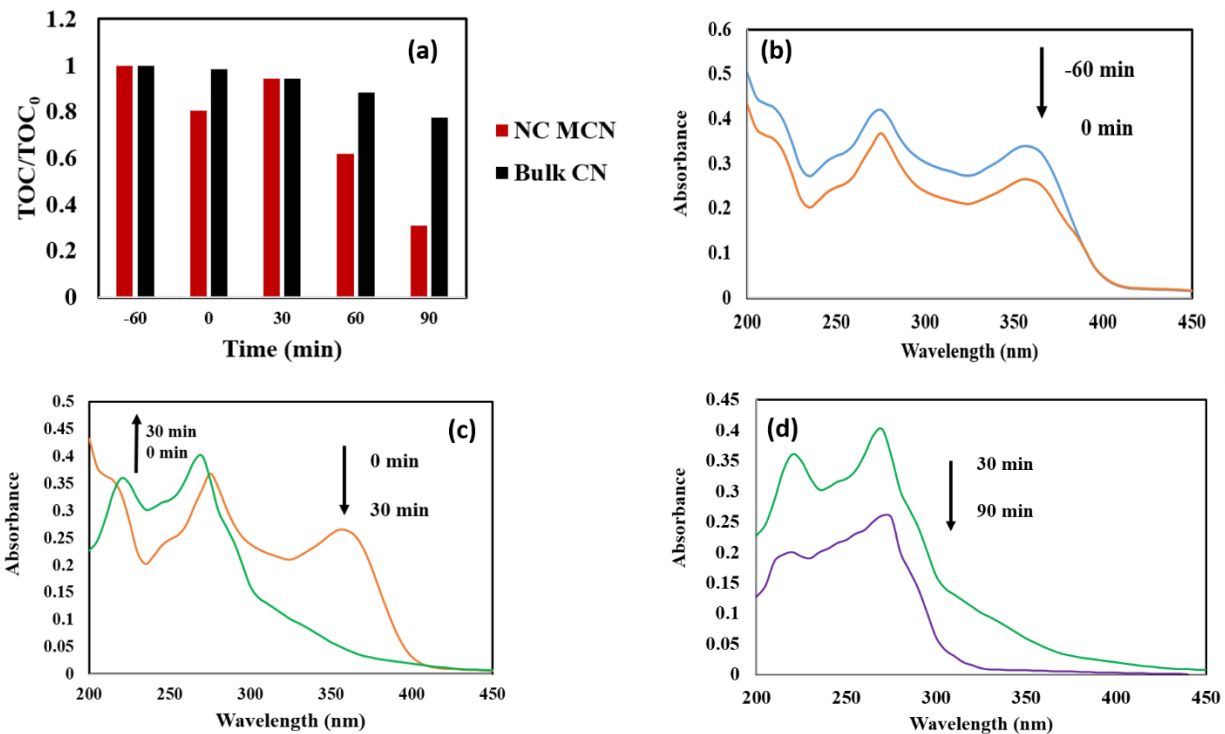


**Figure 2-23.** (a) Removal of TOC as a function of time for tetracycline degradation using as-prepared photocatalysts, Spectra of TCs photodegradation solutions at different reaction time: (b) -60 to 0 min; (c) 0-30 min; (d) 30-90 min

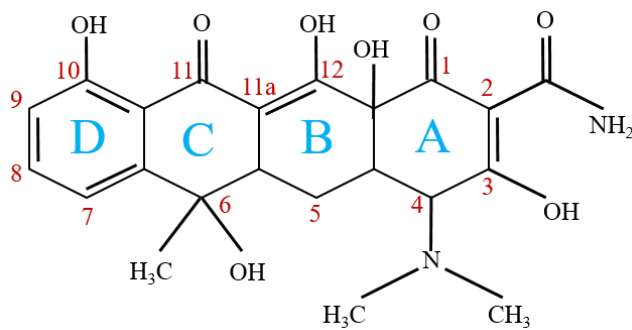


**Figure 2-24.** Molecular structures of the tetracycline

### 2.3.12 Toxicity evaluation

It could be observed that different intermediates were produced as the TC was degraded and each of them with its specific properties could influence the water body differently. As a result, in the process of water purification, exploring the toxicity of produced intermediates is of great importance. So to analyze the toxicity of TC and its produced photodegradation intermediates, the acute toxicity, bioaccumulation factors, developmental toxicity, and mutagenicity of these organic materials were estimated. This estimation was conducted based on the quantitative structure-activity relationship (QSAR) method by using the Toxicity Estimation Software Tool (T.E.S.T.) [112, 113]. As exhibited in Figure 2-25 a, The LD<sub>50</sub> value of TC for rats is 806.96 mg.kg<sup>-1</sup>, which is evaluated as “very toxic”. Besides P12 and P13, all other intermediates showed a higher value of LD<sub>50</sub> compared to TC, confirming that the acute toxicity of the intermediates was decreased. Even though P12 and P13 are highly toxic, the main ultimate intermediates of TC are P16, P17, and P18 which have a higher value of LD<sub>50</sub> and lower toxicity than TC. Moreover, although the bioaccumulation factor of most intermediates is higher than TC, the final product of P18 has a lower bioaccumulation factor which is favorable (Figure 2-25 b). It can be observed from Figure 2-25 c that the developmental toxicity of produced all intermediates are lower than TC except for P3. Interestingly, the developmental toxicity of P4, P9, P10, P14, and P16 are so close to the developmental non-toxic region. Furthermore, TC is “mutagenic positive” and some intermediates have a higher value of mutagenicity, but the final intermediates from P11 to P18 must be in the range of negative mutagenicity and much lower than TC (Figure 2-25 d). Based on the above discussion, the toxicity of most of the produced intermediates decreased during irradiation of visible light. However, as it is necessary to obtain a complete non-toxic solution, prolonging the photocatalytic reaction time is desired to purify contaminated water.

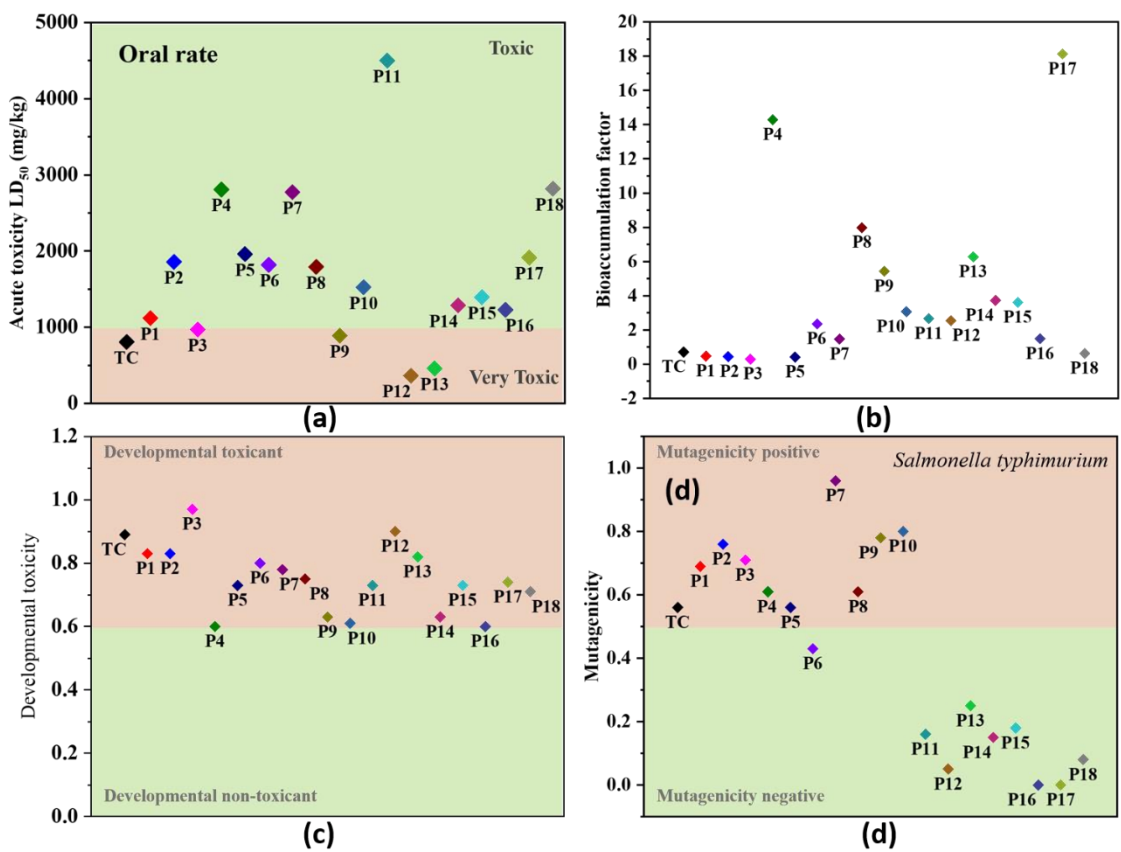


**Figure 2-25.** Toxicity assessment results of TC intermediates produced under photocatalytic degradation using NC MCN (a) acute toxicity LD<sub>50</sub>; (b) Bioaccumulation factor; (c) developmental toxicity (d) mutagenicity

## 2.4 Conclusion

In facing the world-wide challenge of wastewater treatment, photocatalytic degradation of organic pollutants under visible light is considered a great opportunity. In this study, a mesoporous graphitic carbon nitride with significant visible light activity was synthesized using melamine precursor and silica clusters as the sacrificial hard template. The confined growth of g-C<sub>3</sub>N<sub>4</sub> planes in the presence of silica templates resulted in higher surface area and mesoporous structure and consequently more active sites and enhanced light-harvesting capability of NC MCN. Structural defects (N vacancy and cyano groups) were introduced into the structure of NC MCN which produced midgap states into the electronic structure of the catalyst. The midgap states caused more efficient light-harvesting with higher wavelengths and prohibited recombination of photo-excited charge carriers by acting as trapping sites for electrons. In summary, enhancing light-harvesting, increasing active sites, and reducing photogenerated electron-hole recombination were the main factors that boosted the photocatalytic activity of the NC MCN. Consequently, with these superior characteristics, NC MCN could degrade TC and RhB in a very short time. The stability and reusability of the catalyst were also tested within eight cycles of photodegradation experiments. No significant reduction in the activity of the catalyst was observed, and its structure and morphology were also retained. The main reactive species involved in the photocatalytic reaction were determined using active species trapping experiments and EPR spectra, which showed the leading role of photogenerated holes (h<sup>+</sup>) and superoxide radicals (<sup>•</sup>O<sub>2</sub><sup>-</sup>) in the photocatalytic degradation process. The TOC of solution at different reaction times were consistent with the three main steps of the photodegradation process, i.e. adsorption, photodegradation, and mineralization. Moreover, using LC-MS analysis, the produced intermediates of TC during photocatalytic degradation were proposed in detail through three different pathways. Then using QSAR

prediction, the toxicity of all intermediates was estimated and presented. TC is mutagenicity positive, but the final obtained products were mutagenicity negative. Finally, the results of the bioaccumulation factor, acute toxicity, and developmental toxicity presented that the toxicity of TC intermediates was reduced after visible light photodegradation.

Based on the current findings, this comprehensive study in the construction of mesoporous g-C<sub>3</sub>N<sub>4</sub> with defects and its capability in the degradation, mineralization, and toxicity reduction of TC is expected to facilitate the way of producing highly efficient photocatalyst in the application of wastewater and environmental pollution remediation.

# Chapter 3- Construction of Hierarchical Inverse Opal g-C<sub>3</sub>N<sub>4</sub>

## 3.1 Introduction

One way to improve the activity of g-C<sub>3</sub>N<sub>4</sub> is to control its morphology, size and hence enhance its active reaction sites. In this study, by using SiO<sub>2</sub> nanoparticles as the sacrificial template (with an average size of 300 nm) which was synthesized using the stober method, we successfully fabricated a hierarchical inverse opal structure for g-C<sub>3</sub>N<sub>4</sub>. The inverse opal g-C<sub>3</sub>N<sub>4</sub> showed superior activity toward the degradation of different kinds of organic pollutants, such as bisphenol a, tetracycline, methylene blue, and rhodamine B. However, the degradation time and efficiency for these four pollutants were different which is discussed in detail in this study

## 3.2 Experimental section

### 3.2.1 Synthesis of materials

#### 3.2.1.1 Preparation of SiO<sub>2</sub> microspheres

Uniformly dispersed silica microspheres with a diameter of around 320 nm were synthesized based on the well-known StÖber method. In detail, solution A contained 154 ml aqueous ammonia, 304 ml ethanol, and 370 ml deionized water mixed together in a stirrer for 10 min. Solution B, containing 683 ml ethanol and 67 ml tetraethoxysilane (TEOS) was added to solution A in about 1 min, while the solution was in intensive stirring (800 r/min). After that, the solution was kept under magnetic stirring (400 r/min) for 16 h to allow growth of silica particles. The white precipitate was then collected by centrifugation (11000 rpm), washed with water and ethanol 3 times, mixed with 100 ml ethanol and sonicated for 15 min, then dried in oven at 100 °C. Eventually, the as-prepared white solid was ground in a mortar and was heated in the air from room temperature to 550 °C in 4 h and kept at this temperature for 6 h to achieve monodispersed silica microspheres. A schematic illustration of SiO<sub>2</sub> synthesis process is shown in Figure 3-1.

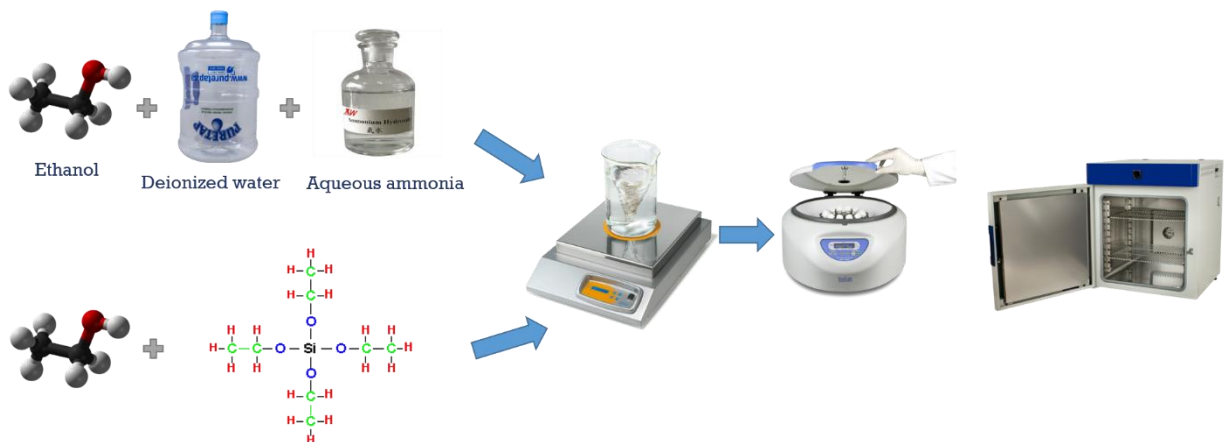


**Figure 3-1.** Schematic illustration of SiO<sub>2</sub> microsphere synthesis



### 3.2.1.2 Synthesis of inverse opal g-C<sub>3</sub>N<sub>4</sub>

Cyanamide was used as the precursor to synthesize inverse opal structure of g-C<sub>3</sub>N<sub>4</sub>. At first, 1.5 g cyanamide was put in a ceramic plate and was stirred at the temperature of 80 °C until melted it was melted. Then, specific amount of SiO<sub>2</sub> microspheres were added gradually to the melted cyanamide while mixing. This solution was then kept mixing for about 30 min in the same temperature (80 °C). After that, the mixture was cooled, grounded and transferred to a crucible for calcination. The crucible was heated in a muffle furnace in air at 550 °C for 2 h with a ramping rate of 2.2 °C/min. The resultant yellow sample of g-C<sub>3</sub>N<sub>4</sub>/SiO<sub>2</sub> hybrids were mixed with 40 ml of 4 M ammonium hydrogen difluoride for 48 h to completely remove the SiO<sub>2</sub> hard template. The suspension then washed with distilled water several times to the point that the PH reached 7, and then dried in oven at 80 °C for 24 h. The obtained catalysts were denoted as IO CN-x, where x act as the mass ratio of silica template-to-cyanamide, which were IO CN-0.5, IO CN-1, IO CN-2. As a control catalyst for this research, Bulk g-C<sub>3</sub>N<sub>4</sub> was synthesized by calcining cyanamide without silica particles in the same heat treatment approach, which was represented by Bulk CN. A schematic illustration of IO CN synthesis is shown in Figure 3-2.

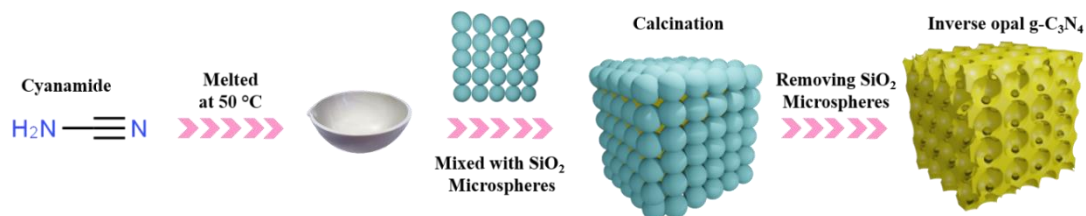


**Figure 3-2.** Schematic illustration of inverse opal g-C<sub>3</sub>N<sub>4</sub> synthesis

### 3.2.2 Characterization

The verification of the morphology of the samples was conducted using field emission scanning electron microscopy (FE-SEM) and transmission electron microscopy (TEM). The powder X-ray diffraction (XRD) patterns of the as-prepared samples were obtained with a Bruker/D8 (Advance model) diffractometer in the  $2\theta$  range of 10.0 to 80° using steps of 0.1-degree operating with Cu K $\alpha$  radiation as the X-ray source. Fourier transform infrared (FTIR) spectra were obtained utilizing Varian 670/620 spectrometer to investigate structural characterization. Solid-state  $^{13}\text{C}$  magic angle spinning (MAS) nuclear magnetic resonance (NMR) spectra of catalysts were recorded on a Bruker NVMRS 600 MHz solid-state NMR spectrometer at room temperature. The surface chemical compositions were determined with X-ray photoelectron spectroscopy (XPS) utilizing a Thermo Fisher Scientific spectrometer equipped with a monochromated Al-K $\alpha$  X-ray source. UV-vis diffuse reflection spectroscopy (UV-vis DRS) was performed using a Carry 5000 UV-vis DRS-Agilent-Model spectrophotometer in a spectral range of 200–800 nm. The photoluminescence (PL) spectra were recorded using Cary Eclipse (Model NF900 (FLS920)) photoluminescence detector with a 340 nm excitation wavelength. The Brunauer-Emmett-Teller (BET) surface areas and the distribution of pores of the samples were analyzed by N $_2$  porosimetry using Micromeritics Instruments (Model ASAP2020 Analysis). The electrochemical impedance spectroscopy (EIS) was investigated in the frequency range of 0.05 Hz to 100 kHz at 0.6 V (vs. Ag/AgCl) in Na $_2$ SO $_4$  solution under light illumination. To obtain the concentration of the organic pollutants at different time intervals, UV-vis spectroscopy equipment (Thermo Fisher Scientific, model: G10S UV-Vis) was employed. Electron paramagnetic resonance (EPR) was conducted using a Bruker model EMX-12 spectrometer with  $f=9.64$  GHz. To estimate the intermediates and the probable transform pathways of TC degradation, liquid chromatography-mass spectroscopy (LC-MS) was used.

### 2.2.3 Evaluation of the photocatalytic performance

To obtain the photocatalytic performance of the as-synthesized g-C<sub>3</sub>N<sub>4</sub> samples for degradation of four different organic pollutants of TC, RhB, MB, and BPA, the experiments were conducted under visible light irradiation, and for the light source, a 300 W xenon lamp (with installed UV cut-off filter and an IR water filter ( $400 < \lambda < 800$  nm)) was used. Typically, before the photocatalytic test, 15 mg of the catalyst was mixed with 15 mL aqueous solution of the organic pollutant with a concentration of 15 mgL<sup>-1</sup>. Before irradiation, the mixture was stirred for 15 min in the dark situation to allow the solution and the catalyst to attain adsorption-desorption equilibrium. Afterward, the light turned on and the mixture was irradiated while stirring. During the photocatalytic reaction, the solution was withdrawn every 15 min and centrifuged at the speed of 4000 rpm for 10 min, and the remaining concentration of the pollutant was measured and determined using a UV-Vis spectrometer. The following equation shows the photocatalytic degradation efficiency (PDE) of various organic pollutants.

$$\text{PDE} = (C_0 - C_n) / C_0 \times 100\% \quad (1)$$

Where  $C_0$  (mgL<sup>-1</sup>) is the starting concentration of RhB, TC, MB, or BPA, and  $C_n$  is the concentration of pollutant after the irradiation time of  $t$ .

### 3.3 Results and discussion

#### 3.3.1 SEM and TEM images

To explore the morphology and microscopic structure of silica clusters and synthesized materials, SEM and TEM were implemented. The SEM image of SiO<sub>2</sub> microspheres in the average size of 300 nm is shown in the Figure 3-3 a which confirms the construction of uniform spherical shape. Figure 3-3 b shows the SEM image of inverse opal g-C<sub>3</sub>N<sub>4</sub> which was synthesized using the cyanamide/SiO<sub>2</sub> mass ratio of 1/0.5. Figure 3-3 c is for cyanamide/SiO<sub>2</sub> mass ratio of 1/1, and Figure 3-3 and e are for cyanamide/SiO<sub>2</sub> mass ratio of 1/2 which shows much higher uniform structure. Also Figure 3-3 f shows the TEM image of IO CN 1:2 which is considered as the best sample with uniform porosity.

#### 3.3.2 BET analysis

To analyze the surface properties and porosity of the catalysts, the nitrogen adsorption–desorption measurements were conducted (Figure 3-4). The obtained plot of both catalysts revealed a typical IV-type isotherm with an H3 hysteresis loop in the range of 0.4–0.95 P/P<sub>0</sub> based on the International Union of Pure and Applied Chemistry (IUPAC) classification, confirming the presence of mesoporous structure. The BJH pore size distribution also clearly exhibits that IO CN 1:2 possesses very abundant mesopores in the range from 2 to 80 nm compared with the other samples. The BET specific surface area, pore diameter, and pore volume of the samples are summarized in Table 3-1. Consistently, IO CN3 exhibited a specific surface area of 66.77 m<sup>2</sup> g<sup>-1</sup> and pore volume of 0.25 cm<sup>3</sup> g<sup>-1</sup>, which are much higher than other samples. These data illustrate that using silica microspheres as hard templates could significantly produce a hierarchical mesoporous structure with enhanced surface area and enlarged pore volume.

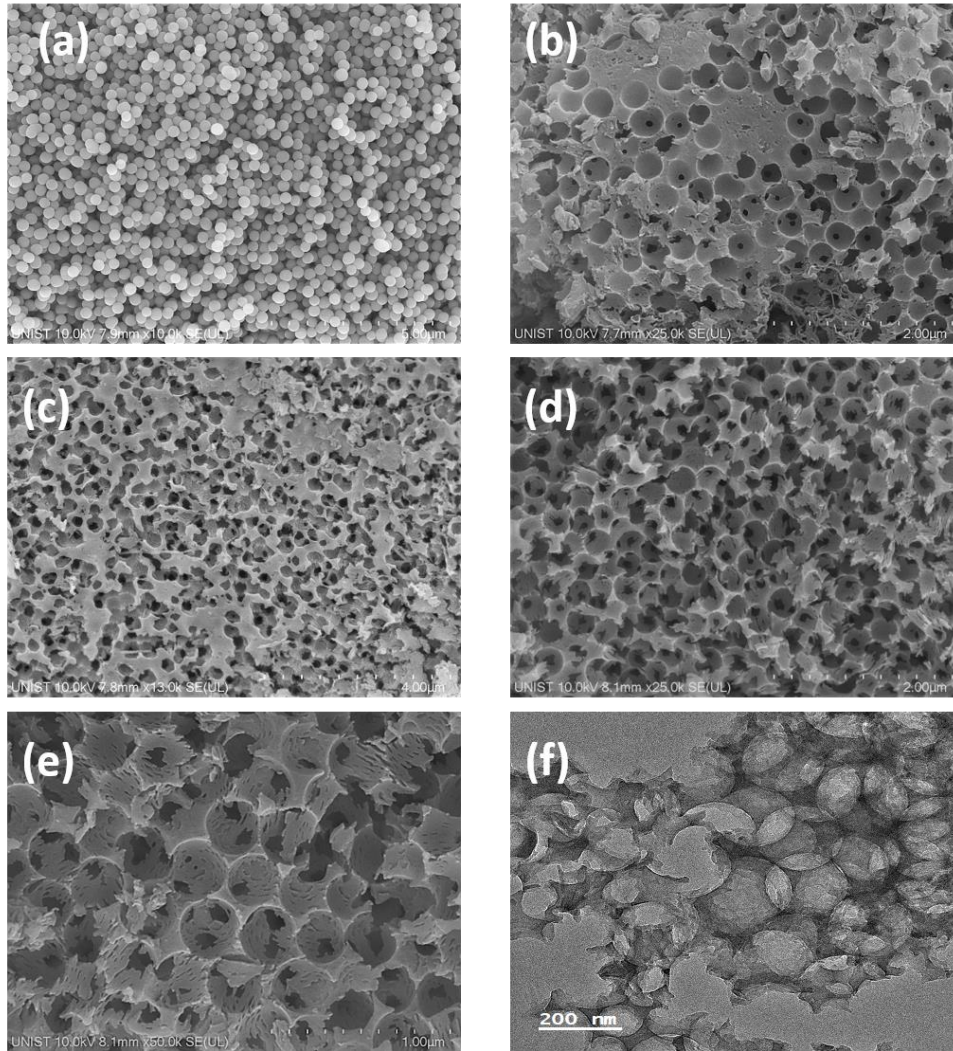


**Figure 3-3.** SEM and TEM images of synthesized samples

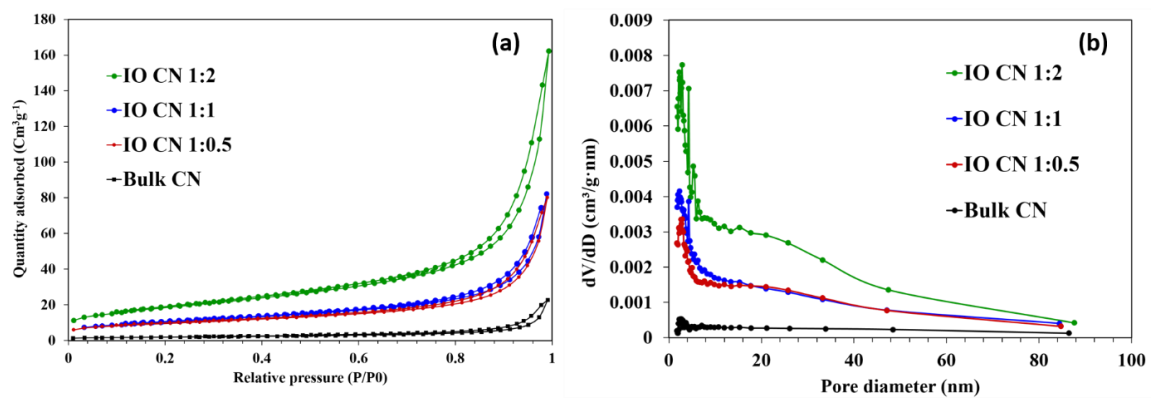


**Figure 3-4.** (a) N<sub>2</sub> adsorption/desorption isotherms (b) The corresponding pore size distribution curves Bulk CN.

**Table 3-1** BET results

Sample	Pore volume (cm <sup>3</sup> g <sup>-1</sup> )	Pore diameter (nm)	BET surface area(m <sup>2</sup> g <sup>-1</sup> )
IO CN3	0.25	15	66.77
IO CN2	0.12	13.56	37.5
IO CN1	0.12	14.8	33.34
Bulk CN	0.035	21.43	6.5

### 3.3.3 Crystal structure and chemical composition

The crystalline nature and chemical structure of synthesized catalysts were explored via XRD measurements as depicted in Fig. 22. The representative XRD spectra of all samples exhibit two diffraction peaks at  $2\theta$  values around  $27.3^\circ$  and  $13.1^\circ$ , which could be attributed to the (002) and (100) reflections. The former peak is corresponded to interlayer stacking of carbon nitride aromatic system, while the latter could be ascribed to in-plane structural packing motifs, respectively.

FT-IR spectra of as-obtained Bulk CN and IO CNs shown in Fig. 22b verify that all samples represent the typical graphitic-like construction of g-C<sub>3</sub>N<sub>4</sub>. The sharp peak at around  $809\text{ cm}^{-1}$  is ascribed to the out-of-plane bending mode of heptazine rings. The group peaks located in the  $1000\text{--}1700\text{ cm}^{-1}$  region are attributed to C-N aromatic heterocycles. The broad peaks in the range of  $3000$  to  $3600\text{ cm}^{-1}$  are associated with stretching vibration of N-H bonds.

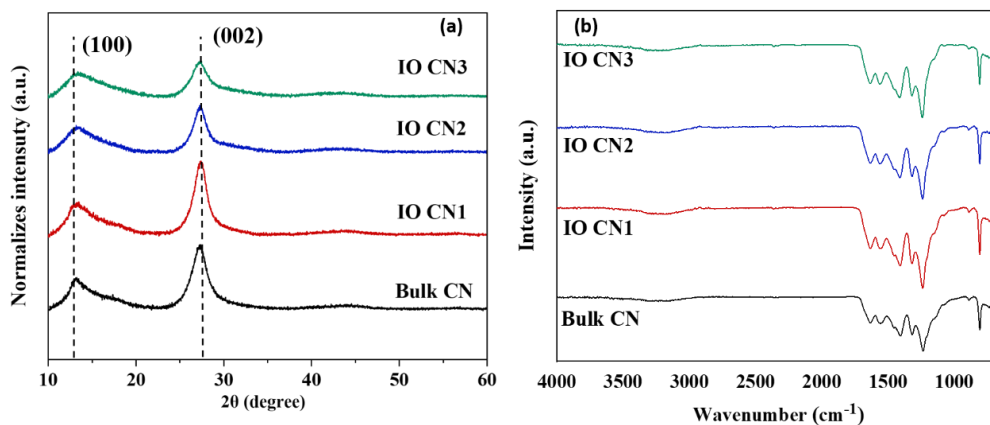


**Figure 3-5.** (a) X-ray diffraction (XRD) patterns, (b) FTIR spectra

### 3.3.4 Optical properties

In terms of the exploitation of solar energy, it is of great significance to expand light-absorption for the photocatalyst, to produce more photoinduced charge carriers for subsequent redox interactions. Thus, the optical absorption characteristics of photocatalysts were analyzed using UV-vis DRS spectra as presented in Figure 3-6. The absorption edge of all samples is located at 480 and 500 nm, confirming that all as-prepared g-C<sub>3</sub>N<sub>4</sub> photocatalysts are active in the visible light region. Compared to other catalysts, IO CN3 exhibited a slight blue shift, indicating the enlargement of the bandgap due to the quantum confinement effect induced by the creation of nanoring morphology [114]. On the contrary, IO CN3 showed an increased visible light-harvesting capability in the entire visible-light spectrum. This is primarily ascribed to the multiple scattering of the incident light in the pores structure of IO CN3, as well as the highly available surface area of this catalyst [59].

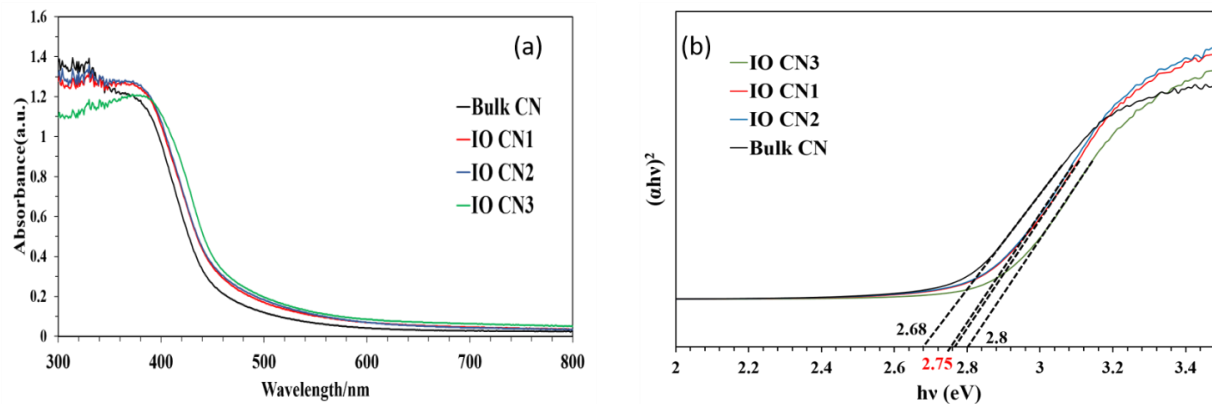


**Figure 3-6.** (a) UV-Vis diffuse reflectance spectra; (b) the corresponding  $(\alpha h\nu)^2$  vs  $h\nu$  plots of prepared samples

### 3.4 Photodegradation results

#### 3.4.1 Photocatalytic degradation of MB

The blank experiment (without using the photocatalyst) under visible light irradiation showed trivial degradation for MB, confirming that pollutant removal from the solution in the presence of prepared photocatalysts was mainly due to the photocatalytic degradation process. In terms of the adsorption capacity of the samples during the reaction, IO CN3 showed higher adsorption of pollutants compared to other samples.

After an approximately 60 min reaction without irradiation (in the dark condition), the equilibrium of adsorption-desorption was achieved. Thus, further removal of the MB after the 60 min adsorption experiment was mainly attributed to photocatalytic degradation. As presented in Figure 3-7 b, the Bulk CN, showed the lowest performance in terms of MB degradation, and only 45% of the pollutant was removed after 200 min of visible light irradiation. The IO CN1 and IO CN2 showed almost the same photodegradation results, and their ability was improved compared to that



of the Bulk CN. Meanwhile, IO CN3 had the best performance which could completely degrade MB in a 110-min photocatalytic reaction.

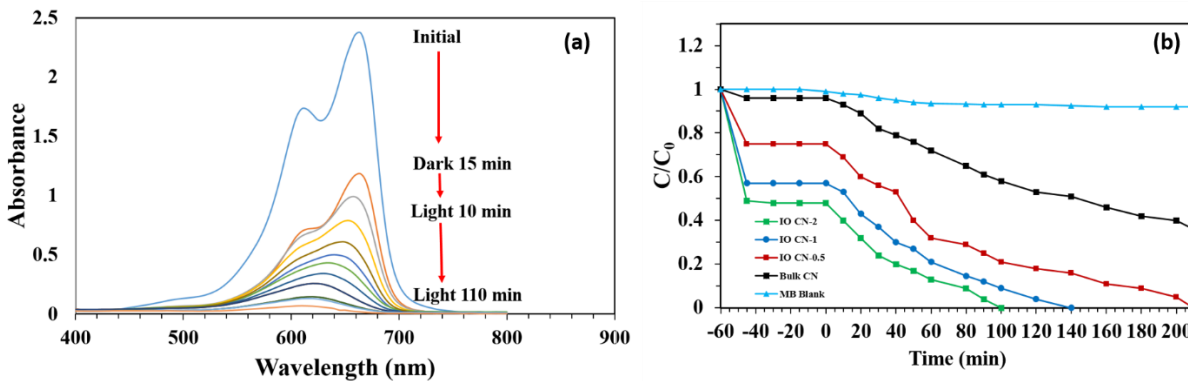


**Figure 3-7.** (a) UV–Vis absorbance spectra of MB; (b) Photocatalytic degradation curves of MB

### 3.4.2 Photocatalytic degradation of RhB

The blank experiment (without using the photocatalyst) under visible light irradiation showed trivial degradation for RhB, confirming that pollutant removal from the solution in the presence of prepared photocatalysts was mainly due to the photocatalytic degradation process. In terms of the adsorption capacity of the samples during the reaction, IO CN3 showed higher adsorption of pollutants compared to other samples.

After an approximately 60 min reaction without irradiation (in the dark condition), the equilibrium of adsorption-desorption was achieved. Thus, further removal of the RhB after the 60 min adsorption experiment was mainly attributed to photocatalytic degradation. As presented in Fig. 25b, the Bulk CN, showed the lowest performance in terms of RhB degradation, and only 40% of the pollutant was removed after 200 min of visible light irradiation. The IO CN1 and IO CN2 showed almost the same photodegradation results, and their ability was improved compared to that

of the Bulk CN. Meanwhile, IO CN3 had the best performance which could completely degrade MB in a 25-min photocatalytic reaction.

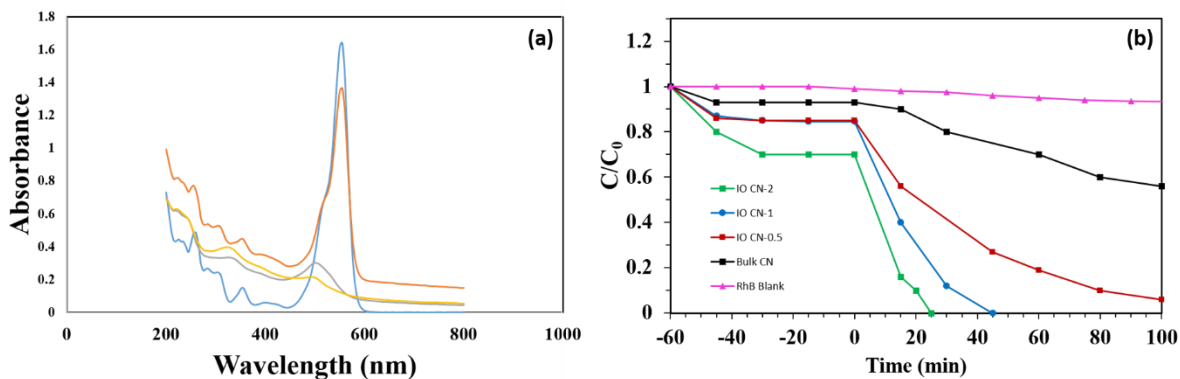


**Figure 3-8.** (a) UV-Vis absorbance spectra of RhB; (b) Photocatalytic degradation curves of RhB

### 3.5 Conclusion

Constructing nanostructure g-C<sub>3</sub>N<sub>4</sub> with well-controlled morphology is accompanied by several advantages in different environmental applications. However, the precise engineering of this catalyst is still a great challenge. In this study, using hard-template approach, we could successfully fabricate hierarchical inverse opal g-C<sub>3</sub>N<sub>4</sub>. As a result of polymerization of cyanamide precursor in the narrow space of SiO<sub>2</sub> microspheres with an average size of 300 nm as the sacrificial hard template, a uniform porous structure was synthesized. The as-obtained IO CN showed superior photoactivity toward degradation of both RhB and MY organic dyes as the target pollutant. Complete degradation of MB was achieved within 110 min, while this time was much more longer for Bulk CN and other reference photocatalysts (more than 300 min). Different characterizations provided the details of enhanced photoactivity of IO CN. Increased surface area, higher porosity,

and the VB position were attributed to the increased efficiency of IO CN toward the degradation of pollutants.

The results of this study is estimated to facilitate the routes of fabricating an efficient g-C<sub>3</sub>N<sub>4</sub> catalyst for wastewater treatment and pollutant degradation.

# **Chapter 4- A New Strategy for Fabrication of Uniform Washer-Ring- like Graphitic Carbon Nitride**

In this chapter, a novel and simple method that utilizes supramolecular self-assembly and hard-template to precisely engineer and control the final nanostructure and morphology of g-C<sub>3</sub>N<sub>4</sub>. The supramolecular precursor, prepared through a hydrothermal process of melamine in water as a solvent, was mixed with SiO<sub>2</sub> microspheres and then after polymerization and template removal, a novel and highly uniform 3D washer-ring-like g-C<sub>3</sub>N<sub>4</sub> (DW CN) was successfully constructed. The uniform and well-separated ring nanostructure, highly available surface area, great porosity, and the introduction of favorable defects into the structure of g-C<sub>3</sub>N<sub>4</sub>, led to higher visible-light absorption and lower photogenerated electron-hole recombination. DW CN showed a much higher photodegradation efficiency of Bisphenol A (BPA), than reference samples. Therefore, this hybrid approach of supramolecular self-assembly and hard-template can be considered as a sustainable way to design the nanostructure of organic photocatalyst (g-C<sub>3</sub>N<sub>4</sub>) to improve the photocatalytic treatment of recalcitrant organic pollutants such as BPA.

## 4.1 Introduction

Bisphenol A (2,2-bis(4-hydroxyphenyl) propane, BPA) is a well-known precursor that is widely used in the fabrication of polymer compounds, including polycarbonates, epoxy resins, etc. [10]. The widespread use of BPA in plastic products and the inappropriate disposal and waste management made this chemical ubiquitous in numerous water systems. As a result, BPA is frequently detected in industrial and municipal wastewater [11]. In addition, BPA has previously been reported to be a typical endocrine disruptor (EDC). Furthermore, even low levels of exposure to this chemical are accompanied by adverse health effects on aquatic wildlife and human beings [12]. Up to now, numerous methods have been applied to remove BPA from contaminated water, such as membrane filtration, chlorination, biological procedures, adsorption, ion exchange [115, 116].

Among the different strategies, semiconductor photocatalysts have great potential to mitigate the ongoing universal environmental challenges through efficient solar energy collection and conversion [117]. Until now, numerous studies have been conducted to design a stable photocatalyst that is active in visible light and has sufficient capacity for different applications of organic pollutant photodegradation and energy production [118-121]. Between the different photocatalysts addressed, graphitic carbon nitride (g-C<sub>3</sub>N<sub>4</sub>), a metal-free organic semiconductor with a layered structure, has drawn tremendous attention from researchers in various applications such as wastewater treatment, CO<sub>2</sub> reduction, H<sub>2</sub> production, and materials synthesis [122-124]. The g-C<sub>3</sub>N<sub>4</sub> photocatalyst benefits from excellent features such as great optical properties, chemical stability, nontoxicity, low price, easy synthesis, and also being active under visible light illumination [125]. It is convenient to construct bulk g-C<sub>3</sub>N<sub>4</sub> through thermal polymerization of N-rich precursors such as melamine and urea. However, pristine g-C<sub>3</sub>N<sub>4</sub> cannot fully meet the

prerequisites for actual applications due to the short survival life of photoinduced charge carriers, small specific surface area, and inadequate solar light absorption [126].

Therefore, various strategies were implemented in different studies to modify the morphological, chemical, electrical, and optical properties of g-C<sub>3</sub>N<sub>4</sub>, such as metal and non-metal doping [127, 128], integrating with other semiconductors to fabricate heterojunctions [129], defect engineering [130, 131], utilizing different synthesis methods such as soft and hard template [123], supramolecular preorganization [132], molten salt [133], nanostructure design [59, 134].

To this end, nanostructure engineering of g-C<sub>3</sub>N<sub>4</sub> has been confirmed to be a unique approach to enhancing photocatalytic activity by improving the separation of photoinduced electron-holes and introducing favorable defects into the heptazine units of this catalyst. The design of nanostructures includes the construction of nanosphere [58], nanotubes [59, 60], nanorods [48, 61], nanosheets [62], nanoclusters [8], and porous hierarchical structure [63]. Up to now, templating and template-free approaches were employed to create nanostructure g-C<sub>3</sub>N<sub>4</sub>. Among different methodologies, the use of supramolecular self-assembly has been regarded as an efficient method to organize the precursor, and subsequently manipulate the final nanostructure of g-C<sub>3</sub>N<sub>4</sub>. To construct and direct ordered morphology, the preorganized supramolecular precursor could be obtained through noncovalent bonding such as hydrogen bonds between the initial building blocks [102, 135]. Morphological manipulation using supramolecular precursors has been performed in various research and studies to form different shapes such as spheres, rods, tubes, and flowers [136, 137]. For example, Huang et al. utilized melamine as a raw precursor and water as a solvent to synthesize a supramolecular structure with prismatic morphology through the hydrothermal procedure and, based on that, fabricated hollow porous prismatic graphitic carbon nitride with superior photocatalytic activity for H<sub>2</sub> production and rhodamine B degradation [138]. However, obtaining

various well-controlled morphologies by simply using supramolecular preorganization depends on the appropriate selection of the solvent [139], and the formation of hydrogen bonds between the monomers would be stronger when the solvent is organic rather than polar. For example, organic solvents such as dimethyl sulfoxide and chloroform could be utilized to dissolve melamine and cyanuric acid at room temperature and fabricate different morphologies. However, the use of these solvents is limited due to their toxicity [140].

Recently, it was well investigated that the template-assisted method is another effective way of forming a g-C<sub>3</sub>N<sub>4</sub> nanostructure because, by controlling the size and shape of the template, the architecture of the as-prepared g-C<sub>3</sub>N<sub>4</sub> nanostructure is directly plausible. For example, Cui et al. produced onion-ring-like g-C<sub>3</sub>N<sub>4</sub> using SiO<sub>2</sub> microspheres as a sacrificial hard-template which exhibited much higher photocatalytic efficiency towards hydrogen evolution, than the bulk sample [78]. In another study, Tian et al. improved the photocatalytic degradation efficiency of the catalyst by producing hierarchical macro-mesoporous g-C<sub>3</sub>N<sub>4</sub> with an inverse opal structure using an ordered silica template [141]. Furthermore, in the previous study by our group, the authors synthesized g-C<sub>3</sub>N<sub>4</sub> nanoclusters using SiO<sub>2</sub> nanoclusters as a hard template and achieved a highly improved photocatalyst for tetracycline degradation [8]. In addition, the use of a hard-template in the synthesis process of g-C<sub>3</sub>N<sub>4</sub> is accompanied by the introduction of some favorable defects in heptazine units due to the confined polymerization of the g-C<sub>3</sub>N<sub>4</sub> planes in the narrow space between hard templates, which makes the hard-templating method more efficient [130].

Inspired by the above research, with the aim of precise g-C<sub>3</sub>N<sub>4</sub> shape and size engineering, in this study, we used a hybrid approach of supramolecular preorganization and hard-templating method. We used water as the solvent to prepare the supramolecular precursor through a simple, reliable, and environmentally friendly approach. After mixing the supramolecular precursor with SiO<sub>2</sub>

microspheres as a hard-template and then removing the template, we thoroughly investigated the morphological, optical, and chemical structure of the as-prepared sample (simplified as DW CN). To analyze the impact of the precursor, we also used melamine and mixed it with SiO<sub>2</sub> microspheres with the same proportion and heating approach as DW CN (named as IO CN). Interestingly, the results showed that for IO CN (that melamine was used as the precursor), the silica particles circumscribe melamine. Then, a hierarchical inverse opal structure was formed after the template was removed, as reported earlier [141]. However, by employing the supramolecular precursor, the supramolecular self-assemblies circumscribe SiO<sub>2</sub> particles. After template removal, highly uniform 3D washer-ring-like g-C<sub>3</sub>N<sub>4</sub> was formed, which had enhanced available specific surface area and porosity, and was decorated with favorable defects in the tri-s-triazine structure. The results of this research confirm that the behavior of the supramolecular precursor in the presence of a hard-template is different compared to that of melamine. Thus, it is believed that the finding of this research could be a starting point for further manipulation of the g-C<sub>3</sub>N<sub>4</sub> nanostructure.

The photoactivity of optimized DW CN and other as-prepared catalysts was assessed toward the degradation of BPA as the target pollutant, under visible light illumination. DW CN exhibited much higher BPA photodegradation efficiency compared to IO CN and other bulk samples, because of its higher surface area, porosity, highly uniform and well-dispersed morphology, and the existence of structural defects in the heptazine units. The degradation pathway and intermediates generated in the BPA photodegradation process were investigated precisely based on the LC-MS analysis. Another important issue in wastewater treatment, specially the photodegradation of organic pollutants, is the toxicity of intermediates produced. The complete degradation of parent pollutants does not testify to the termination of possible biological toxicity



and associated ecological risks [142]. In this study, the possible biological toxicity of the byproducts produced in the photodegradation process of BPA was investigated using three open-source programs based on the quantitative structure-activity relationships (QSAR). Finally, the mineralization capability of DW CN was evaluated using total organic carbon (TOC) concentration. The results of this study could provide comprehensive and worthwhile information on the design of the g-C<sub>3</sub>N<sub>4</sub> nanostructure and its application for effective wastewater remediation.

## **4.2 Experimental section**

### **4.2.1 Preparation of silica microspheres**

Uniformly dispersed silica microspheres with a diameter of around 300 nm were synthesized based on the well-known StÖber method [78]. In detail, solution A contained 154 ml of aqueous ammonia, 304 ml of ethanol, and 370 ml of deionized water mixed in a stirrer for 10 min. Solution B, containing 683 ml of ethanol and 67 ml of tetraethoxysilane (TEOS), was added to solution A in approximately 1 min, while the solution was stirred intensively (800 r/min). After that, the solution was kept under magnetic stirring (400 r/min) for 16 h to allow the growth of silica particles. The white precipitate was then collected by centrifugation (11000 rpm), washed with water and ethanol 3 times, mixed with 100 ml of ethanol, and sonicated for 15 min, then dried in the oven at 100 °C. Finally, the white solid prepared was ground in a mortar and heated in the air from room temperature to 550 °C in 4 h and kept at this temperature for 6 h to achieve monodispersed silica microspheres.

### **4.2.2 Preparation of inverse opal g-C<sub>3</sub>N<sub>4</sub>**

To synthesize the inverse opal g-C<sub>3</sub>N<sub>4</sub> structure, 3 g of silica microspheres were thoroughly mixed with 1.5 g of melamine and transferred to the ceramic-covered crucible. The mixture was then calcined in the air from room temperature to 550 °C for 4 h (with a ramping rate of 2.2 °C.min<sup>-1</sup>).

The resultant yellow sample of the hybrid g-C<sub>3</sub>N<sub>4</sub>/SiO<sub>2</sub> was mixed with 40 ml of 4M ammonium hydrogen difluoride for 48 h to completely remove the hard template of SiO<sub>2</sub>. The suspension was then washed with distilled water several times to the point where the PH reached 7 and then dried in the oven at 80 °C for 24 h. The obtained catalysts were denoted as IO CN. As a control catalyst for this investigation, Bulk g-C<sub>3</sub>N<sub>4</sub> was synthesized by calcining melamine without silica particles in the same heat treatment approach, which was represented by Bulk CN.

#### **4.2.3 Preparation of supramolecular precursor and 3D washer-ring-like g-C<sub>3</sub>N<sub>4</sub>**

To prepare a supramolecular precursor, 4 g of melamine was mixed with 80 ml of deionized water and stirred magnetically while reaching a temperature of 85 °C. The mixture kept stirring at this temperature until dissolved. The mixture was then transferred to a Teflon-lined autoclave reactor and underwent hydrothermal treatment at 180 °C for 24 h. When the suspension reached room temperature, it was washed with ethanol and water several times, and then dried at 60 °C in the oven. Subsequently, 1.5 g of this supramolecular precursor was mixed with 3 g of SiO<sub>2</sub>, grounded, and calcined from room temperature to 550 °C for 4 h (with a ramping rate of 2.2 °C.min<sup>-1</sup>). The synthesized sample then went through the same process as the IO CN (removing silica particles and drying in the oven). Finally, the light yellow sample obtained was labeled DW CN (the reason for this naming is explained in Section 3.3). Again, as a control photocatalyst, the supramolecular precursor without the use of SiO<sub>2</sub> microspheres was calcined in the furnace with a similar heat treatment, labeled SM CN.

#### **4.2.4 Photocatalytic degradation analysis**

Photocatalytic degradation of BPA was performed using different g-C<sub>3</sub>N<sub>4</sub> samples under visible light irradiation of a 300 W xenon lamp with a 400 nm cutoff filter. For each set of photocatalytic experiments, 20 mg of each g-C<sub>3</sub>N<sub>4</sub> photocatalyst was placed in a 50 ml beaker containing 25 ml

of BPA solution ( $15 \text{ mg}\cdot\text{L}^{-1}$ ), and stirred in the dark for 60 min to achieve adsorption-desorption equilibrium. Subsequently, the beaker was placed in front of the visible light irradiation while stirring. For each sample in the photocatalytic process, after a certain photodegradation interval, the solution was removed and centrifuged to store 1 ml of it to evaluate the photocatalytic degradation efficiency. The stability assessment was analyzed as follows: after the photodegradation of BPA, the solution was centrifuged, washed twice, and then collected for the subsequent photodegradation reaction. The scavenging experiment was conducted to assess the main reactive species. Four scavengers of  $\text{AgNO}_3$ , benzoquinone (BQ), isopropyl alcohol (IPA), and triethanolamine (TEA) were used to determine the active species of ( $e^-$ ), ( $\bullet\text{O}_2$ ), ( $\bullet\text{OH}$ ), and ( $h^+$ ).

## **4.3 Results and discussion**

### **4.3.1 Construction mechanism of the inverse opal g- $\text{C}_3\text{N}_4$**

Inverse opal morphology was prepared using melamine as the precursor and  $\text{SiO}_2$  microspheres with an average diameter of 300 nm as the sacrificial hard template. Mixing  $\text{SiO}_2$  microspheres with melamine, followed by calcination and removal of silica particles, resulted in constructing a uniform hierarchical mesoporous structure. In this procedure, melamine polymerizes in the small rooms between silica particles. The silica microspheres circumscribe melamine, and then after the  $\text{SiO}_2$  microspheres are removed by etching, the periodic structure of the IO CN is obtained, due to the reverse replica of the silica microspheres. A schematic illustration of this synthesis process is shown in Figure 4-1. SEM and TEM were employed to explore the microscopic structure of the synthesized materials. The SEM image of  $\text{SiO}_2$  microspheres with an average size of 300 nm is shown in Figure 4-1 a, confirming the fabrication of highly uniform microspheres of the same size. Figure 4-1 b and c represent the SEM images of IO CN, showing the formation of a 3D hierarchical inverse opal structure with abundant mesoporous. For comparison, the morphology of Bulk CN

that was synthesized without using silica particles is shown in Figure 4-1 d which shows highly stacked layers of g-C<sub>3</sub>N<sub>4</sub>. The internal structure and morphology of the IO CN were analyzed using TEM, which is shown in Figures 4-1 e and f, and reveal the existence of plentiful mesoporous in the IO CN with a hierarchical structure.

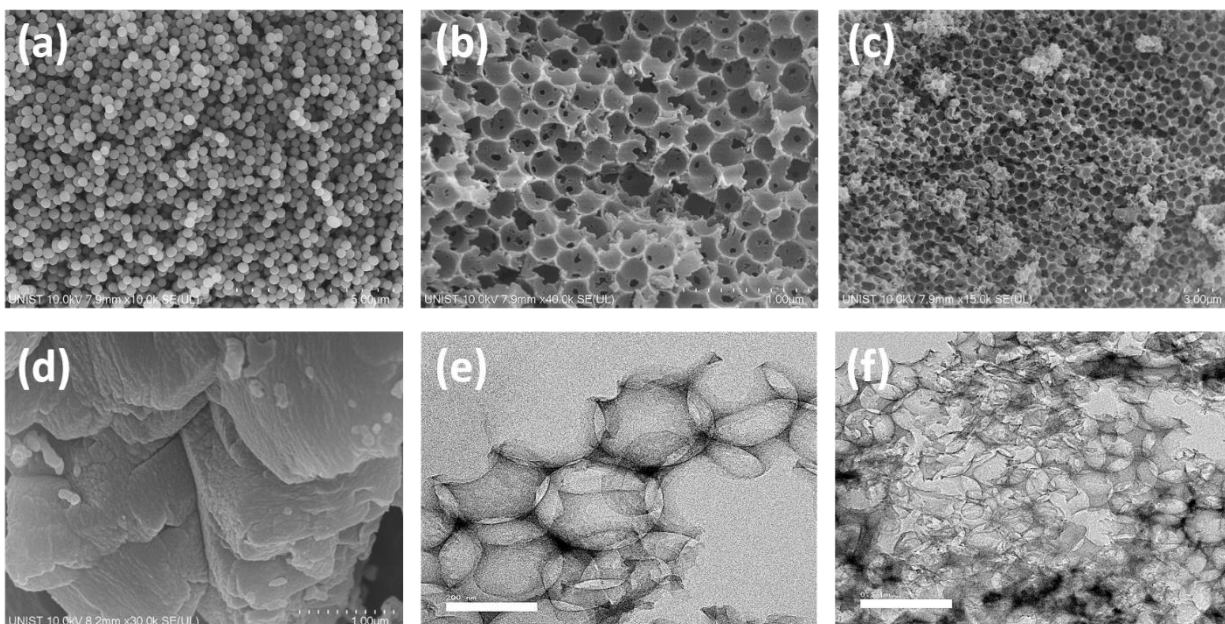


**Figure 4-1.** The SEM images of (a) SiO<sub>2</sub> microspheres with an average size of 300 nm, (b, c) IO CN, (d) Bulk CN; TEM images of (e, f) IO CN

### 4.3.2 Construction mechanism of supramolecular precursor

After the dissolution of melamine in water, the mixture was put under hydrothermal reactions and part of the melamine was hydrolyzed into cyanuric acid at the temperature of 180 °C for 24 h [102]. This reaction goes hand in hand with the release of NH<sub>3</sub> gases, which could be clearly smelled after opening the autoclave cover. During this hydrothermal procedure, unhydrolyzed melamine went through self-assembly reactions with the produced cyanuric acid by making hydrogen bonding, shaping tubular morphology (the schematic representation is shown in Fig.6). As reported,

a melamine molecule can make 3 hydrogen bonds with cyanuric acid molecules, and a cyanuric acid molecule can also generate 3 hydrogen bonds with melamine molecules [59]. As a result of these series of hydrogen bonding and self-assembly, full formation of the tubular supramolecular precursor containing many inner uniform stacking rods was obtained after 24 h hydrothermal reaction [138]. The  $\text{NH}_3$  gas released during the hydrothermal process played an essential role in the fabrication of this supramolecular precursor [138]. It can be observed from the SEM images in Figure 4-2 a that melamine itself does not have any specific morphology; however, when converted to the supramolecular precursor (SM-24), the specific tubular morphology was created (Figure 4-2 b and c).



**Figure 4-2.** SEM images of (a) pure melamine, (b, c) supramolecular precursor after 24 h hydrothermal reaction time

### 4.3.3 XRD and FTIR results of supramolecular structure

Further investigation of the formation of tubular supramolecular precursors from hydrogen bonding between melamine and cyanuric acid was directed using X-ray diffraction (XRD) and Fourier transform infrared (FTIR) spectroscopies. As presented in Figure 4-3, the XRD and FTIR patterns of supramolecular precursors differ from the melamine spectra, confirming the formation of a new molecular arrangement and crystallinity after the hydrothermal reaction. As reported in several studies, the redshift of the  $\text{C}=\text{O}$  characteristic peak and the blue shift of the triazine ring vibration peak indicates the formation of  $\text{N-H}\cdots\text{N}$  and  $\text{N-H}\cdots\text{O}$ , by hydrogen bonds between

melamine and cyanuric acid [143]. These 2 shifts can be observed from the FTIR spectra shown in Figure 4-3 a. The peak of triazine ring vibration was shifted from  $809\text{ cm}^{-1}$  to  $765\text{ cm}^{-1}$ , and the C=O characteristic peak was shifted from  $1648\text{ cm}^{-1}$  to  $1660\text{ cm}^{-1}$  [132]. The new peak at around  $1718\text{ cm}^{-1}$  has emerged in SM-24 FTIR spectra, which corresponds to the existence of the carbonyl group caused by hydrolysis of some melamine [138]. Furthermore, the new characteristic peak of SM-24 located at  $1780\text{ cm}^{-1}$  appeared as a result of the interaction between water and self-assembly supramolecular structure while kept in the hydrothermal process [138]. Moreover, from the XRD spectra of both samples in Figure 4-3 b, it is obvious that for SM-24, some melamine diffraction peaks were weakened or disappeared, and other new diffraction peaks were emerged at around  $10.9$ ,  $11.9$ ,  $21.7$ ,  $28.1$ , and  $33.4^\circ$  [138]. All of the outcomes from XRD and FTIR confirm the creation of a new configuration based on hydrogen bonds and the successful formation of supramolecular structures.

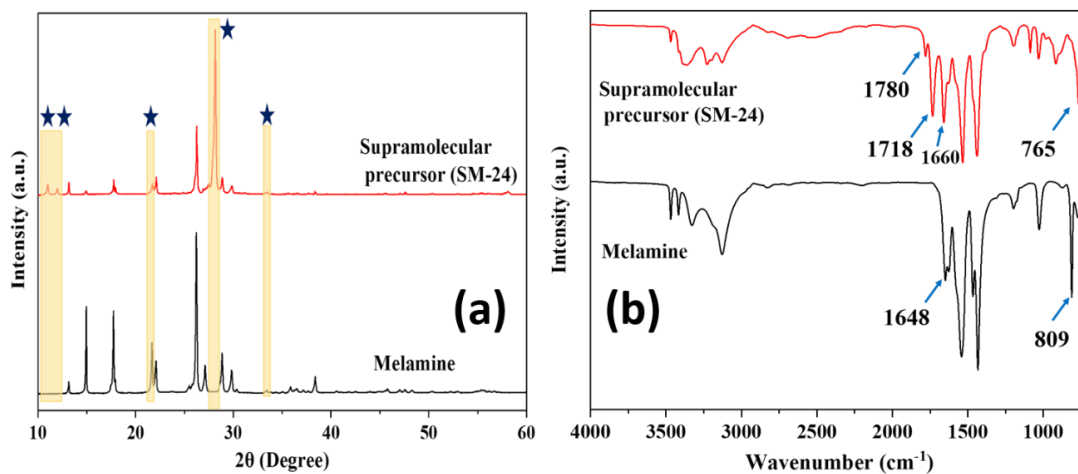


**Figure 4-3.** (a) FTIR spectra of pure melamine and the supramolecular precursor; (b) XRD patterns of pure melamine and supramolecular precursor

#### 4.3.4 Construction of washer-ring-like g-C<sub>3</sub>N<sub>4</sub>

When the supramolecular precursor was subjected to thermal treatment (without using a hard-template), the tubular structure was preserved in some parts of the sample. However, the tubular shape became hollow due to polymerization and calcination. Meanwhile, in some parts, the morphology of small nanotubes was attained (as is presented in Figure 4-4 a and b). However, the polymerization of the supramolecular structure in the presence of SiO<sub>2</sub> microspheres, followed by the removal of silica particles, resulted in the formation of a novel morphology for g-C<sub>3</sub>N<sub>4</sub>. As a result of this synthesis process, the supramolecular precursor circumscribed each silica microsphere individually. After the template was removed, a highly uniform 3D washer-ring-like morphology was fabricated, and the rings were individually or dually separated from other rings. This structure was named DW CN, which is the abbreviation for Dad's washer-like graphitic carbon nitride. The reason for this name is that, while the first author of this study was working on this research, her beloved father passed away, and she was grieving for him. Her father, Hamid, was a plumber, and from her childhood, she always played with the plenty of washers in her father's car. So it is believed that the formation of these washer-like structures belongs to her father because, at first glance that the author saw the SEM images of DW CN, they reminded her father of her. SEM images of this DW CN are presented in Figure 4-4 c, d, e, and f at different magnifications that confirm the formation of a highly uniform ring-like nanostructure. Also, in Fig. S1, the SEM image of DW CN represents the circumscribed rings connected in a half-sphere shape with a radius of 300 nm (equal to the radius of SiO<sub>2</sub> microspheres). This verifies that the supramolecular precursors circumscribed SiO<sub>2</sub> microspheres during polymerization.

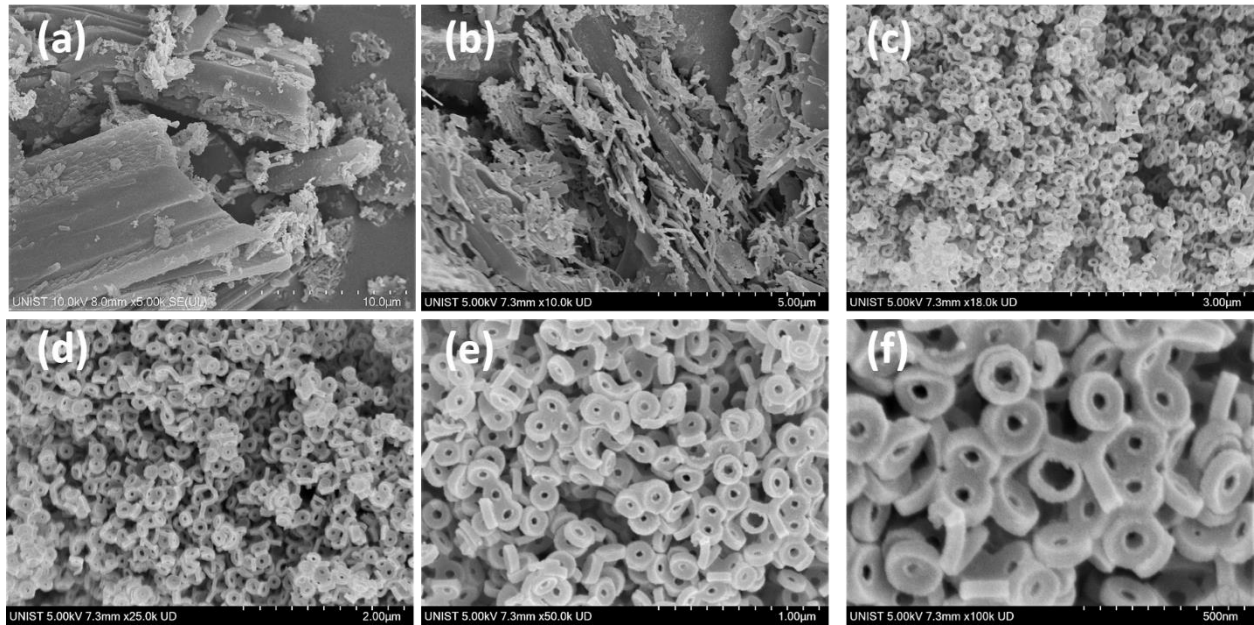


**Figure 4-4.** The SEM images of (a, b) SM CN; (c, d, e, f) DW CN

The TEM images of DW CN are shown in Figure 4-5, which clearly represent the morphology of single ring, double, and triple rings. The rings are thick with an outer diameter of approximately 160 nm, and the diameter of the holes is approximately 35 nm. This washer-ring-like structure is constructed as a collaboration of the supramolecular and hard-template approaches.

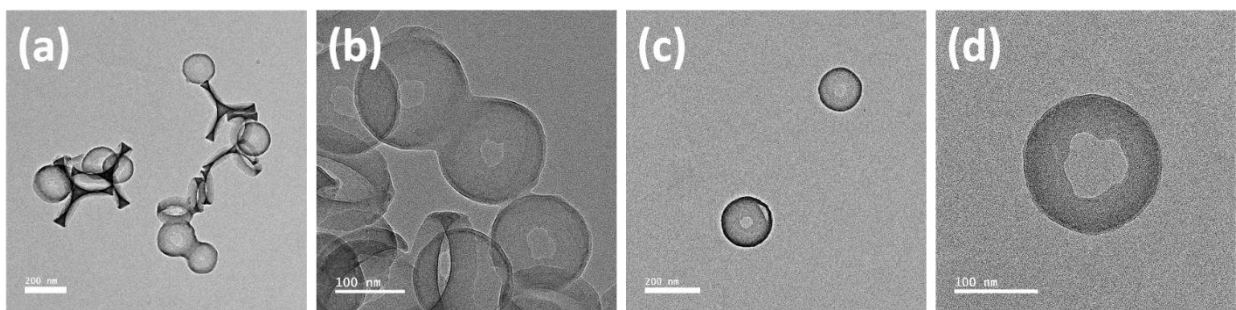


**Figure 4-5.** TEM images of DW CN



Based on the explanations of Sections 4.3.1 to 3.4, the formation process of the as-prepared inverse opal structure (IO CN), supramolecular self-assembly (supramolecular precursor), tubular g-C<sub>3</sub>N<sub>4</sub> (SM CN), and 3D ring-like morphology (DW CN) is suggested and presented in Figure 4-6.

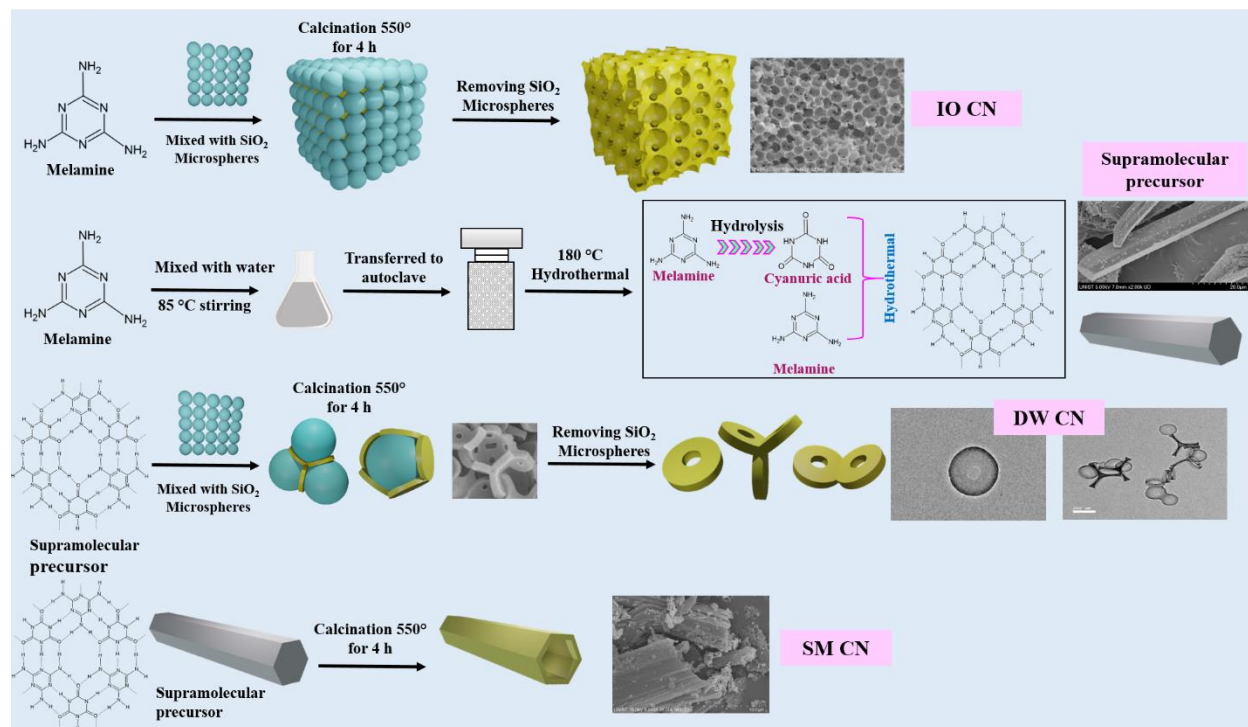


**Figure 4-6.** Schematic representation of the synthesis IO CN, supramolecular precursor, DW CN, and SM CN

### 4.3.5 Specific surface area and porous structure

A more detailed exploration of the surface characteristics and porosity of the samples was carried out using N<sub>2</sub> adsorption-desorption analysis. The results are shown in Figure 4-7 a and show that all 4 catalysts are the typical type of IV curve isotherm with an H3 hysteresis loop at P/P<sub>0</sub> in the range of 0.8-1.0, which confirms the formation of mesoporous structure [144], following SEM and TEM images. From the BJH pore size distribution of all samples presented in Figure 4-7b, it is clear that DW CN shows abundant pores from 2 to 80 nm compared to other catalysts because of the construction of a uniform ring structure. The IO CN also has abundant pores in the 2-80 nm

range due to the formation of the hierarchical porous structure, as observed in SEM images. These data confirm the formation of meso-macroporous in both DW CN and IO CN, while DW CN contains much more abundant porosity.

In the photocatalytic activity process, the specific surface area plays a vital role. A higher surface area results in greater adsorption of pollutants on the surface and more exposed reaction sites for the catalyst [145]. The Brunauer-Emmett-Teller (BET) specific surface area and the corresponding pore diameter and volume of the prepared catalysts are recorded and provided in Table 4-1. For the 4 different catalysts of DW CN, SM CN, IO CN, and Bulk CN, the recorded surface areas are 66.24, 8.7, 50.8, 5.3  $\text{m}^2\text{g}^{-1}$  and their corresponding pore volumes are 0.27, 0.04, 0.19, and 0.03  $\text{cm}^3\text{g}^{-1}$ , respectively. Therefore, the formation of washer-like rings increased the surface area of  $\text{g-C}_3\text{N}_4$ , which is approximately 7.6 times greater than that of SM CN. DW CN also possessed an enhanced pore volume, resulting in higher photocatalytic activity.

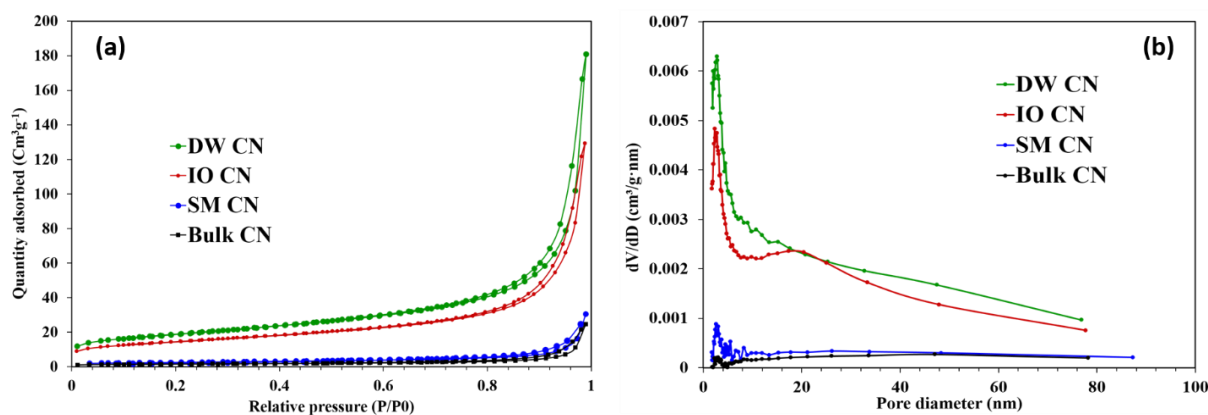


**Figure 4-7.** (a)  $\text{N}_2$  adsorption-desorption isotherms; (c) The correlated pore size distribution plots of as-prepared samples

**Table 4-1** BET results

Sample	Pore volume (cm <sup>3</sup> g <sup>-1</sup> )	Pore diameter (nm)	BET surface area (m <sup>2</sup> g <sup>-1</sup> )
DW CN	0.27	19.8	66.24
SM CN	0.04	28.1	8.7
IO CN	0.19	18	50.8
Bulk CN	0.03	40.8	5.3

#### 4.3.6 Crystal structure and composition analysis

The prepared samples' crystallographic properties and chemical structure were investigated by XRD and FTIR patterns. As shown in Figure 4-8, all samples represent similar patterns that are typical of the graphitic carbon nitride structure. This confirms that the basic structure of g-C<sub>3</sub>N<sub>4</sub> is preserved, despite further post-treatment (using supramolecular precursor and a hard-template). In the XRD spectra, the peak located at  $2\theta=27.3^\circ$  can be indexed as the (002) diffraction peak, corresponding to the inter-planer stacking of carbon nitride aromatic system [146]. The (100) plane centered around  $2\theta=13^\circ$  can be attributed to the in-plane structural ordering of tri-s-triazine units [147]. Compared to other synthesized catalysts, the intensity of both characteristic peaks of DW CN decreased significantly and became broader. This indicates that upon the formation of the ring structure, the crystallization between the basic layers of g-C<sub>3</sub>N<sub>4</sub> and the in-plane structural ordering was reduced.

In the FT-IR spectra of the prepared samples (Figure 4-8b), the peaks at around 808 cm<sup>-1</sup> represent the s-triazine ring [148]. Multiple peaks in the region of 1150-1720 cm<sup>-1</sup> exhibit stretching vibration modes of N=C—N heterocycles. Broad peaks between 3000-3500 cm<sup>-1</sup> correspond to N-H stretching vibrations [102]. In addition to these peaks, a new small peak appeared at 2171 cm<sup>-1</sup> for DW CN, which belongs to the stretching vibration of the terminal cyano groups (C≡N) [149].

It can be speculated that the presence of SiO<sub>2</sub> as a hard-template and incomplete polymerization of g-C<sub>3</sub>N<sub>4</sub> in some parts, resulted in the existence of defects and cyano groups [8]. To provide additional insights on newly produced cyano groups (C≡N), solid-state <sup>13</sup>C NMR analysis was used. As shown in Figure 4-8c, all samples showed 2 clear peaks at 162 and 169 ppm, which correspond to C<sub>3</sub> (CN<sub>3</sub>) and C<sub>2</sub> (CN<sub>2</sub>(NH<sub>2</sub>)) of the heptazine units [150]. Compared to other catalysts, the intensity of peak No. 3 (CN<sub>3</sub>) decreased for DW CN. Furthermore, a clear new peak at 103.4 ppm and a weak peak at 174.5 ppm were detected for the DW CN. The former peak is attributed to the sp hybridized carbon atom in the C≡N groups (C<sub>4</sub>), and the latter corresponds to the carbon atom adjacent to the C≡N groups, respectively [85, 149, 151]. These data further confirm that the core structure of g-C<sub>3</sub>N<sub>4</sub> was preserved during the construction of the 3D ring-like morphology, with a small variation in terminal amine groups upon formation of cyano groups.

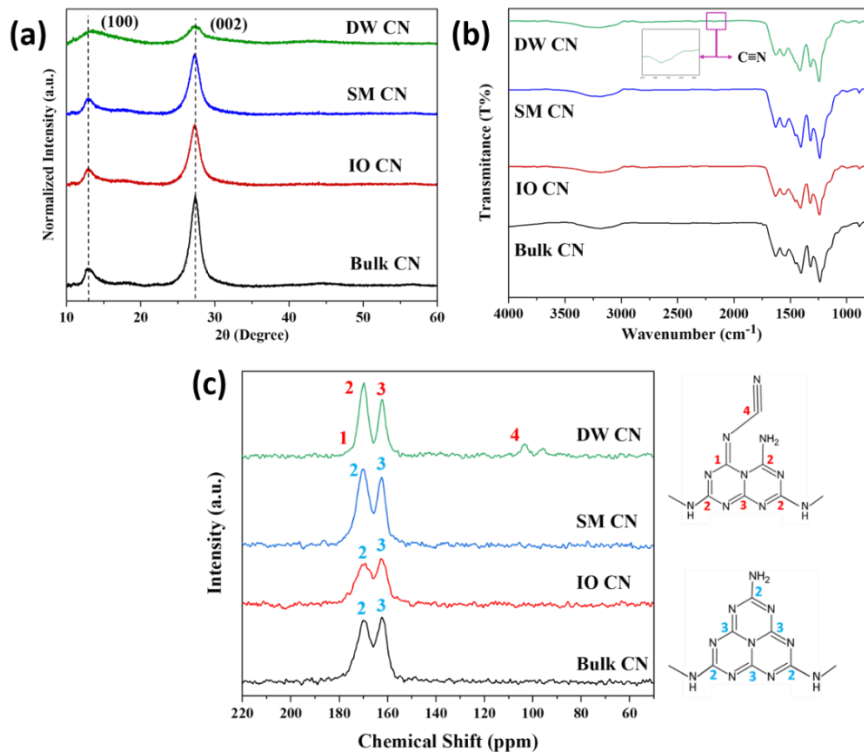


**Figure 4-8.** (a) XRD diffraction patterns, (b) FTIR spectra, (c) NMR spectra of as-prepared catalysts

The chemical composition and binding states of the synthesized photocatalysts were examined using X-ray photoelectron spectroscopy (XPS). Full scan spectra of all samples are shown in Figure 4-9a that confirm the presence of carbon (C1s), nitrogen (N1s), and oxygen (O1s) in the structure of all catalysts, respectively [152]. The high-resolution XPS spectrum for N1s could be deconvoluted to three peaks (Figure 4-9b), in which the  $\text{-C=N-C}$  peak located at around 397.8 eV is related to the  $\text{sp}^2$ -hybridized nitrogen in triazine heterocycle, the peak named  $\text{-N-(C)}_3$  corresponds to the tertiary nitrogen bonded with C atoms. The peak of  $\text{C-NH}_2$  is assigned to the terminal amino functional groups [153]. As exhibited in Fig.9 b, the binding energy of  $\text{-N-(C)}_3$  in the N1s XPS spectra decreased from 399.5 for SM CN to 398.2 eV for DW CN, indicating more electron distributions induced by nitrogen deficiency (the confirmation for the presence of N-vacancies will be discussed later) [76]. The XPS spectrum for C1s for all 4 samples could be deconvoluted into 3 separated peaks as depicted in Figure 4-9c and d. The C-C peak corresponds to the carbon atoms in the graphitic form ( $\text{C-C} / \text{C=C}$ ), which are adventitious carbon contamination, the  $\text{N=C-N}$  peak is assigned to the  $\text{sp}^2$ -bonded carbon in the graphitic carbon nitride framework, and the  $\text{N-C-NH}_2$  peak attributed to the  $\text{sp}^2$  hybridized C at the edge of tri-s-triazine, respectively [154]. Besides, the peak at 285.9 eV attributed to  $\text{C-NH}_x$  bonds can be detected in C1s XPS spectra of DW CN (Figure 4-9d), which also validates the creation of  $\text{C}\equiv\text{N}$  groups, because cyano groups possess identical C1s binding energies as the  $\text{C-NH}_x$  groups [76, 149]. Consequently, all XPS results resemble the typical heptazine-based structure of  $\text{g-C}_3\text{N}_4$ ; however, the peaks located 399 and 400.3 in the high-resolution spectrum of N1s are different for DW CN compared to SM CN, which is attributed to the existence of cyano groups in the structure [155].

According to the deconvolution data of N1s, the peak area ratio of the N=C=N-C to the N-N-(C)<sub>3</sub> (N<sub>2c</sub>/N<sub>3c</sub>) reduced significantly from 3.68 for SM CN to 1.69 for DW CN, as shown in Table 4-2. This decrease in N<sub>2c</sub>/N<sub>3c</sub> indicates the loss of nitrogen atoms in the heptazine structure and denotes the existence of nitrogen-vacancy in the DW CN. Furthermore, this missing of N atoms occurred at -C=N-C lattice sites, rather than -N-(C)<sub>3</sub>, as was reported previously [156].

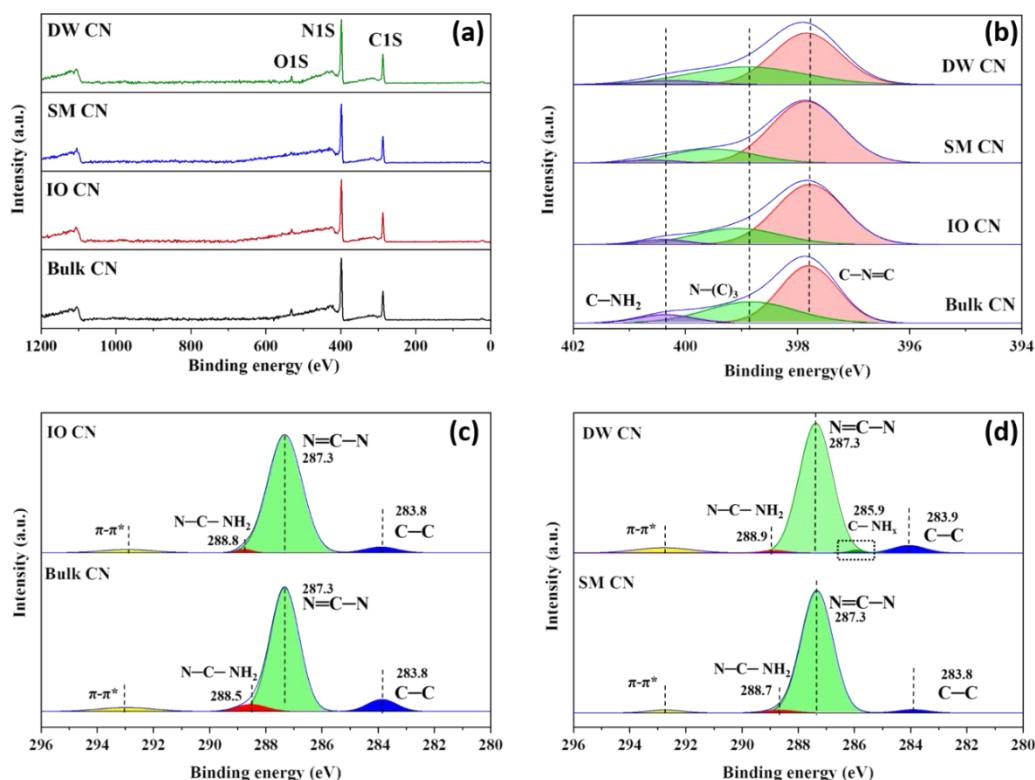


**Figure 4-9.** High resolution XPS spectra of as-prepared catalysts, (a) survey; (b) N1s; (c,d) C1s

**Table 4-2** XPS N1s deconvolution result of SM CN and DW CN.

	SM CN			DW CN		
	N <sub>2c</sub> C=N=C	N <sub>3c</sub> N-(C) <sub>3</sub>	N <sub>CH</sub> C-NH <sub>2</sub>	N <sub>2c</sub> C=N=C	N <sub>3c</sub> N-(C) <sub>3</sub>	N <sub>CH</sub> C-NH <sub>2</sub>
<b>Peak/eV</b>	<b>397.84</b>	<b>399.5</b>	<b>400.6</b>	<b>397.8</b>	<b>398.9</b>	<b>400.2</b>
<b>FWHM</b>	<b>1.25</b>	<b>1.48</b>	<b>0.89</b>	<b>1.21</b>	<b>2.07</b>	<b>1.16</b>
<b>Area</b>	<b>6196.18</b>	<b>1679.31</b>	<b>199.12</b>	<b>4745.8</b>	<b>2796.89</b>	<b>374.6</b>

<b>Peak area ratio (N<sub>2C</sub>/N<sub>3C</sub>)</b>	<b>3.68</b>	<b>1.69</b>
<b>Peak area ratio (N<sub>CH</sub>/N<sub>3C</sub>)</b>	<b>0.12</b>	<b>0.13</b>

**Table 4-3.** XPS N1s deconvolution result of Bulk CN and IO CN.

	Bulk CN			IO CN		
	N <sub>2C</sub> C–N=C	N <sub>3C</sub> N–(C) <sub>3</sub>	N <sub>CH</sub> C–NH <sub>2</sub>	N <sub>2C</sub> C–N=C	N <sub>3C</sub> N–(C) <sub>3</sub>	N <sub>CH</sub> C–NH <sub>2</sub>
<b>Peak/eV</b>	<b>397.79</b>	<b>398.83</b>	<b>400.3</b>	<b>397.7</b>	<b>399.07</b>	400.3
<b>FWHM</b>	<b>1.03</b>	<b>1.58</b>	<b>0.98</b>	<b>1.21</b>	<b>1.53</b>	0.82
<b>Area</b>	<b>4256.69</b>	<b>2412.69</b>	<b>582.52</b>	<b>4978.18</b>	<b>1674.55</b>	277.56
<b>Peak area ratio (N<sub>2C</sub>/N<sub>3C</sub>)</b>	<b>1.76</b>			<b>2.9</b>		
<b>Peak area ratio (N<sub>CH</sub>/N<sub>3C</sub>)</b>	<b>0.24</b>			<b>0.165</b>		

Further confirmation of the presence of nitrogen-vacancy in the structure of DW CN was explored using elemental analysis. As shown in Table 4-4, the N/C atomic ratio of Bulk CN is 1.88, and for the IO CN, a slightly lower, 1.87. However, this reduction in the N/C atomic ratio was enhanced for the DW CN which is 1.83 compared to 1.87 for the SM CN. Several studies have well reported that the use of the hard-template in the g-C<sub>3</sub>N<sub>4</sub> synthesis process and the limitation of the growth of heptazine planes introduces some defects and vacancies, especially nitrogen vacancies [8, 130]. These data following the FT-IR, NMR, and XPS results confirm the formation of defects (cyano groups and nitrogen vacancies) in the structure of DW CN. For more illustration, a schematic atomic representation of the g-C<sub>3</sub>N<sub>4</sub> triazine structure without and with defects is shown in Figure

4-10, which demonstrates the location of the N vacancy and the cyano groups in the g-C<sub>3</sub>N<sub>4</sub> structure.

**Table 4-4** Elemental analysis for Bulk CN, IO CN, SM CN, and DW CN

Sample	C (wt.%)	N (wt.%)	N <sub>total</sub> /C <sub>total</sub> (wt.%)
Bulk CN	34.43	64.95	1.88
IO CN	34.2	64.2	1.87
SM CN	34.2	64.3	1.88
DW CN	33.8	62.12	1.83

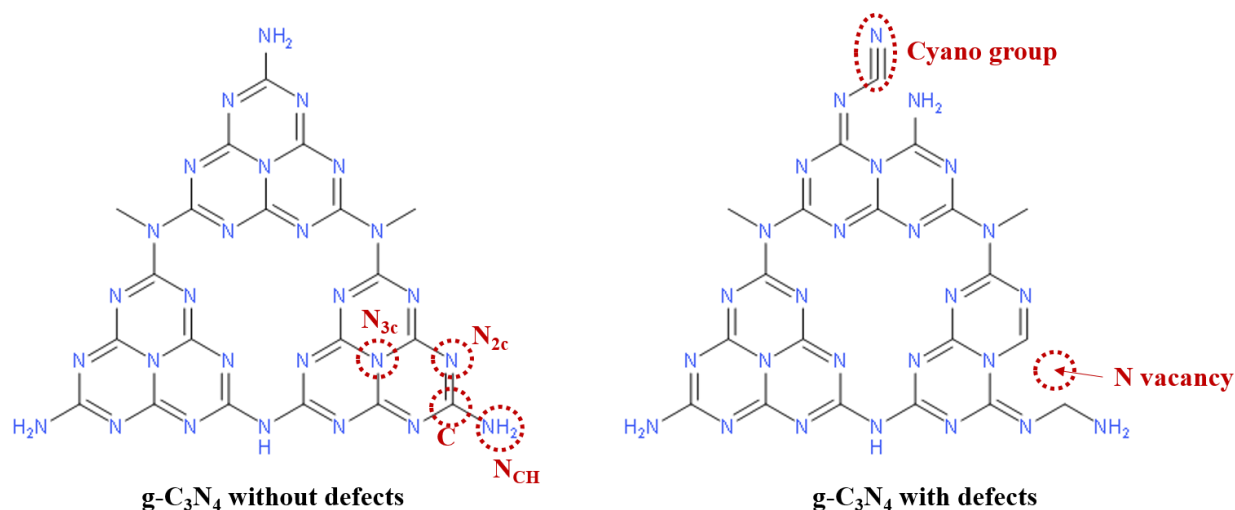


**Figure 4-10.** Schematic atomic model of triazine structure of g-C<sub>3</sub>N<sub>4</sub> with and without defects

### 4.3.7 Optical properties and electronic band structure

In terms of the exploitation of solar energy, it is of great significance to expand light-absorption for the photocatalyst, to produce more photoinduced charge carriers for subsequent redox interactions [86]. Thus, the optical absorption characteristics of photocatalysts were analyzed using UV-vis DRS spectra as presented in Figure 4-11. The absorption edge of all samples is located at 480 and 500 nm, confirming that all as-prepared g-C<sub>3</sub>N<sub>4</sub> photocatalysts are active in the visible light region. Compared to other catalysts, DW CN exhibited a slight blue shift, indicating the



enlargement of the bandgap due to the quantum confinement effect induced by the creation of nanoring morphology [114]. On the contrary, DW CN showed an increased visible light-harvesting capability in the entire visible-light spectrum. This is primarily ascribed to the multiple scattering of the incident light in the pores and rings of DW CN, as well as the highly available surface area of this catalyst [59].

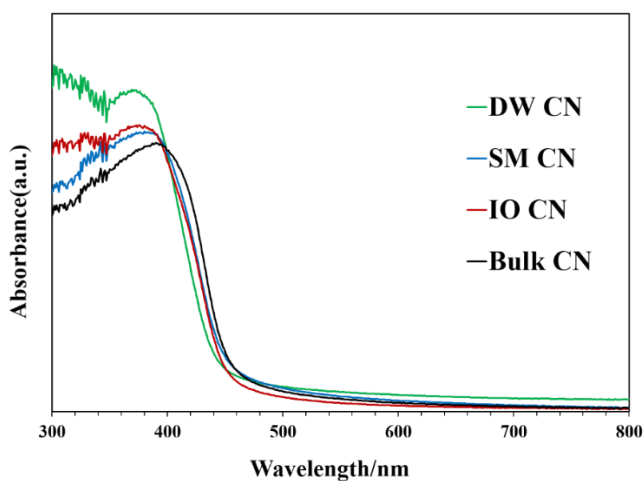


**Figure 4-11.** UV-vis diffuse reflectance pattern of prepared photocatalysts

To obtain the bandgap energies ( $E_g$ ), the plots of  $(\alpha h\nu)^2$  vs photon energy ( $h\nu$ ) were analyzed, based on the Kubelka-Munk functions (Figure 4-12) [157]. The band gaps of the Bulk CN, IO CN, SM CN, and DW CN are 2.75, 2.79, 2.77, and 2.9 eV, respectively. In comparison to the Bulk CN, IO CN had an enlarged bandgap. Compared to SM CN, DW CN had a larger bandgap because of the formation of nanostructures in both IO CN and DW CN, due to the use of the hard-template in the synthesis process. From one perspective, DW CN had the largest bandgap, which is advantageous for photocatalytic degradation, due to the enhanced redox ability of charge carriers [158]. In another view, the bandgap opening has been well reported to limit the use of visible-light by the photocatalyst [159]. However, the DRS spectrum of the catalysts (Figure 4-12) shows an obvious

absorption tail known as the Urbach tail in the visible light range for DW CN, confirming the existence of some electronic states known as midgap states in the band structure of this catalyst [160]. These midgap states that were induced within the bandgap due to the introduction of defects into the DW CN structure can considerably promote the light absorption capability of this photocatalyst, due to the absorption of photons with smaller energies compared to the bandgap energy, a phenomenon called increased sub-bandgap absorption [86, 100, 160, 161]. The transition energy ( $E_t$ ) of the midgap states for the DW CN was predicted to be 2.75 eV, based on the Kubelka-Munk method. This is consistent with previous studies, which suggest that after introducing defects into the backbone of g-C<sub>3</sub>N<sub>4</sub>, some midgap states will be produced at 0.5-1.0 eV below the conduction band minimum [162].

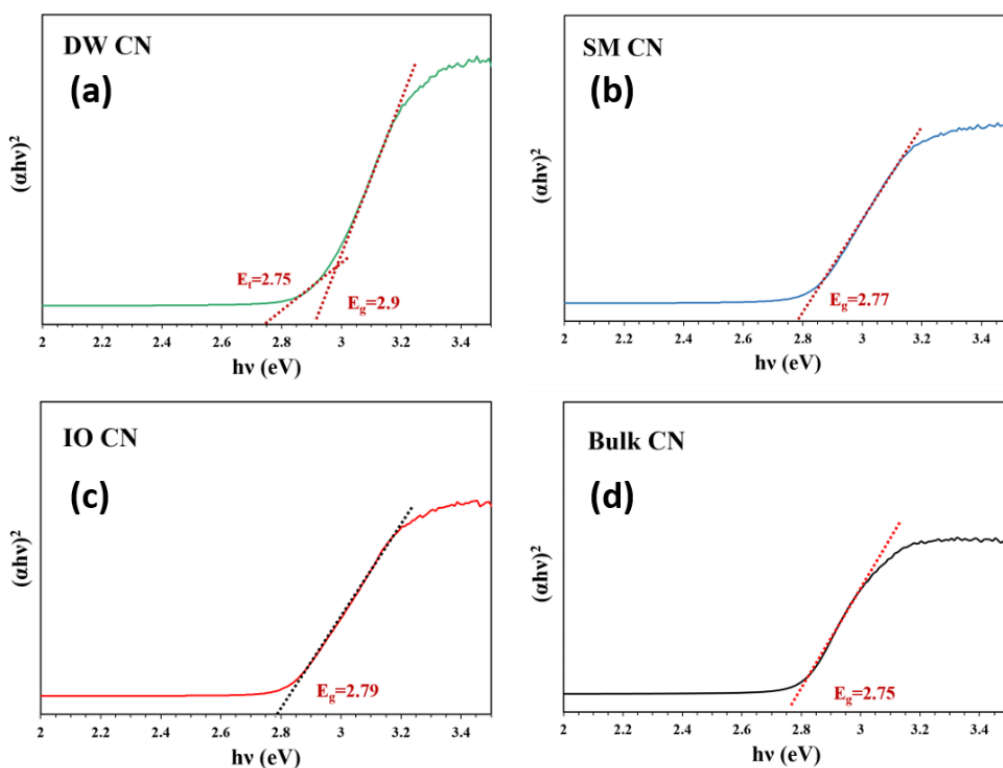


**Figure 4-12.** Optical band gaps of the as-synthesized g-C<sub>3</sub>N<sub>4</sub> catalysts achieved by Tauc plots

Together with the VB position obtained from XPS valence band spectra of catalysts (shown in Figure 4-13), these results could be utilized to determine CB positions and the band edge of mid-gap states. A schematic demonstration representing the electronic band formation of 4 samples is shown in Figure 4-14. It can be observed that the VB position of IO CN (1.3 eV) is slightly more positive than Bulk CN (1.1 eV) and increased to 1.6 eV for SM CN. Meanwhile, the VB position reached its most positive value for DW CN (1.8 eV), which confirms that the combination approach of supramolecular precursor and hard-template could enhance the oxidation capability of the photocatalyst. This feature, along with the presence of midgap states under CB of DW CN plays a considerable role in enhancing the light-harvesting capacity and oxidation capability of this catalyst. These factors are crucial in the photodegradation of BPA as a target pollutant. (As will be discussed in Section 3.7). Furthermore, the mid-gap states could act as temporary trapping sites for photoinduced electrons, thus reducing the possibility of charge recombination [130].

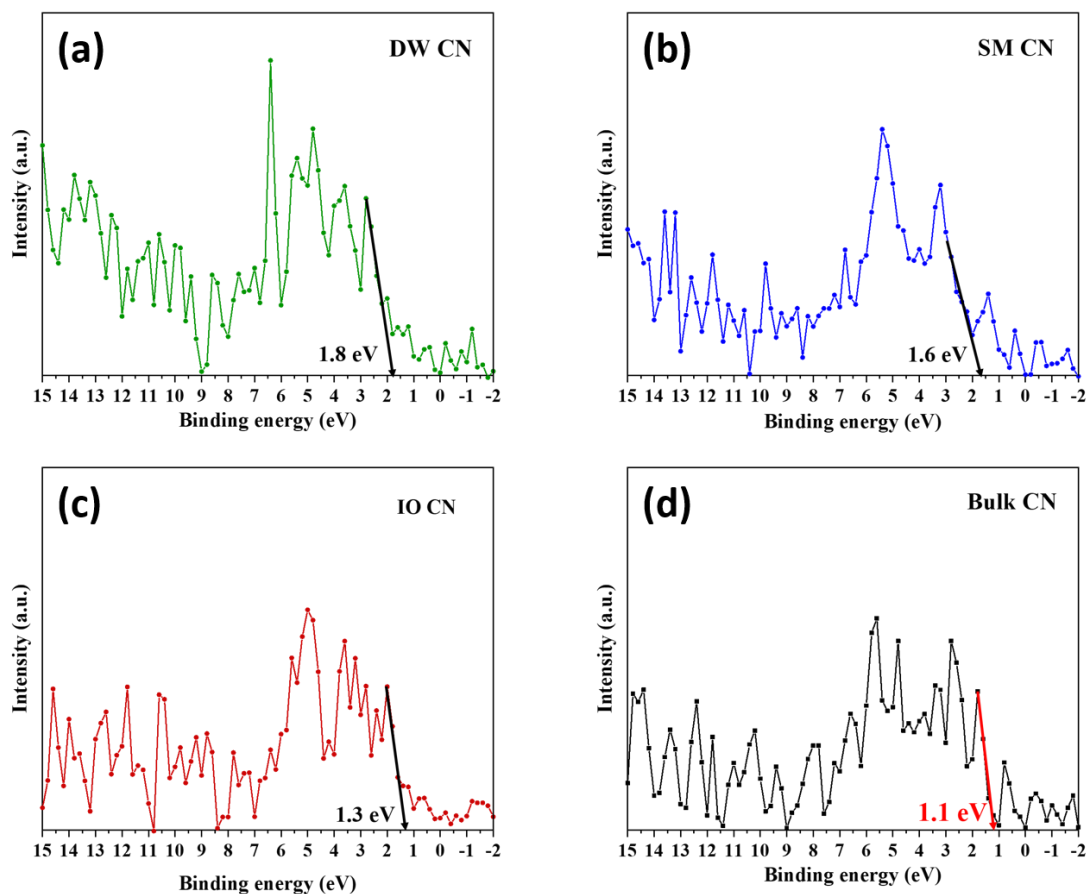


Figure 4-13. XPS valence band spectra of as-prepared catalysts

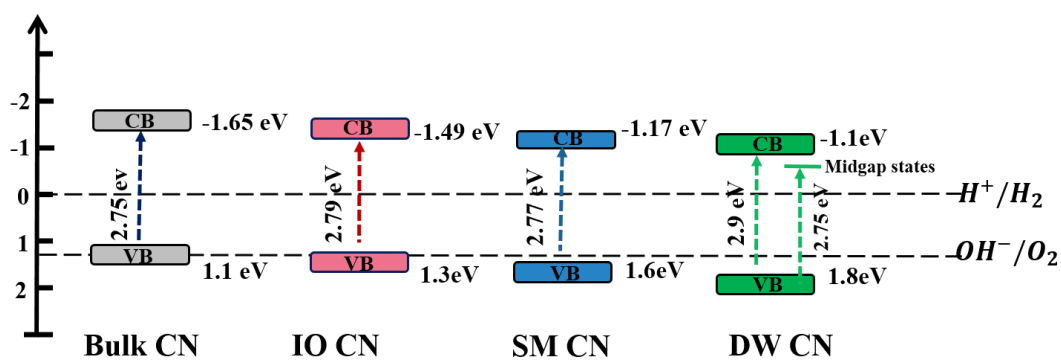
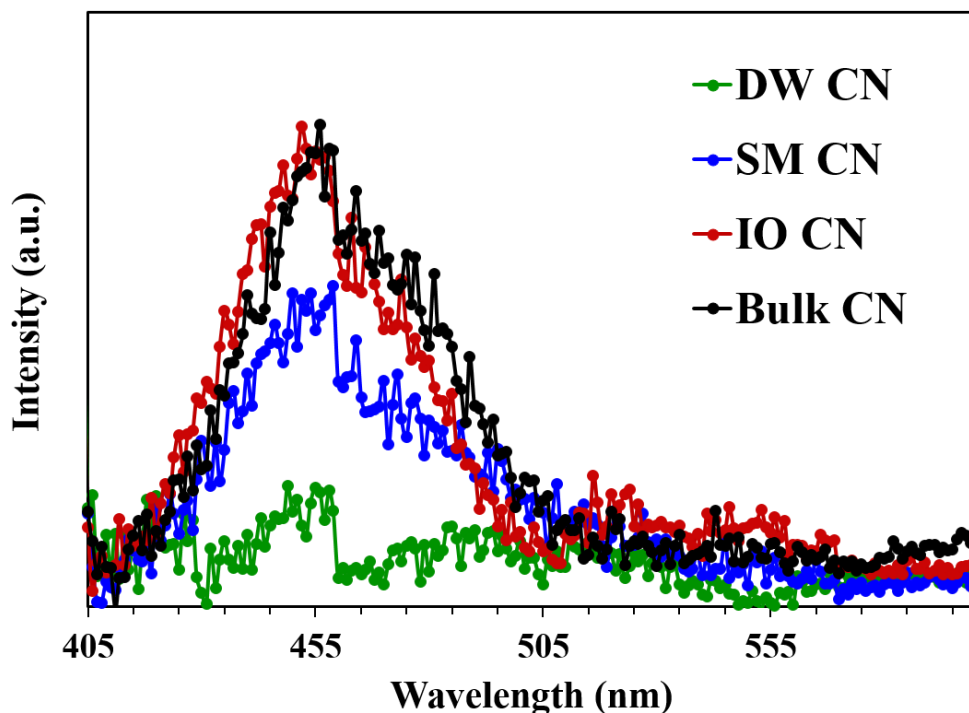


Figure 4-14. Schematic illustration of band edge positions of synthesized catalysts

To elucidate the separation and recombination process of photoinduced carriers, steady-state photoluminescence (PL) spectroscopy was adopted. As depicted in Figure 4-15, Bulk CN showed the strongest PL intensity, hence quick recombination of photoinduced charge carriers. The IO CN also showed moderately lower peak intensity compared to Bulk CN. Among all catalysts, the PL spectrum of DW CN reduced sharply, indicating that this ring-like  $g\text{-C}_3\text{N}_4$  had very low recombination of photogenerated electron-hole. This result indicates that the 3D washer-ring-like nanostructure improved charge separation and transfer because of its high specific surface area, large pore volume, and mid-gap states in the electronic band structure.



**Figure 4-15.** PL spectra of synthesized samples

#### **4.3.8 Photoelectrochemical properties**

Additional investigation on electron-hole separation and transition performance of DW CN and other as-prepared catalysts was conducted by analyzing the photocurrent response of all samples deposited on fluoride-tin oxide (FTO) electrodes. As shown in Figure 4-16, the DW CN showed a

notably enhanced photocurrent under frequent on and off series of light irradiation. The increased photocurrent for DW CN demonstrates that this photocatalyst has enhanced strength in the separation and transition of photogenerated charge carriers. In addition, EIS characterization was performed to further analyze the electron transfer capacity of the prepared samples (Figure 4-16b). It is noted that DW CN showed a much smaller arc diameter in the Nyquist plot, indicating a lower interfacial resistance in charge transfer and a higher electron conductivity [157].

Photoelectrochemical results agree with PL analysis and confirm that DW CN enhanced the separation of photogenerated electron holes, which results in higher redox efficiency and photodegradation capability of the catalyst.

It is worth mentioning that, based on Figure 4-16, both IO CN and SM CN showed enhanced efficiency in electron-hole separation and transition compared to the Bulk sample. However, their optical capability is much lower than that of DW CN, which shows the superiority of the 3D washer-ring-like photocatalyst that was produced by a joint approach of supramolecular self-assembly and hard template.

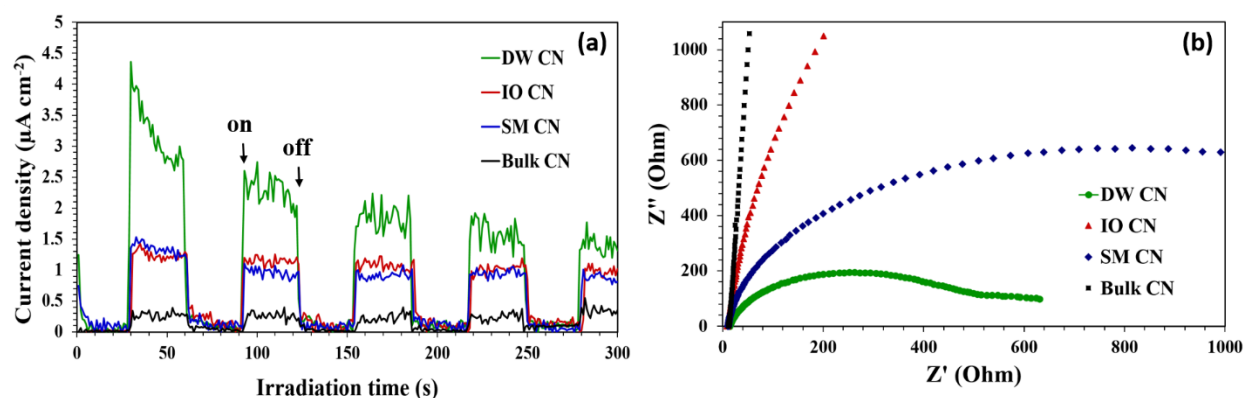


**Figure 4-16.** (a) photocurrent response; (b) EIS Nyquist plots of synthesized samples

#### 4.3.9 Photocatalytic degradation assessment

The photocatalytic performance of synthesized materials was assessed using BPA as the target pollutant. The degradation process was carried out under visible light irradiation and in the presence of each photocatalyst separately (Figure 4-17 a). The blank experiment (without using the photocatalyst) under visible light irradiation showed trivial degradation for the BPA, confirming that BPA removal from the solution in the presence of prepared photocatalysts was mainly due to the photocatalytic degradation process. In terms of the adsorption capacity of the samples during the reaction, DW CN showed higher adsorption of BPA compared to other samples. After an approximately 45 min reaction without irradiation (in the dark condition), the equilibrium of adsorption-desorption was achieved. Thus, further removal of the pollutant after the 60 min adsorption experiment was mainly attributed to photocatalytic degradation. As presented in Figure 4-17 a, the Bulk CN, showed the lowest performance in terms of BPA degradation, and only 18% of the pollutant was removed after 180 min of visible light irradiation. The SM CN and IO CN showed almost the same photodegradation results, and their ability was improved compared to that of the Bulk CN. Meanwhile, DW CN had the best performance which could completely degrade BPA in a 75-min photocatalytic reaction.

The pseudo-first-order kinetic model can be used for this photocatalytic degradation reaction, as presented in Eq. 1 [163].

$$\ln(C_0/C_n) = kt \quad (1)$$

Where  $k$  denotes the first-order reaction rate constant,  $C_0$  and  $C_n$  indicate BPA concentration at reaction times of 0 min and  $n$  min, respectively. As shown in Figure 4-17 b, the value of the photocatalytic reaction rate constant of DW CN ( $0.044 \text{ min}^{-1}$ ) is approximately 12.5 times higher than that of SM CN ( $0.0035 \text{ min}^{-1}$ ) and also much higher than the other 2 samples of IO CN ( $0.0031$

min<sup>-1</sup>) and Bulk CN (0.0015 min<sup>-1</sup>). The results suggested that the photoactivity of DW CN may be considerably enhanced as a result of its greater efficiency of absorbing visible light, which can lead to higher production of photoinduced electrons, causing more efficient separation of charge and thus improved photoactivity. Furthermore, all of the features of DW CN, including a higher specific surface area, ring morphology, and a more positive position of VB, are attributed to its enhanced photoactivity.

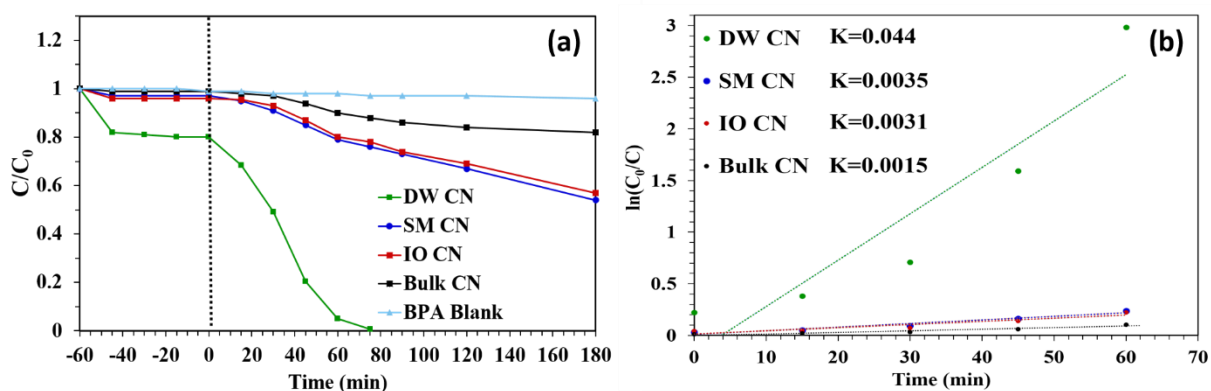


Figure 4-17. (a) Comparison of the photodegradation efficiency of as-prepared photocatalysts toward degradation of BPA; (b) pseudo-first-order kinetic plots of BPA photodegradation for all 4 samples

#### 4.3.10 Stability and recycling analysis

To test the reusability of DW CN, 6 cycles of BPA degradation were implemented under identical conditions. In each cycle, photocatalytic degradation was performed in 60 min under visible light irradiation. As depicted in Figure 5-18, the photodegradation efficiency did not decrease considerably during the first 3 cycles. For the remaining cycles, only a slight variation in the photodegradation capability of DW CN was observed. Furthermore, the SEM image of the used DW CN (Figure 4-19) confirms that the 3D washer-like ring morphology of this catalyst is well



preserved after the sample is re-used, which is advantageous for providing a high active surface area. These results verify that the constructed ring-like DW CN could be utilized as a perfect reusable photocatalyst for the practical application of BPA photocatalytic degradation.

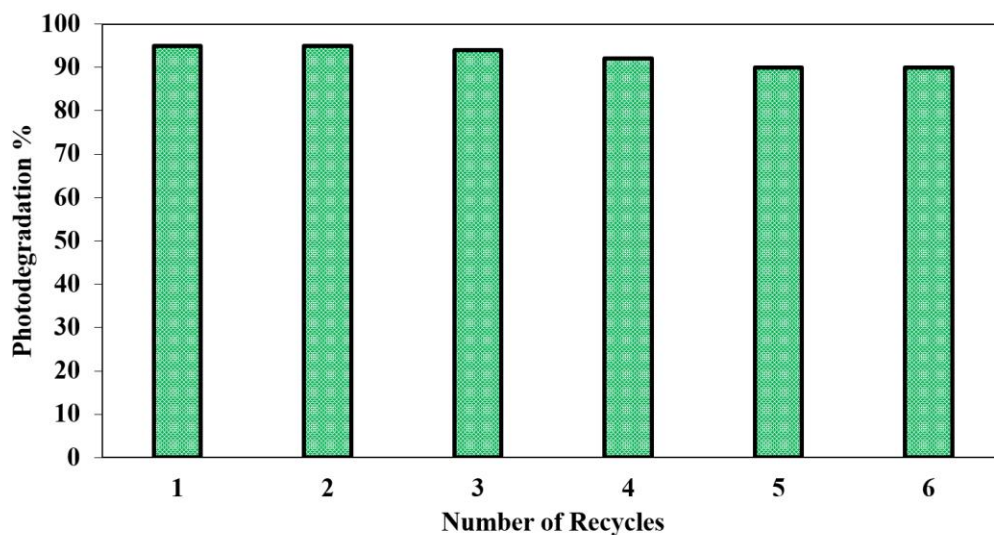


**Figure 4-18.** Photocatalytic stability of DW CN in the degradation of BPA repeated for six cycles

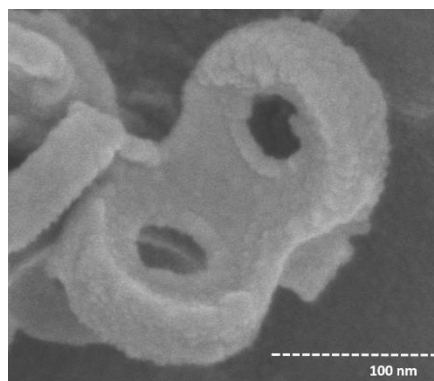


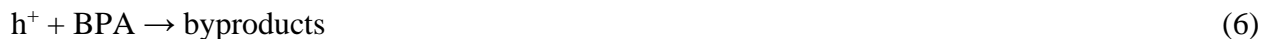
**Figure 4-19.** SEM image of used DW CN

#### **4.3.11 Detection of the main photogenerated reactive species**

As a general rule, 4 reactive species of hydroxyl radicals ( $\cdot\text{OH}$ ), electrons ( $e^-$ ), holes ( $h^+$ ), and superoxide radicals ( $\cdot\text{O}_2$ ) could play essential roles in the photocatalytic degradation of organic pollutants [164]. To identify the dominant photogenerated reactive species involved in the

photodegradation of BPA over DW CN, a series of comparative analyzes was carried out with the specific addition of some scavengers to the beaker containing the catalyst and BPA solution. As presented in Figure 4-20, it was monitored that the addition of AgNO<sub>3</sub> only slightly decreased the photodegradation efficiency of BPA suggesting that electrons (e<sup>-</sup>) did not promote the degradation of BPA. Meanwhile, after the addition of BQ, and IPA, the photodegradation of BPA was significantly inhibited, indicating that 2 reactive species of hydroxyl radicals (•OH), and superoxide radicals (•O<sub>2</sub><sup>-</sup>) played crucial roles in the photocatalytic reaction. However, the greatest quenching impact was detected in the sample constituting TEA, which confirms that holes (h<sup>+</sup>) were the dominant reactive species in the photocatalytic degradation of BPA over DW CN. Based on these results, the contribution of reactive species during BPA photodegradation could be presented in order as follows: •OH < •O<sub>2</sub><sup>-</sup> < h<sup>+</sup>

Accordingly, plausible photocatalytic reactions can be suggested as presented in Eqs. (2) to (7).



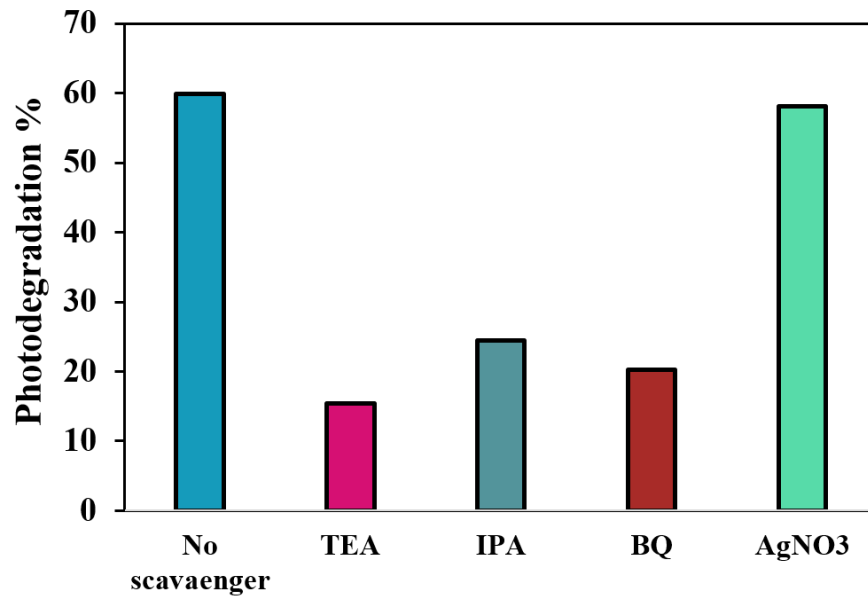


**Figure 4-20.** BPA photodegradation percent utilizing DW CN and in the existence of various scavengers

#### **4.3.12 Unraveling the improved photodegradation of the DW CN photocatalyst**

Based on the above experimental results and interpretation, the molecular procedure for enhanced BPA degradation by DW CN has been suggested. A schematic representation of this is shown in Figure 4-21. It is well accepted that in any photocatalytic process, 3 consecutive main stages are involved: 1) light absorption, 2) charge generation and transportation, and 3) surface oxidation-reduction reactions [165]. The precise engineering of DW CN with its unique microstructure and electronic properties resulted in the superior performance of this catalyst in each step mentioned, toward degradation of BPA. Firstly, the uniform, well-separated washer-like rings of DW CN with highly enhanced porosity had an essential role in the strengthening photodegradation activity of this catalyst by facilitating the transmission of the reagents throughout active sites. Second, the high available surface area of DW CN provides extensive exposed active sites for surface reactions.

In addition, this porous and uniform morphology facilitates light absorption and utilization by providing a more accessible surface area.

Third, the presence of favorable defects in the heptazine structure of DW CN results in the generation of some electronic states inside the bandgap, which affects its photocatalytic performance from 2 aspects. (1) These mid-gap states provide the opportunity for electrons to be excited by the absorption of photons energies lower than those of the bandgap energy and extend the light absorption range. (2) These surface vacancy defects could be regarded as electron trap sites, and significantly prevent electron-hole recombination and promote the movement of photoinduced charge carriers. This is followed by an enhanced reaction of trapped electrons with dissolved oxygen and the production of superoxide radicals ( $\cdot\text{O}_2$ ), which was previously shown to be a strong oxidative agent in the photodegradation process of BPA.

Eventually, the VB position of the DW CN was calculated to be (+1.8 eV), which is much more positive than other as-prepared samples, indicating that the holes in the DW CN have a stronger oxidation potential, which facilitates the degradation of the target pollutant [166]. This follows from quenching experiments that showed that holes played a dominant role in the photodegradation of BPA.

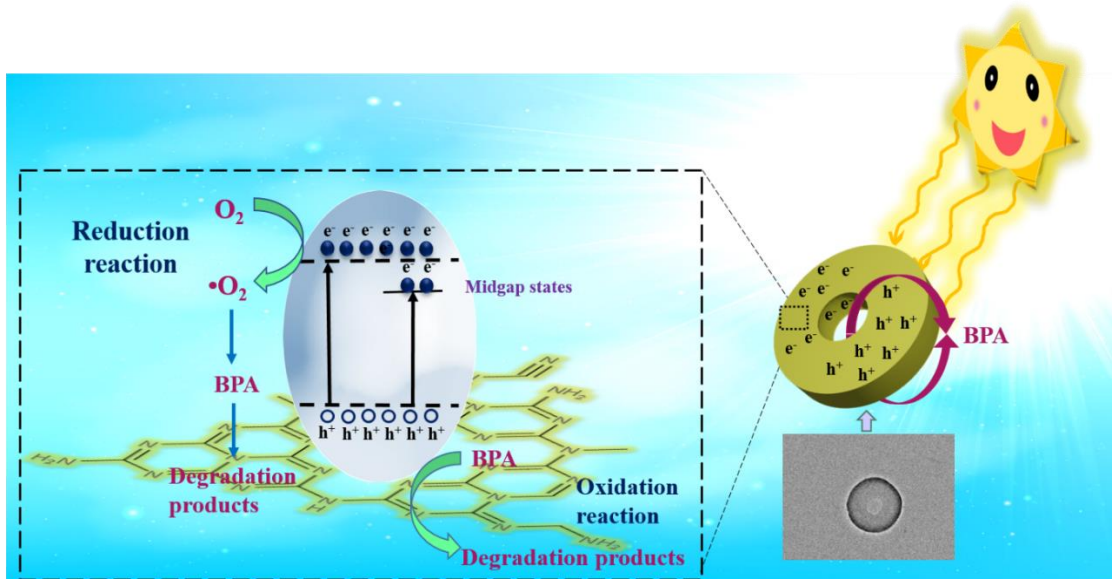


**Figure 4-21.** Schematic representation of BPA photodegradation using 3D ring-like DW CN

#### 4.3.13 Suggested pathway for the transformation of BPA into byproducts

The liquid chromatography-mass (LC-MS) technique was utilized to determine the main intermediates and possible photodegradation routes of BPA at different reaction times using DW CN. Figure 4-22 represents the LC-MS spectra of the initial BPA (before the reaction) and the photodegradation products and intermediates after 15, 30, 45, 60, and 75 min of visible light irradiation ( $\lambda \geq 400\text{nm}$ ). The peak for BPA was detected at 12 min retention time, and the peaks of other major intermediates appeared at retention times of 4.5, 4, 3.3, 3 min. As shown in Figure 4-23, the intensity of BPA (with  $m/z$ : 228) decreased rapidly after 15 min and approximately 95% of BPA degraded after 60 min. Based on these spectra and previous studies, the possible steps and routes of BPA photodegradation are suggested and shown in Figure 4-24. The main byproduct of BPA was P1 ( $m/z$ : 244) which is produced from the hydroxylation process of BPA molecules, similar to reported studies [167]. In this process, hydroxyl radicals attack the aromatic ring of BPA

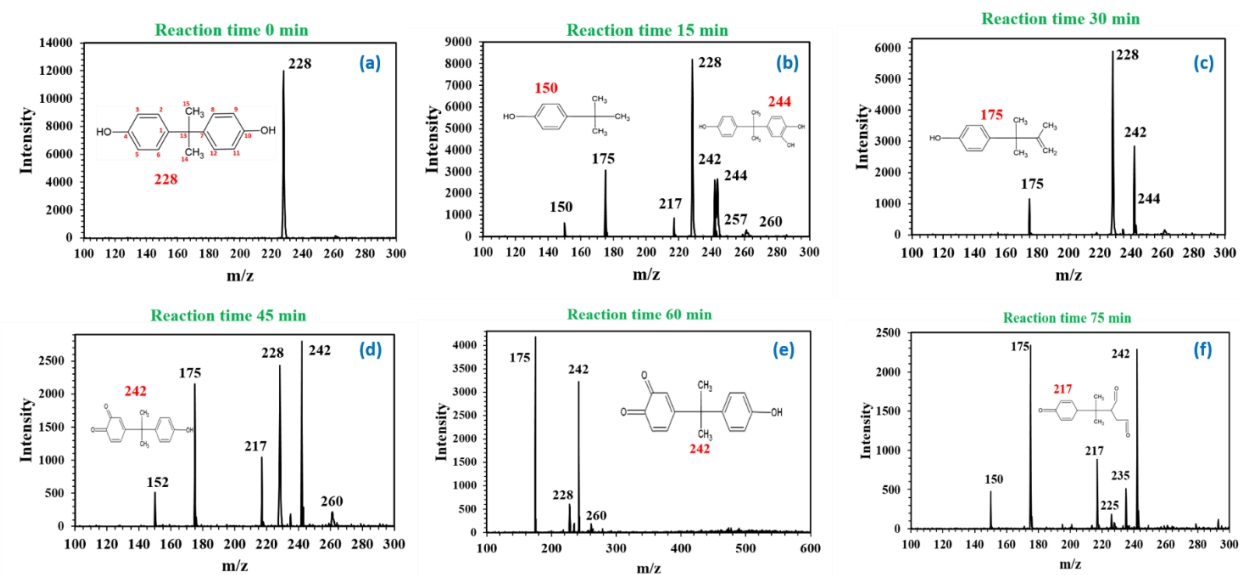
and transform it into P1. After that, there are two major routes for further degradation of the byproducts.

Route 1: Further attack of P1 by hydroxyl radicals resulted in the formation of P2 (m/z: 260) [167]. The intermediates P3 (m/z: 175) and P4 (m/z: 118) were possibly formed due to the oxidation of P2. P5 (m/z: 150) was derived due to the attack of •OH to the electron-rich alkyl carbon of P3 [168]. The subsequent oxidation process gradually converted P5 to P6 [12]. Moreover, an attack on tertiary hydroxyl resulted in the fabrication of P7 (m/z: 133) from P4 [169].

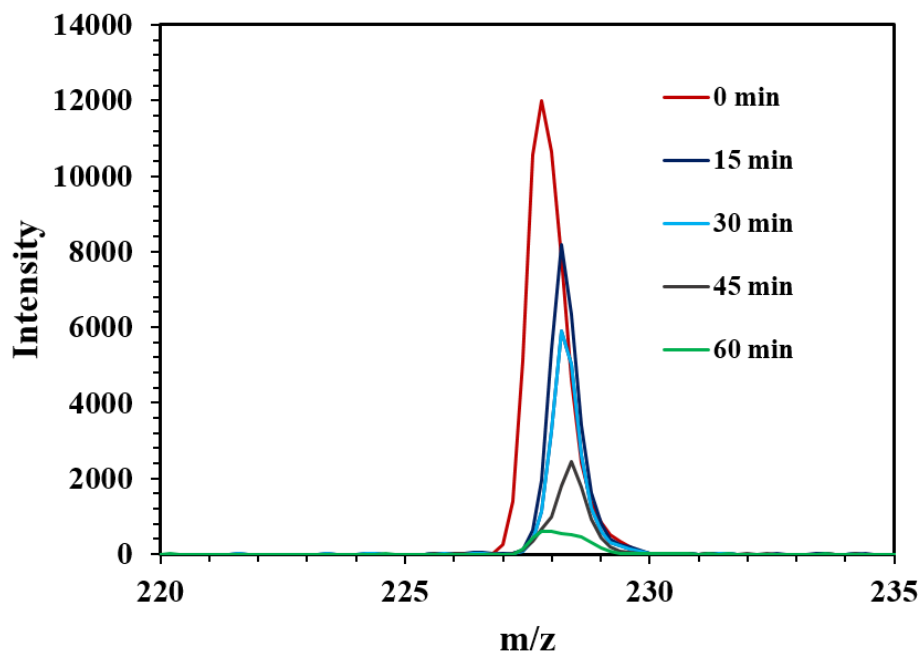
The photodegradation of BPA with route 1 could possibly be expressed in terms of m/z by 2 sub-routes 228→244→260→175→150→152→ or 228→244→260→118→133.

Route 2: This pathway began with the transformation of monohydroxylated BPA (P1) into its quinone derivatives, which is P8 (m/z:242) [169-171]. P8 converted to the di-carbonyl compound of P9 with m/z value of 217 and this byproduct was further transformed to P19 [10].

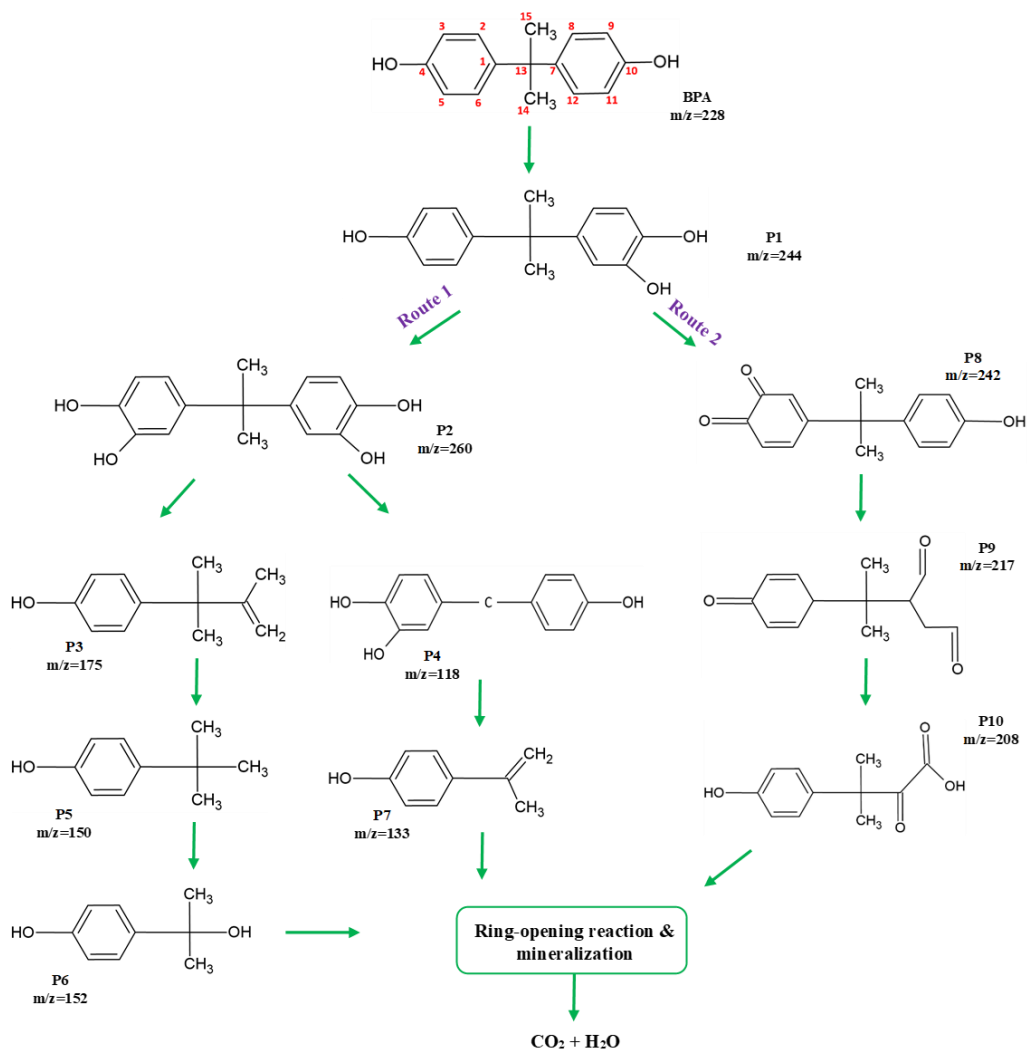
Due to the presence of abundant hydroxyl radicals in the structure, Ring rupturing reactions could occur in P6, P7, and P10 and convert them to nondetectable small byproducts. These small intermediates were ultimately mineralized into carbon dioxide and water. The complete list of produced byproducts, their molecular formula, retention time, proposed structure, and references that were also detected for that specific byproduct are presented in Table 4-5.



**Figure 4-22.** LC-MS chromatograms of (a) BPA; (b) after 15 min; (c) after 30 min; (d) after 45 min; € after 60 min; (d) after 75 min photodegradation reaction time



**Figure 4-23.** Comparison of BPA intensity before the reaction and after 15, 30, 45, and 60 min photocatalytic reaction obtained based on LC-MS chromatograms



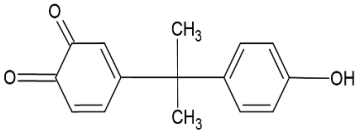
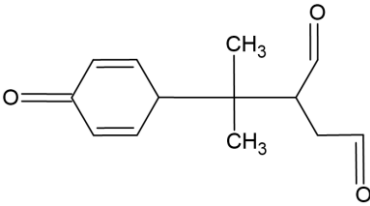
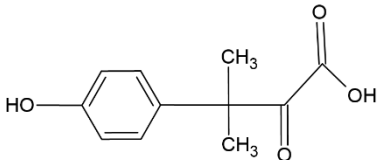
**Figure 4-24.** Proposed BPA photodegradation routes by the DW CN photocatalyst



Table 4-5 Products detected by LC-MS

Product	Molecular formula	m/z	RT (min)	Proposed structure	Detected in reference
BPA	C <sub>15</sub> H <sub>16</sub> O <sub>2</sub>	228	12		
P1	C <sub>15</sub> H <sub>16</sub> O <sub>3</sub>	244	11.6		[170, 172, 173]
P2	C <sub>15</sub> H <sub>16</sub> O <sub>4</sub>	260	12		[167, 169, 174]
P3	C <sub>9</sub> H <sub>16</sub> O	175	3.3		[168]
P4	C <sub>13</sub> H <sub>12</sub> O <sub>3</sub>	118	3.3		[175]
P7	C <sub>9</sub> H <sub>10</sub> O	133	2.9		[169, 176]
P5	C <sub>10</sub> H <sub>14</sub> O	150	3		[12, 177]
P6	C <sub>9</sub> H <sub>12</sub> O <sub>2</sub>	152	3		[12]

---

P8	$C_{15}H_{14}O_3$	242	4.4		[169, 178]
P9	$C_{15}H_{14}O_4$	217	4.4		[11]
P10	$C_{11}H_{12}O_4$	208	2.8		[142]

---

#### 4.3.14 Toxicity evaluation and TOC removal analysis

As explained in the previous section, the photocatalytic degradation of BPA is accompanied by the production of many intermediates, and the estimation of the toxicity of these degradation products is of great importance. However, experimental toxicity prediction is highly challenging because most of the intermediates produced are not available in the laboratory, and the experiments are also costly and time-consuming. Thus, to assess the possible environmental effect and hazard designation of BPA and the intermediates produced during photocatalytic degradation using DW CN, QSAR analysis was implemented, using 3 open-source available software of ECOSAR, TEST, and ERRBA-IRFMN [142]. QSAR analysis anticipates correlated toxicity data based on the quantitative correlation between chemical structure and toxicological activity [179]. A schematic illustration of the acute and chronic toxicities of BPA and intermediates is presented in Figure 4-25, and the corresponding data are shown in Tables S6 and S7. Similar to earlier research, the acute toxic range of BPA and degradation products were estimated, i.e., “very toxic” (<0.1 ppm), “toxic” (0.1-1 ppm), “harmful” (1-10 ppm), and “not harmful” (>10 ppm); and the chronic toxic

ranges were sorted as, i.e., “very toxic” (<1 ppm), “toxic” (1-10 ppm), “harmful” (10-100 ppm), and “not harmful” (>100 ppm) [180]. These data are based on EU Directive No.67/548/EEC, and Chinese Hazard Chemical Evaluation Guidelines (HJ/T 1954-2004), which described various toxicity ranges for BPA and produced intermediates [181, 182]. From Figure 4-25, BPA and its products showed different toxicity levels for 3 organisms of fish, daphnid, and green algae, obtained from the ECOSAR program. For the 10 identified oxidation products, the acute toxicity of P3, P5, P7, and P8 was in the levels of “toxic” and “very toxic”, which are higher than the parent chemical (BPA), demonstrating the production of some byproducts with higher biological toxicity than BPA. One possible reason for the increased toxicity might be the increase in hydroxyl groups in benzene rings, resulting in enhanced binding activity and solubility of produced intermediates and hence their bioavailability [142, 183]. However, the acute toxicity of other intermediates (P1, P2, P4, P6, P9, P10) is lower than that of BPA, and even some byproducts are at the nonharmful level, so they are considered as desired byproducts. Chronic toxicity to fish, daphnids, and green algae are similar to their acute toxicity, as shown in Figure 4-25.

The estimation of developmental toxicity, bioaccumulation factor, and mutagenicity was conducted using the T.E.S.T program. The estrogenic activity was evaluated using the estrogen receptor relative binding affinity (ERRBA) model (IRFMN), as shown in Table 4-6 and Figure 4-26. Generally, BPA and degradation byproducts are toxic to biological development and estrogen receptor binding active, as previously reported [142]. However, two intermediates of P2 and P7 are in the non-toxic developmental region, and two byproducts of P6 and P9 are inactive to estrogen receptor binding. Moreover, interestingly, the BPA and all intermediates are at the level of negative mutagenicity. Additionally, all bioaccumulation factors of the intermediates are considerably lower than those of the parent compound, BPA, which is highly favorable. Reduced bioaccumulation factor decreases the probability that the intermediates produced reach their effective concentrations within living organisms [142]. Consequently, from the point of view of bioaccumulation, photocatalytic degradation of BPA over DW CN is a practical way to mitigate the toxic effects of BPA on living organisms. Among all intermediates produced, P3 has shown the highest toxicity, especially in analyzing acute and chronic toxicity, which is denoted as an undesired byproduct. On the contrary, P9 and P10 had lower toxicity in most QSAR methods, which could be considered favorable byproducts of the photocatalytic degradation of BPA.

Consequently, as stated above, the photodegradation of BPA over DW CN is accompanied by the production of toxic and non-harmful byproducts similar to previously reported research [142, 181]. However, most of the intermediates had reduced overall toxicity compared to that of BPA itself, demonstrating the effectiveness of DW CN in mitigating the toxicity of BPA and its possible environmental impacts.

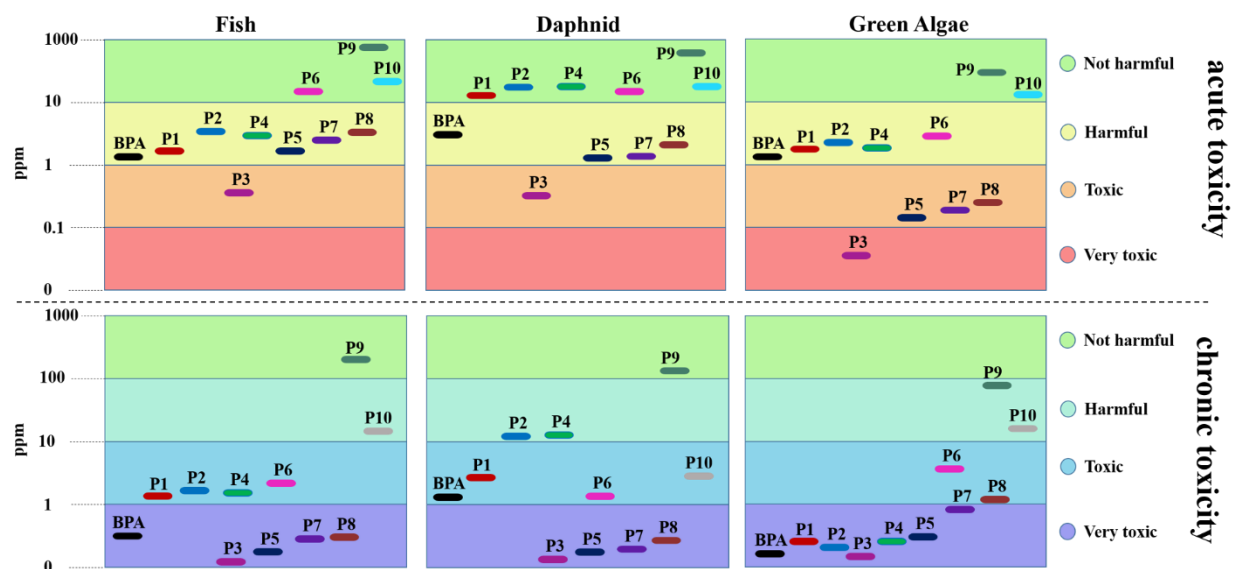


Figure 4-25. The predicted toxicity measurements of BPA and its photodegradation intermediates using ECOSAR

Table 4-6 Acute toxicity obtained using ecological structure activity relationships (ECOSAR) model

Product	Fish 96-h LC50	Daphnid 48-h LC50	Green Algae 96-h EC50
BPA	1.28	5.24	1.33
P1	2.65	13.1	2.07
P2	5.47	32.7	3.21
P3	0.606	0.750	0.058
P4	5.26	32.8	2.90
P5	2.15	1.77	0.2
P6	48.3	16.4	4.17
P7	3.99	2.67	0.364
P8	4.15	3.25	0.384
P9	937.48	803.59	403.02
P10	174	44.9	14.9

**Table 4-7** Chronic toxicity obtained predicted by ecological structure activity relationships (ECOSAR) model

Product	Fish (ChV)	Daphnid (ChV)	Green Algae (ChV)
BPA	0.55	1.77	0.227
P1	1.22	4.57	0.329
P2	2.71	11.7	0.474
P3	0.076	0.123	0.215
P4	2.65	11.9	0.422
P5	0.247	0.249	0.596
P6	4.53	1.64	7.79
P7	0.435	0.345	0.971
P8	0.470	0.447	1.11
P9	396.37	103.35	92
P10	15.3	4.02	23.7

**Table 4-8** Summary of toxicity assessment indices produced by quantitative structure-activity relationship (QSAR) models

Product	Developmental toxicity	Ames mutagenicity	Bioaccumulation factor	Estrogenic activity
BPA	0.71	0.09	117.27	Active
P1	0.65	0.07	82.39	Active
P2	0.58	0.1	21.05	Active
P3	0.76	0.05	24.68	Active
P4	0.71	0.25	17.42	Active
P5	0.79	0	42.51	Active
P6	0.74	0.15	7.05	Inactive
P7	0.57	0.37	47.57	Active
P8	0.9	0.46	23.34	Active
P9	0.76	0.21	N/A	Inactive
P10	0.8	0.36	1.34	Active

TOC analysis was performed to examine the mineralization capability of the DW CN, as shown in Figure 4-27. After a reaction of 30 min, the TOC concentration was reduced by 25%, and after 60 min, 40% TOC removal was achieved. BPA was completely removed from the solution after 75 min of reaction, during which the TOC elimination efficiency was approximately 45%. Therefore, the photocatalytic degradation reaction should be prolonged to completely mineralize the solution and convert all intermediates to H<sub>2</sub>O and CO<sub>2</sub>.

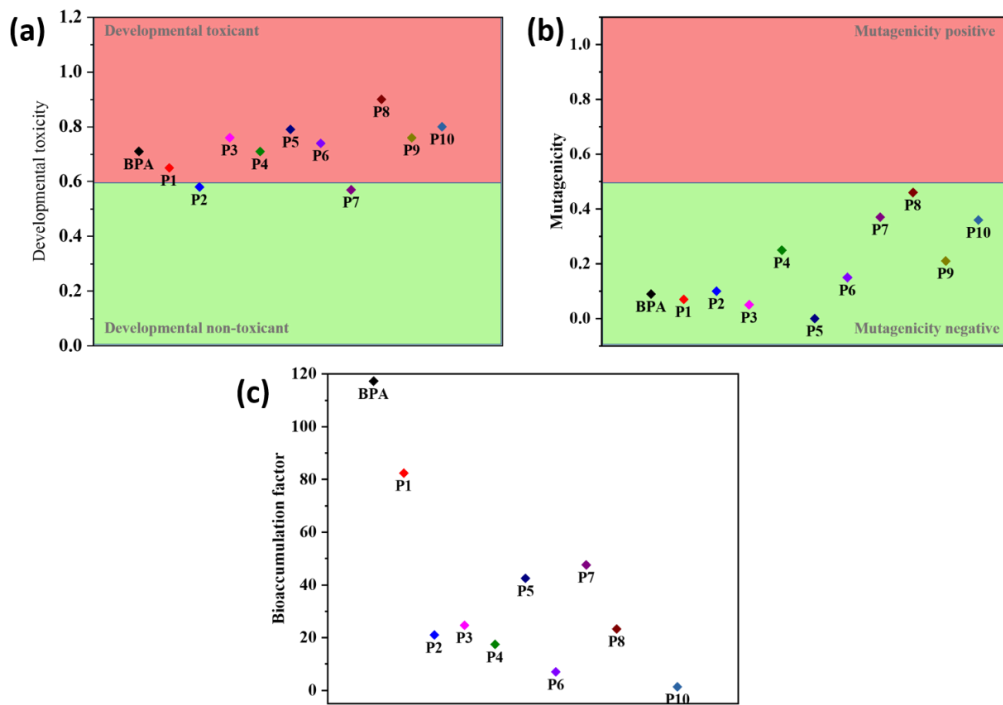


**Figure 4-26.** Toxicity analysis results (a) developmental toxicity; (b) mutagenicity; (c) bioaccumulation factor of BPA and produced intermediates

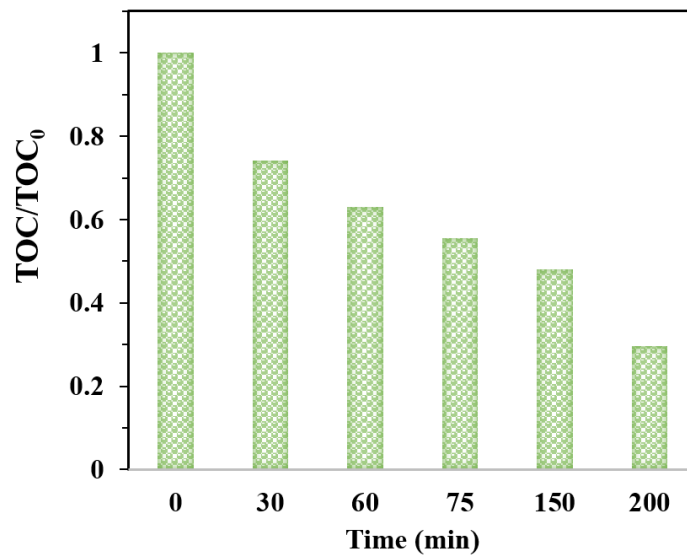


**Figure 4-27.** Removal of TOC as a function of time for BPA degradation using DW CN

#### 4.4 Conclusions

The precise engineering of the g-C<sub>3</sub>N<sub>4</sub> catalyst remains a great challenge. In this study, using the joint approach of supramolecular self-assembly and hard-template, a highly uniform and dispersed 3D ring-like morphology for g-C<sub>3</sub>N<sub>4</sub> was successfully fabricated. The supramolecular preorganization with a tubular shape was synthesized using water as the solvent and melamine as the monomer, through a hydrothermal reaction and hydrogen bonding. After mixing with SiO<sub>2</sub> microspheres, supramolecular self-assembly circumscribed SiO<sub>2</sub> particles and novel uniform dispersed washer-ring-like morphology were obtained, with an average outer diameter of 180 nm, and the diameter of holes inside the ring was approximately 35 nm.

The as-obtained DW CN with ring-like nanostructure showed superior photoactivity toward degradation of BPA as the target organic pollutant. Moreover, complete degradation of BPA was achieved within 75 min, while this time was much longer for IO CN and other reference photocatalysts (more than 300 min).

The increased surface area, higher porosity, existence of defects, and VB position were attributed to the increased efficiency of DW CN toward the degradation of BPA by enhancing active sites, increasing visible-light absorption capability, formation of midgap states, and inhibition of photogenerated electron-hole recombination.

The recyclability of DW CN was analyzed after the catalyst was used for 6 consecutive BPA photodegradation reactions. The photoactivity of DW CN did not significantly reduce, and even the ring-like morphology was preserved after the photodegradation reaction. Furthermore, based on the results of the risk assessment, some byproducts had much lower toxicity than BPA.

Ultimately, this comprehensive study on the fabrication of 3D ring-shaped g-C<sub>3</sub>N<sub>4</sub> using a simple and joint approach of supramolecular self-assembly and hard-template is expected to be a promising pathway to manipulate nanostructure and morphology and obtain highly efficient photocatalyst.

# Chapter 5- Conclusion

In summary, this thesis mainly focused on the synthesis of graphitic carbon nitride photocatalyst through three separate processes based on hard-template approach. In the first part by using SiO<sub>2</sub> clusters as a template, mesoporous graphitic carbon nitride nano-clusters (NC MCN) were fabricated as a high-activity photocatalyst. The confined growth of carbon nitride in the presence of SiO<sub>2</sub> clusters introduced extra structural defects to the carbon nitride framework including nitrogen vacancies and cyano groups, which was confirmed by employing different characterization analyses. These structural defects created midgap states below the conduction band, which improved light-harvesting efficiency and suppressed electron-hole recombination. Thus, NC MCN showed high photocatalytic activity toward degradation of both tetracycline and rhodamine B under visible light irradiation. Complete degradation of 15 ml solution of 15 ppm tetracycline was achieved in 30 min compared to the bulk catalyst (taking more than 3 h). Furthermore, NC MCN demonstrated high stability after reusing for 8 consecutive photodegradation cycles. The total organic carbon concentration at different reaction time showed a rising and falling trend, which illustrate photodegradation process, i.e. adsorption, photodegradation, and mineralization. By liquid chromatography-mass spectroscopy analysis, the produced intermediates during the tetracycline degradation were proposed, which showed the



formation of smaller molecules in just 15 min. The toxicity of the intermediates was analyzed using quantitative structure-activity relationship estimation and the outcomes exhibited that the toxicity of the solution reduced as the reaction time increased. This comprehensive study from photodegradation process to mineralization of TC demonstrated NC MCN as a promising photocatalyst for sustainable treatment of wastewater.

In the second part of the project, by using silica microspheres as the hard-template we could successfully fabricate hierarchical inverse opal g-C<sub>3</sub>N<sub>4</sub>. As a result of polymerization of cyanamide precursor in the narrow space of SiO<sub>2</sub> microspheres with an average size of 300 nm as the sacrificial hard template, a uniform porous structure was synthesized. The as-obtained IO CN showed superior photoactivity toward degradation of both RhB and MY organic dyes as the target pollutant. Complete degradation of MB was achieved within 110 min, while this time was much more longer for Bulk CN and other reference photocatalysts (more than 300 min). Different characterizations provided the details of enhanced photoactivity of IO CN. Increased surface area, higher porosity, and the VB position were attributed to the increased efficiency of IO CN toward the degradation of pollutants.

Finally, in the third part of the project, using the joint approach of supramolecular self-assembly and hard template, we could successfully fabricate highly uniform and dispersed ring-like morphology for g-C<sub>3</sub>N<sub>4</sub>. In detail, the reaction behavior of melamine and supramolecular self-assembly was thoroughly investigated in the presence and without using SiO<sub>2</sub> microspheres. The supramolecular preorganization with a tubular shape was synthesized using water as the solvent and melamine as the monomer, through hydrothermal reaction and hydrogen bonding. The fabrication of supramolecular self-assembly was confirmed using XRD and FTIR analysis. When the supramolecular precursor went through calcination (without using the hard template), a hollow

tubular structure was attained, as was reported previously. Our purpose for this study was to scrutinize the polymerization of supramolecular precursors in the narrow space of SiO<sub>2</sub> microspheres with an average size of 300 nm as the sacrificial hard template. It was observed that when melamine was used, the hard template would circumscribe the melamine particles, and after calcination and removal of the template, hierarchical inverse opal structure could be achieved, through the reverse replica of silica particles. On the contrary, when the supramolecular precursor was utilized and mixed with the SiO<sub>2</sub> microspheres (with the same synthesis procedure as IO CN), the supramolecular precursor would circumscribe SiO<sub>2</sub> microspheres, and after removal of the template, a novel highly uniform and dispersed washer-ring-like morphology was obtained, with average outer diameter of 180 nm, and the diameter of holes inside the ring was approximately 35 nm. The as-obtained DW CN with ring-like nanostructure showed superior photoactivity toward degradation of BPA as the target organic pollutant. Complete degradation of BPA was achieved within 75 min, while this time was much more longer for IO CN and other reference photocatalysts (more than 300 min). Different characterizations provided the details of enhanced photoactivity of DW CN. Increased surface area, higher porosity, the existence of defects, and the VB position were attributed to the increased efficiency of DW CN toward the degradation of BPA. These features result in enhanced active sites, visible-light absorption capability, formation of midgap states, and inhibition of photogenerated electron-hole recombination in DW CN.

The recyclability of DW CN was analyzed after using the catalyst for 6 consecutive BPA photodegradation reactions. The photoactivity of DW CN did not reduce significantly, and even the ring-like morphology was preserved after the photodegradation reaction. The produced byproducts of BPA were estimated based on LC-MS characterization, and photodegradation pathways were suggested. As the toxicity analysis is of crucial importance in wastewater treatment,

the risk assessment was performed using three open-source programs based on QSAR models. It was found that one of the byproducts possessed much lower toxicity compared to the BPA, and other intermediates. Ultimately, the mineralization capability of DW CN in the BPA photodegradation was assessed, which showed that by prolonging the experiment, TOC would be reduced greatly.

Accordingly, this comprehensive study on the fabrication of ring-like g-C<sub>3</sub>N<sub>4</sub> using joint and simple approach of supramolecular self-assembly and hard template is expected to be promising pathway of manipulating g-C<sub>3</sub>N<sub>4</sub> nanostructure, providing a new strategy to control the final morphology. It is believed that by changing the morphology of hard template, further well-controlled shapes of g-C<sub>3</sub>N<sub>4</sub> could be constructed, which needs more research and study. Moreover, the detailed investigation on BPA photodegradation, toxicity assessment, and mineralization was performed. This research is estimated to facilitate the routes of fabricating an efficient g-C<sub>3</sub>N<sub>4</sub> catalyst for wastewater treatment and pollutant degradation.

## 5.1 Suggestions

- The photoactivity of synthesized catalysts could be tested for different applications such as H<sub>2</sub> production, CO<sub>2</sub> reduction.
- Constructing silica nanoparticles in different shapes could result in the fabrication of new morphologies with new characteristics, which could be further investigated.

## Chepter 5- Refernces

- [1] R.P. Schwarzenbach, B.I. Escher, K. Fenner, T.B. Hofstetter, C.A. Johnson, U. Von Gunten, B. Wehrli, *The challenge of micropollutants in aquatic systems*, *Science*, 313 (2006) 1072-1077.
- [2] C. Ortolano, B. Tomasello, N. Grassie, N. Wambiji, M. Antonelli, *Impact of population growth and climate change on the freshwater resources of Lamu Island, Kenya*, *Water*, 7 (2015) 1264-1290.
- [3] M.I. Osotsi, D.K. Macharia, B. Zhu, Z. Wang, X. Shen, Z. Liu, L. Zhang, Z. Chen, Synthesis of ZnWO<sub>4</sub>-x nanorods with oxygen vacancy for efficient photocatalytic degradation of tetracycline, *Progress in Natural Science: Materials International*, 28 (2018) 408-415.
- [4] M. El-Shahawi, A. Hamza, A. Bashammakh, W. Al-Saggaf, An overview on the accumulation, distribution, transformations, toxicity and analytical methods for the monitoring of persistent organic pollutants, *Talanta*, 80 (2010) 1587-1597.
- [5] A. Fiaz, D. Zhu, J. Sun, Environmental fate of tetracycline antibiotics: degradation pathway mechanisms, challenges, and perspectives, *Environmental Sciences Europe*, 33 (2021) 1-17.
- [6] R. Krishnan-Ayer, Heterogeneous photocatalytic treatment of organic dyes in air and aqueous media, *Journal of photochemistry and photobiology C: photochemistry reviews*, 9 (2008) 171-192.
- [7] M. Razavi-Esfali, T. Mahvelati-Shamsabadi, H. Fattahimoghaddam, B.-K. Lee, Highly efficient photocatalytic degradation of organic pollutants by mesoporous graphitic carbon nitride bonded with cyano groups, *Chemical Engineering Journal*, 419 (2021) 129503.
- [8] R. Dariani, A. Esmaeili, A. Mortezaali, S. Dehghanpour, Photocatalytic reaction and degradation of methyl orange on TiO<sub>2</sub> nano-sized particles, *Optik*, 127 (2016) 143-147.
- [9] T. Ahmad, M. Noorhad, Y. Alzharani, S.M. Alshahr, Photocatalytic degradation of bisphenol-A with g-C<sub>3</sub>N<sub>4</sub>/MoS<sub>2</sub>-PANI nanocomposite: kinetics, main active species, intermediates and pathways, *Journal of Molecular Liquids*, 311 (2020) 113339.
- [10] J.O. Tijani, M.E. Mouele, O.O. Fatoba, O.O. Babajide, L.F. Petrik, Degradation of bisphenol-A by dielectric barrier discharge system: influence of polyethylene glycol stabilized nano zero valent iron particles, *Advances in Natural Sciences: Nanoscience and Nanotechnology*, 8 (2017) 035013.
- [11] Y. Xiao, X. Liu, Y. Huang, W. Kang, Z. Wang, H. Zheng, Roles of hydroxyl and carbonate radicals in bisphenol a degradation via a nanoscale zero-valent iron/percarbonate system: influencing factors and mechanisms, *RSC Advances*, 11 (2021) 3636-3644.
- [12] G. Crini, E. Lichtfouse, Advantages and disadvantages of techniques used for wastewater treatment, *Environmental Chemistry Letters*, 19 (2021) 1-13.
- [13] E. Crini, A. Antonietti, D. Casarà, B. D'Amico, S. Garino, G. Canavese, S. Hernández, V. Cauda, Sonophotocatalytic degradation mechanisms of Rhodamine B dye via radicals generation by micro-and nano-particles of ZnO, *Applied Catalysis B: Environmental*, 243 (2019) 629-640.
- [14] M. Nie, Y. Li, F. He, C. Xie, Z. Wu, B. Sun, K. Zhang, J. Kong, J. Liu, Degradation of tetracycline in water using Fe<sub>3</sub>O<sub>4</sub> nanospheres as Fenton-like catalysts: kinetics, mechanisms and pathways, *New Journal of Chemistry*, 44 (2020) 2847-2857.

- [17] S. Rasalingam, R. Peng, R.T. Koodali, Removal of hazardous pollutants from wastewaters: applications of TiO<sub>2</sub>-SiO<sub>2</sub> mixed oxide materials, *Journal of Nanomaterials*, 2014 (2014).
- [18] X. Pang, N. Skillen, N. Gunaratne, D.W. Rooney, P.K. Robertson, Removal of phthalates from aqueous solution by semiconductor photocatalysis: A review, *Journal of Hazardous Materials*, 402 (2020) 123461.
- [19] J. Herrmann, Heterogeneous photocatalysis: fundamentals and applications to the removal of various types of aqueous pollutants, *Catalysis today*, 53 (1999) 113-129.
- [20] M. Melchionna, P. Ferrasiero, Updates on the road map for photocatalysis, *ACS Catalysis*, 10 (2020) 5203-5211.
- [21] Hoffmann, S.T. Martin, W. Choi, D.W. Bahnemann, Environmental applications of semiconductor photocatalysis, *Chemical reviews*, 95 (1995) 69-208.
- [22] A. Naseri, M. Samadi, A. Pourianadi, A.Z. Moshfagh, S. Ramabhisima, Graphitic carbon nitride (g-C<sub>3</sub>N<sub>4</sub>)-based photocatalysts for solar hydrogen generation: recent advances and future development directions, *Journal of Materials Chemistry A*, 5 (2017) 23406-23433.
- [23] J. Yu, J. Low, W. Xiao, P. Zhou, M. Jaroniec, Enhanced photocatalytic CO<sub>2</sub>-reduction activity of anatase TiO<sub>2</sub> by coexposed {001} and {101} facets, *Journal of the American Chemical Society*, 136 (2014) 8839-8842.
- [24] H. Wang, G. Chen, D.W. Bahnemann, Photoelectrocatalytic materials for environmental applications, *Journal of Materials Chemistry*, 16 (2006) 1719-1722.
- [25] H. Wang, Z. Wang, B. Huang, Y. Mao, Y. Jin, X. Qin, X. Zhang, Y. Dai, Oxygen vacancy induced band-gap narrowing and enhanced visible light photocatalytic activity of ZnO, *ACS applied materials & interfaces*, 4 (2012) 4024-4030.
- [26] H. Wang, K. Dou, W.Y. Teoh, Y. Zhan, T.F. Hung, F. Zhang, J. Xu, R. Zhang, A.L. Rogach, Engineering of facets, band structure, and gas-sensing properties of hierarchical Sn<sup>2+</sup>-doped SnO<sub>2</sub> nanostructures, *Advanced Functional Materials*, 23 (2013) 4847-4853.
- [27] H. Wang, A.L. Rogach, Hierarchical SnO<sub>2</sub> nanostructures: recent advances in design, synthesis, and applications, *Chemistry of Materials*, 26 (2014) 1391-1399.
- [28] T. Mishima, M. Matsuda, M. Miyake, Visible light photocatalytic properties and electronic structure of Zr-based oxynitride, Zr<sub>2</sub>ON<sub>2</sub>, derived from nitridation of ZrO<sub>2</sub>, *Applied Catalysis A: General*, 324 (2007) 77-82.
- [29] C. Shifu, Z. Sujuan, L. Wei, Z. Wei, Preparation and activity evaluation of p-n junction photocatalyst NiO/TiO<sub>2</sub>, *Journal of Hazardous Materials*, 155 (2008) 320-326.
- [30] F. Vahini, P.S. Kumar, S. Karuthanandian, Bandgap-tailored NiO nanospheres: an efficient photocatalyst for the degradation of crystal violet dye solution, *Applied Physics A*, 122 (2016) 18.
- [31] M. Kalaeir, M. Tayebi, B.-K. Lee, The synergistic effects of acid treatment and silver (Ag) loading for substantial improvement of photoelectrochemical and photocatalytic activity of Na<sub>2</sub>Ti<sub>3</sub>O<sub>7</sub>/TiO<sub>2</sub> nanocomposite, *Applied Surface Science*, 540 (2021) 148359.
- [32] Z. Masoumi, M. Tayebi, B.-K. Lee, The role of doping molybdenum (Mo) and back-front side illumination in enhancing the charge separation of α-Fe<sub>2</sub>O<sub>3</sub> nanorod photoanode for solar water splitting, *Solar Energy*, 205 (2020) 126-134.
- [33] L. Wang, T. Huang, G. Yang, C. Lu, F. Dong, Y. Li, W. Guan, The precursor-guided hydrothermal synthesis of CuBi<sub>2</sub>O<sub>4</sub>/WO<sub>3</sub> heterostructure with enhanced photoactivity under simulated solar light irradiation and mechanism insight, *Journal of hazardous materials*, 381 (2020) 120956.

- [38] J.V. Liebig, About some nitrogen compounds, *Ann. Pharm.* 10, 10.
- [39] E.C. Franklin, THE AMMONO CARBONIC ACIDS, *Journal of the American Chemical Society*, 44 (1922) 486-509.
- [40] J.H. Sturdivant, The Structure of Cyameluric Acid, Hydromelonic Acid and Related Substances, *Proc Natl Acad Sci U S A*, 23 (1937) 615-620.
- [41] R.S. Hosmane, M.A. Rossman, N.A. Leonard, Synthesis and structure of tri-s-triazine, *Journal of the American Chemical Society*, 104 (1982) 945-949.
- [42] D.M. Teter, P.J. Henry, Low-Compressibility Carbon Nitrides, *Science*, 271 (1996) 53-55.
- [43] E. Kroke, M. Schwarz, Novel group 14 nitrides, *Coordination Chemistry Reviews*, 248 (2004) 493-552.
- [44] F. Goettmann, A. Fischer, M. Antonietti, A. Thomas, Metal-free catalysis of sustainable Friedel–Crafts reactions: direct activation of benzene by carbon nitrides to avoid the use of metal chlorides and halogenated compounds, *Chemical communications*, (2006) 4530-4532.
- [45] X. Wang, K. Maeda, A. Thomas, K. Takane, G. Xin, J.M. Carlsson, K. Domen, M. Antonietti, A metal-free polymeric photocatalyst for hydrogen production from water under visible light, *Nature* 443 (2010) 79-83.
- [46] J. Wen, J. Xie, X. Chen, X. Li, A review on g-C<sub>3</sub>N<sub>4</sub>-based photocatalysts, *Applied surface science, materials*, 8 (2009) 76-80.
- [47] Y. Ma, J. Fan, Y. Xue, H. Chang, Y. Masubuchi, S. Yin, Synthesis of graphitic carbon nitride from different precursors by fractional thermal polymerization method and their visible light induced photocatalytic activities, *Journal of Alloys and Compounds*, 735 (2018) 1297-1305.
- [48] S. Cao, J. Low, J. Yu, M. Jaroniec, Polymeric photocatalysts based on graphitic carbon nitride, *Advanced Materials*, 27 (2015) 2150-2170.
- [49] M. J. O'Neil, J. Fan, S.-P. Chai, Graphitic Carbon Nitride (g-C<sub>3</sub>N<sub>4</sub>)-Based Photocatalysts for Artificial Photosynthesis and Environmental Remediation: Are We a Step Closer To Achieving Sustainability?, *Chemical Reviews*, 116 (2016) 7159-7329.
- [50] Y. Chen, X. Liu, L. Hou, X. Guo, R. Fu, J. Sun, Construction of covalent bonding oxygen-doped carbon nitride/graphitic carbon nitride Z-scheme heterojunction for enhanced visible-light-driven H<sub>2</sub> evolution, *Chemical Engineering Journal*, 383 (2020) 123132.
- [51] G. Song, Z. Chu, W. Jin, H. Sun, Enhanced performance of g-C<sub>3</sub>N<sub>4</sub>/TiO<sub>2</sub> photocatalysts for degradation of organic pollutants under visible light, *Chinese Journal of Chemical Engineering*, 23 (2015) 1326-1334.
- [52] Y. Markushyna, C.A. Smith, A. Savateev, Organic photocatalysis: carbon nitride semiconductors vs. molecular catalysts, *European Journal of Organic Chemistry*, (2020).
- [53] F. Li, J. Chen, J. Fan, Q. Xiao, Single-Atom Copper on amino-group enriched graphitic carbon nitride for photocatalytic CO<sub>2</sub> reduction, *ChemSusChem*, (2020).
- [54] S. Tonda, S. Kumar, S. Kandula, V. Shrober, Fe doped and mediated graphitic carbon nitride nanosheets for enhanced photocatalytic performance under natural sunlight, *Journal of Materials Chemistry A*, 2 (2014) 6772-6780.
- [55] M. Zhang, X. Bai, D. Liu, J. Wang, Y. Zhu, Enhanced catalytic activity of potassium-doped carbon nitride induced by low valence position, *Applied Catalysis B: Environmental*, 164 (2015) 77-84.
- [56] B. Shinde, B. Lin, B. Gao, Y. Chen, A facile approach to synthesize novel oxygen doped g-C<sub>3</sub>N<sub>4</sub> with superior visible light photoactivity, *Chemical Communications*, (2012) 12017-12019.
- [57] Y. Wang, Q. Wang, X. Zhang, F. Wang, M. Saffar, J. He, Visible light driven type II heterostructure g-C<sub>3</sub>N<sub>4</sub>/TiO<sub>2</sub> photocatalysis, *Chemical Communications*, (2012) 12017-12019.
- [58] D.A. Giannakopoulos, N.A. Travlou, I. Secor, T.J. Bandosz, Oxidized g-C<sub>3</sub>N<sub>4</sub> nanospheres as enhanced photocatalysis properties: a review, *Nanoscale*, 5 (2013) 8326-8339.
- [59] D.A. Giannakopoulos, N.A. Travlou, I. Secor, T.J. Bandosz, Oxidized g-C<sub>3</sub>N<sub>4</sub> nanospheres as catalytically photoactive linkers in MOF/g-C<sub>3</sub>N<sub>4</sub> composite of hierarchical pore structure, *Small*, 13 (2017) 1601758.

- [59] Z. Mo, H. Xu, Z. Chen, X. She, Y. Song, J. Wu, P. Yan, L. Xu, Y. Lei, S. Yuan, Self-assembled synthesis of defect-engineered graphitic carbon nitride nanotubes for efficient conversion of solar energy, *Applied Catalysis B: Environmental*, 225 (2018) 154-161.
- [60] O. Stroyuk, O. Raievska, D.R. Zahn, Graphitic carbon nitride nanotubes: a new material for emerging applications, *RSC Advances*, 10 (2020) 54059-54087.
- [61] H. Liu, J. Huang, H. Zhou, M. Antonietti, Uniform graphitic carbon nitride nanorod for efficient photocatalytic hydrogen evolution and sustained photoenzymatic catalysis, *ACS applied materials & interfaces*, 6 (2014) 8434-8440.
- [62] S. Yang, Y. Gong, J. Zhang, L. Zhan, L. Ma, Z. Fang, R. Vajtai, X. Wang, P.M. Ajayan, Exfoliated graphitic carbon nitride nanosheets as efficient catalysts for hydrogen evolution under visible light, *Advanced materials*, 25 (2013) 2452-2456.
- [63] Y. Fukasawa, K. Takanae, A. Shimojima, M. Antonietti, K. Domen, T. Okubo, Synthesis of ordered porous graphitic-C<sub>3</sub>N<sub>4</sub> and regularly arranged Ta<sub>3</sub>N<sub>5</sub> nanoparticles by using self-assembled silica nanospheres as a primary template, *Chemistry—An Asian Journal*, 6 (2011) 103-109.
- [64] X. Ma, L. Wang, Q. Zhang, H.L. Jiang, Switching on the photocatalysis of metal-organic frameworks by engineering structural defects, *Angewandte Chemie*, 131 (2019) 12303-12307.
- [65] Y. Jia, Z. Tang, J. Zhang, Z. Zhang, Defect engineering of air-treated WO<sub>3</sub> nanorods enhanced visible-light-driven photocatalytic hydrogen production, *Nano Energy*, 24 (2016) 65-71.
- [66] G. Zhang, W. Jiang, S. Hua, H. Zhao, L. Zhang, Z. Sun, Constructing bulk defective perovskite SrTiO<sub>3</sub> nanocubes for high-performance photocatalysts, *Nanoscale*, 8 (2016) 18965-18968.
- [67] S. Bai, N. Zhang, C. Gao, Y. Xiong, Defect engineering in photocatalytic materials, *Nano Energy*, 53 (2018) 296-336.
- [68] S. Cai, H. Li, H. Zhao, Synthesis g-C<sub>3</sub>N<sub>4</sub> of high specific surface area by precursor pretreatment strategy with SBA-15 as a template and their photocatalytic activity toward degradation of rhodamine B, Phosphorus, Sulfur, and Silicon and the Related Elements, 194 (2019) 229-235.
- [69] K. Nakata, D. Li, X. Wang, A. Fujishima, Q. Meng, New two-dimensional porous graphitic carbon nitride nanosheets for highly efficient photocatalytic hydrogen evolution under visible-light irradiation, *Catalysis Science & Technology*, 9 (2019) 3849-3857.
- [70] W. Liu, N. Iwasa, S. Fujita, H. Koizumi, M. Yamaguchi, T. Shimada, Porous graphitic carbon nitride nanoplates obtained by a combined exfoliation strategy for enhanced visible light photocatalytic activity, *Applied Surface Science*, 499 (2020) 143901.
- [71] C.-B. Chen, C.-X. Li, Y.-J. Zhang, Y.-J. Wang, J.-Y. Lu, H.-Q. Liu, W.-W. Li, Cyano-rich mesoporous carbon nitride nanospheres for visible-light-driven photocatalytic degradation of pollutants, *Environmental Science: Nano*, 5 (2018) 2966-2977.
- [72] L. Liang, L. Shi, F. Wang, H. Wang, W. Qi, The improvement of photocatalytic performance for hydrogen evolution over mesoporous g-C<sub>3</sub>N<sub>4</sub> modified with nitrogen defects, *Sustainable Energy & Fuels*, 4 (2020) 5179-5187.
- [73] W. Tu, Y. Xu, J. Wang, B. Zhang, T. Zhou, S. Yin, S. Wu, C. Li, Y. Huang, Y. Zhou, Z. Zou, J. Robertson, M. Kraft, R. Xu, Investigating the Role of Tunable Nitrogen Vacancies in Graphitic Carbon

Nitride Nanosheets for Efficient Visible-Light-Driven H<sub>2</sub> Evolution and CO<sub>2</sub> Reduction, ACS Sustainable Chemistry & Engineering, 5 (2017) 7260-7268.

- [76] J. Liu, W. Fang, Z. Wei, Z. Qin, Z. Jiang, W. Shangguan, Efficient photocatalytic hydrogen evolution on N-deficient g-C<sub>3</sub>N<sub>4</sub> achieved by a molten salt post-treatment approach, Applied Catalysis B: Environmental, 238 (2018) 465-470.
- [77] Y. Xue, Y. Guo, Z. Liang, H. Cui, J. Tian, Porous g-C(3)N(4) with nitrogen defects and cyano groups for excellent photocatalytic nitrogen fixation without co-catalysts, J Colloid Interface Sci, 556 (2019) 206-213.
- [78] L. Cui, J. Song, A.F. McGuire, S. Kang, X. Fang, J. Wang, C. Yin, X. Li, Y. Wang, B. Cui, Constructing Highly Uniform Onion-Ring-like Graphitic Carbon Nitride for Efficient Visible-Light-Driven Photocatalytic Hydrogen Evolution, ACS Nano, 12 (2018) 5551-5558.
- [79] B. Jürgens, E. Irran, J. Senker, P. Kroll, H. Müller, W. Schnick, Melem (2,5,8-Triamino-tri-s-triazine), an Important Intermediate during Condensation of Melamine Rings to Graphitic Carbon Nitride: Synthesis, Structure Determination by X-ray Powder Diffractometry, Solid-State NMR, and Theoretical Studies, J Chem Phys, 147 (2017) 044701.
- [80] K. R. Her, The chemistry of silica. Solubility, polymerization, colloid and surface properties and Structure Determination by X-ray Powder Diffractometry, Solid-State NMR, and Theoretical Studies, J Chem Phys, 147 (2017) 044701.
- [81] Y. S. Kim, S. Kim, K. H. Ahn, S. I. Lee, Dispersion stability and drying behavior of colloidal silica. Journal of the American Chemical Society, 125 (2003) 10288-10300.
- [82] A. Lesaine, Structural and mechanical properties of dried colloidal silica layers, in, 2018.
- [83] L. Lin, H. Ou, Y. Zhang, X. Wang, Tri-s-triazine-based crystalline graphitic carbon nitrides for highly efficient hydrogen evolution photocatalysis, ACS Catalysis, 8 (2018) 3924-3931.
- [84] J. Zheng, Y. Zheng, C. Chen, Y. Zhan, X. Liu, Q. Zheng, K. Wei, J. Zhu, Network Structured SnO<sub>2</sub>/ZnO Heterojunction Nanocatalyst with High Photocatalytic Activity, Inorganic Chemistry, 48 (2009) 1819-1825.
- [85] Y. Wang, Y. Li, W. Ju, J. Wang, H. Yao, L. Zhang, J. Wang, Z. Li, Molten salt synthesis of water-dispersible polymeric carbon nitride nanoseaweeds and their application as luminescent probes, Carbon, 102 (2016) 477-486.
- [86] J. Ran, T.Y. Ma, G. Gao, X.-W. Du, S.Z. Qiao, Porous P-doped graphitic carbon nitride nanosheets for synergistically enhanced visible-light photocatalytic H<sub>2</sub> production, Energy & Environmental Science, 8 (2015) 3708-3717.
- [87] J. Lei, B. Chen, W. Lv, L. Zhou, L. Wang, Y. Liu, J. Zhang, Robust Photocatalytic H<sub>2</sub>O<sub>2</sub> Production over Inverse Opal g-C<sub>3</sub>N<sub>4</sub> with Carbon Vacancy under Visible Light, ACS Sustainable Chemistry & Engineering, 7 (2019) 16467-16473.
- [88] S. Zhang, J. Li, X. Wang, Y. Huang, M. Zeng, J. Xu, In Situ Ion Exchange Synthesis of Strongly Coupled Ag@AgCl/g-C<sub>3</sub>N<sub>4</sub> Porous Nanosheets as Plasmonic Photocatalyst for Highly Efficient Visible-Light Photocatalysis, ACS Applied Materials & Interfaces, 6 (2014) 22116-22125.
- [89] S. Zhang, S. Song, P. Gu, R. Ma, D. Wei, G. Zhao, T. Wen, R. Jehan, B. Hu, X. Wang, Visible-light-driven activation of persulfate over cyano and hydroxyl group co-modified mesoporous g-C<sub>3</sub>N<sub>4</sub> for boosting bisphenol A degradation, Journal of Materials Chemistry A, 7 (2019) 5552-5560.
- [90] M. You, S. Yi, D. Xia, H. Jing, H. Ji, L. Zhang, Y. Wang, Z. Zhang, D. Chen, Bio-inspired SiO<sub>2</sub>-Hard-Template Reconstructed gC<sub>3</sub>N<sub>4</sub> Nanosheets for Enhanced Photocatalytic Hydrogen Evolution, Catalysis Science & Technology, (2020).
- [91] J. Yang, Y. Liang, K. Li, G. Yang, K. Wang, R. Xu, X. Xie, One-step synthesis of novel K<sup>+</sup> and cyano groups decorated triazine-/heptazine-based g-C<sub>3</sub>N<sub>4</sub> tubular homojunctions for boosting photocatalytic H<sub>2</sub> evolution, Applied Catalysis B: Environmental, 262 (2020) 118252.
- [92] G. Ge, Z. Zhao, Combining iodic acid and nitric acid to fabricate carbon nitride tubes for enhanced hydrogen evolution under visible light, Catalysis Science & Technology, 9 (2019) 266-270.



- [93] D. Zhao, C.L. Dong, B. Wang, C. Chen, Y.C. Huang, Z. Diao, S. Li, L. Guo, S. Shen, Synergy of dopants and defects in graphitic carbon nitride with exceptionally modulated band structures for efficient photocatalytic oxygen evolution, *Advanced Materials*, 31 (2019) 1903545.
- [94] Q. Zhao, L. Fu, D. Jiang, Y. Xi, H. Yang, A nanoclay-induced defective g-C<sub>3</sub>N<sub>4</sub> photocatalyst for highly efficient catalytic reactions, *Chemical Communications*, 54 (2015) 8259-8252.
- [95] W. Wang, H. Zhang, S. Zhang, Y. Liu, C. Wang, C. Sun, H. Zhu, Potassium-Ion-Assisted Regeneration of Active Cyano Groups in Carbon Nitride Nanoribbons: Visible-Light-Driven Photocatalytic Nitrogen Reduction, *Angewandte Chemie International Edition*, 58 (2019) 16644-16650.
- [96] Y. Tian, L. Zhou, Q. Zhu, J. Lei, L. Wang, J. Zhang, Y. Liu, Hierarchical macro-mesoporous g-C<sub>3</sub>N<sub>4</sub> with an inverse opal structure and vacancies for high-efficiency solar energy conversion and environmental remediation, *Nanoscale*, 11 (2019) 20638-20647.
- [97] X. Bu, Y. Bu, S. Yang, F. Sun, L. Tian, Z. Peng, P. He, J. Sun, T. Huang, X. Wang, Graphitic carbon nitride nanoribbon for enhanced visible-light photocatalytic H<sub>2</sub> production, *RSC advances*, 6 (2016) 112210-112214.
- [98] T. Huang, S. Pan, L. Shi, A. Yu, X. Wang, Y. Fu, Hollow porous prismatic graphitic carbon nitride with nitrogen vacancies and oxygen doping: a high-performance visible light-driven catalyst for nitrogen fixation, *Nanoscale*, 12 (2020) 1833-1841.
- [99] W. Tu, Y. Xu, J. Wang, B. Zhang, T. Zhou, S. Yin, S. Wu, C. Li, Y. Huang, Y. Zhou, Investigating the role of tunable nitrogen vacancies in graphitic carbon nitride nanosheets for efficient visible-light-driven H<sub>2</sub> evolution and CO<sub>2</sub> reduction, *ACS Sustainable Chemistry & Engineering*, 5 (2017) 7260-7268.
- [100] J. Zhang, J. Chen, Y. Wan, H. Liu, W. Chen, G. Wang, R. Wang, Defect engineering in atomic-layered graphitic carbon nitride for greatly extended visible-light photocatalytic hydrogen evolution, *ACS applied materials & interfaces*, 12 (2020) 13805-13812.
- [101] M. Wang, C. Fan, S. Yang, M. Liu, J. Luo, Y. Liu, L. Tang, Z. Gong, S. Leng, Nitrogen deficient carbon nitride for efficient visible light driven tetracycline degradation: a combination of experimental and DFT studies, *Catalysis Science & Technology*, 10 (2020) 6800-6808.
- [102] H.-X. Fang, H. Guo, C.-G. Niu, C. Liang, D.-W. Huang, N. Tang, H.-Y. Liu, Y.-Y. Yang, L. Li, Hollow tubular graphitic carbon nitride catalyst with adjustable nitrogen vacancy: Enhanced optical absorption and carrier separation for improving photocatalytic activity, *Chemical Engineering Journal*, 402 (2020) 126183.
- [103] Y. Zhang, J. Shi, Z. Xu, Y. Chen, D. Song, Degradation of tetracycline in a solar/H<sub>2</sub>O<sub>2</sub> system: Preparation mechanism and intermediates, *Chemosphere*, 202 (2018) 661-668.
- [104] M. Cao, B. Wang, Y. Ao, C. Wang, J. Hou, J. Qian, Visible light activated photocatalytic degradation of tetracycline by a magnetically separable composite photocatalyst: Graphene oxide/magnetite/cerium-doped titania, *Journal of Colloid and Interface Science*, 467 (2016) 129-139.
- [105] A. Sengupta, D. Sarkar, P. Das, S. Panja, C. Parikh, D. Ramanathan, S. Bagley, R. Datta, Tetracycline uptake and metabolism by vetiver grass (*Chrysopogon zizanioides* L. Nash), *Environmental Science and Pollution Research*, 23 (2016) 24880-24889.
- [106] J. Cao, L. Lai, B. Lai, G. Yao, X. Chen, L. Song, Degradation of tetracycline by peroxymonosulfate activated with zero-valent iron: performance, intermediates, toxicity and mechanism, *Chemical Engineering Journal*, 364 (2019) 45-56.
- [107] Y. Wang, H. Zhang, L. Chen, S. Wang, D. Zhang, Ozonation combined with ultrasound for the degradation of tetracycline in a rectangular air-lift reactor, *Separation and purification technology*, 84 (2012) 138-146.

- [108] D. Wang, J. Li, Z. Xu, Y. Zhu, G. Chen, Z. Cui, Synthesis of gC<sub>3</sub>N<sub>4</sub>/NiO p–n heterojunction materials with ball-flower morphology and enhanced photocatalytic performance for the removal of tetracycline and Cr<sup>6+</sup>, *Journal of Materials Science*, 54 (2019) 11417-11434.
- [109] X. Huang, M. Leal, Q. Li, Degradation of natural organic matter by TiO<sub>2</sub> photocatalytic oxidation
- [110] H. Wang, H. Yao, J. Pei, E. Liu, D. Li, Photodegradation of tetracycline antibiotics in aqueous solution by UV/ZnO, Desalination and Water Treatment, 57 (2016) 1999-2007.
- [111] W. B. Choz, C. H. Huang, Transformation of tetracyclines mediated by Mn(III) and Cu(II) ions in the presence of oxygen, *Environmental Science & Technology*, 45 (2011) 4014-4020.
- [112] Y. Wang, L. Rao, P. Wang, Z. Shi, L. Zhang, Photocatalytic activity of gC<sub>3</sub>N<sub>4</sub>-doped N vacancy g-C<sub>3</sub>N<sub>4</sub> and the intermediates toxicity evaluation under tetracycline hydrochloride and Cr(VI) coexistence
- [113] C. Yan, Y. Guo, P. Wang, L. Rao, X. Ji, Y. Guo, Improved photoremoval performance of boron carbon nitride–pyromellitic dianhydride composite toward tetracycline and Cr(vi) by itself to change the environment, *Applied Catalysis B: Environmental*, 262 (2020) 118308.
- [114] R.M. Yadav, R. Kumar, A. Aliyan, P.S. Dobal, S. Biradar, R. Vajtai, D.P. Singh, A.A. Marti, P.M. Ajayan, Facile synthesis of highly fluorescent free-standing films comprising graphitic carbon nitride (gC<sub>3</sub>N<sub>4</sub>) nanolayers, *New Journal of Chemistry*, 44 (2020) 2644-2651.
- [115] M. Zielińska, K. Bułkowska, A. Cydzik-Kwiatkowska, K. Bernat, I. Wojnowska-Baryła, Removal of bisphenol A (BPA) from biologically treated wastewater by microfiltration and nanofiltration, *International Journal of Environmental Science and Technology*, 13 (2016) 2239-2248.
- [116] C.G. Moreira, M.H. Moreira, V.M. Silva, H.G. Santos, D.M. Bila, F.V. Fonseca, Treatment of Bisphenol A (BPA) in water using UV/H<sub>2</sub>O<sub>2</sub> and reverse osmosis (RO) membranes: assessment of estrogenic activity and membrane adsorption, *Water Science and Technology*, 80 (2019) 2169-2178.
- [117] X. Pang, N. Skillen, N. Gunaratne, D.W. Rooney, P.K. Robertson, Removal of phthalates from aqueous solution by semiconductor photocatalysis: A review, *Journal of Hazardous Materials*, 402 (2021) 123461.
- [118] M. Tayebi, Z. Masoumi, B.-K. Lee, Ultrasonically prepared photocatalyst of W/WO<sub>3</sub> nanoplates with WS<sub>2</sub> nanosheets as 2D material for improving photoelectrochemical water splitting, *Ultrasonics Sonochemistry*, 70 (2021) 105339.
- [119] A. Tayyebi, M. Tayebi, A. Shafikhani, S.S. Şengör, ZnO quantum dots-graphene composites: Formation mechanism and enhanced photocatalytic activity for degradation of methyl orange dye, *Journal of Alloys and Compounds*, 663 (2016) 738-749.
- [120] A. Shoneye, J. Sen Chang, M.N. Chong, J. Tang, Recent progress in photocatalytic degradation of chlorinated phenols and reduction of heavy metal ions in water by TiO<sub>2</sub>-based catalysts, *International Materials Reviews*, (2021) 1-18.
- [121] P. Wang, J.Y. Zheng, D. Zhang, Y.S. Kang, Selective construction of junctions on different facets of BiVO<sub>4</sub> for enhancing photoactivity, *New Journal of Chemistry*, 39 (2015) 919-925.
- [122] W. Shen, W. Li, D. Tan, P. Zhang, E. Zhang, E. Shermat, B.V. Schmidt, X. Feng, E.D. Rodriguez, R. Jordan, Polymer brushes on graphitic carbon nitride for patterning and as a SERS active sensing layer
- [123] S. Wang, J. Zhang, B. Li, H. Sun, S. Wang, Engineered Graphitic Carbon Nitride-Based Photocatalysts for Visible Light-Driven Water Splitting: A Review, *Energy & Fuels*, 35 (2021) 6504-6526.
- (EDOT) via Graphitic Carbon Nitride: A Modular Toolbox for Attaining PEDOT, *ChemPhotoChem*, (2021).

- [125] N. Aquino de Carvalho, Y. Wang, N. Morales-Soto, D. Waldeck, K. Bibby, K. Doudrick, L.M. Gilbertson, Using C-Doping to Identify Photocatalytic Properties of Graphitic Carbon Nitride That Govern Antibacterial Efficacy, *ACS ES&T Water*, 1 (2020) 269-280.
- [126] L. Lin, T. Hisatomi, S. Chen, T. Takata, K. Domen, Visible-light-driven photocatalytic water splitting: recent progress and challenges, *Trends in Chemistry*, (2020).
- [127] T. Mahvelati Shamsabadi, B.-K. Lee, Photocatalytic H<sub>2</sub> evolution and CO<sub>2</sub> reduction over phosphorus-doped g-C<sub>3</sub>N<sub>4</sub> nanostructures: Electronic, Optical, and Surface properties, *Renewable and Sustainable Energy Reviews*, 130 (2020) 109957.
- [128] S. Wojtyła, K. Spiewak, T. Baran, Doped graphitic carbon nitride: Insights from spectroscopy and electrochemistry, *Journal of Inorganic and Organometallic Polymers and Materials*, 30 (2020) 3448-3478.
- dimensional heterojunction photocatalysts of stoichiometric and non-stoichiometric bismuth oxyhalides with graphitic carbon nitride for sustainable energy and environmental applications, *Catalysts*, 11 (2021) 4293.
- [130] J. Yang, H. Wang, L. Jiang, H. Yu, Y. Zhao, H. Chen, X. Yuan, J. Liang, H. Li, Z. Wu, Defective polymeric carbon nitride: Fabrications, photocatalytic applications and perspectives, *Chemical Engineering Journal*, (2021) 130991.
- [131] K. Pandi, S.K. Lakhera, B. Neppolian, Facile synthesis of nitrogen deficient graphitic carbon nitride for photocatalytic hydrogen production activity, *Materials Letters*, 303 (2021) 30467.
- [132] H. Fattahimoghadam, T. Mahvelati Shamsabadi, B.-K. Lee, Enhancement in Photocatalytic H<sub>2</sub>O<sub>2</sub> Production over g-C<sub>3</sub>N<sub>4</sub> Nanostructures: A Collaborative Approach of Nitrogen Deficiency and Supramolecular Precursors, *ACS Sustainable Chemistry & Engineering*, 9 (2021) 4520-4530.
- [133] H. Liu, D. Chen, Z. Wang, H. Jing, R. Zhang, Microwave-assisted molten-salt rapid synthesis of isotype triazine/heptazine based g-C<sub>3</sub>N<sub>4</sub> heterojunctions with highly enhanced photocatalytic hydrogen evolution performance, *Applied Catalysis B: Environmental*, 203 (2017) 300-313.
- [134] C. Zhou, R. Shi, S. Lu, W. Li-Zhu, T. Chen-Ho, T. Zhang, Template-free large-scale synthesis of gC<sub>3</sub>N<sub>4</sub> microtubes for enhanced visible light-driven photocatalytic H<sub>2</sub> production, *Nano Research*, 11 (2018) 3462-3468.
- [135] T. Jordan, N. Fechler, J. Xu, T.J. Brenner, M. Antonietti, M. Shalom, "Caffeine doping" of carbon/nitrogen-based organic catalysts: Caffeine as a supramolecular edge modifier for the synthesis of photoactive carbon nitride tubes, *ChemCatChem*, 7 (2015) 2826-2830.
- [136] Q. Liang, B. Shao, S. Tong, Z. Liu, L. Tang, Y. Liu, M. Cheng, Q. He, T. Wu, Y. Pan, Recent advances of melamine self-assembled graphitic carbon nitride-based materials: design, synthesis and application in energy and environment, *Chemical Engineering Journal*, (2020) 126951.
- [137] S.I. Stupp, L.C. Palmer, Supramolecular chemistry and self-assembly in organic materials design, *Chemistry of Materials*, 26 (2014) 507-518.
- [138] T. Huang, W. Zhang, S. Pan, L. Zhu, X. Wang, Y. Fu, General synthesis strategy for hollow porous prismatic graphitic carbon nitride: a high-performance photocatalyst for H<sub>2</sub> production and degradation of RhB, *Journal of Materials Science*, 55 (2020) 6037-6050.
- [139] J. Barrio, M. Shalom, Rational design of carbon nitride materials by supramolecular preorganization of monomers, *ChemCatChem*, 10 (2018) 5274-5286.
- [140] Y. Li, X. Chen, Q. Xiang, H. Zhang, H. Wang, J. Zhang, Y. Liu, Hierarchical macro-mesoporous gC<sub>3</sub>N<sub>4</sub> nanoscale horizons, *Nanoscale*, 5 (2013) 765-786.
- [141] Y. Tian, F. Zhou, Q. Zhu, J. Li, K. Wang, J. Zhang, Y. Liu, Hierarchical macro-mesoporous gC<sub>3</sub>N<sub>4</sub> with an inverse opal structure and vacancies for high-efficiency solar energy conversion and environmental remediation, *Nanoscale*, 11 (2019) 20638-20647.

- [142] J. Gao, J. Song, J. Ye, X. Duan, D.D. Dionysiou, J.S. Yadav, M.N. Nadagouda, L. Yang, S. Luo, Comparative toxicity reduction potential of UV/sodium percarbonate and UV/hydrogen peroxide treatments for bisphenol A in water: An integrated analysis using chemical, computational, biological, and metabolomic approaches, *Water Research*, 190 (2021) 116755.
- [143] T. Mahvelati-Shamsabadi, H. Fattahimoghaddam, B.-K. Lee, S. Bae, J. Ryu, Synthesis of hexagonal rosettes of g-C<sub>3</sub>N<sub>4</sub> with boosted charge transfer for the enhanced visible-light photocatalytic hydrogen evolution and hydrogen peroxide production, *Journal of Colloid and Interface Science*, 597 (2021) 345-360.
- [144] B. Lin, G. Yang, B. Yang, Y. Zhao, Construction of novel three dimensionally ordered macroporous carbon nitride for highly efficient photocatalytic activity, *Applied Catalysis B: Environmental*, 198 (2016) 276-285.
- [145] S. Zhang, H.M. Kwon, Z. Li, A. Ikoma, K. Dokko, M. Watanabe, Nitrogen-Doped Inverse Opal Carbons Derived from an Ionic Liquid Precursor for the Oxygen Reduction Reaction, *ChemElectroChem*, 2 (2015) 1080-1085.
- [146] T. Mahvelati-Shamsabadi, B.-K. Lee, Design of Ag/g-C<sub>3</sub>N<sub>4</sub> on TiO<sub>2</sub> nanotree arrays via ultrasonic-assisted spin coating as an efficient photoanode for solar water oxidation: Morphology modification and junction improvement, *Catalysis Today*, 358 (2020) 412-421.
- [147] C. Zhao, Q. Li, Y. Xie, L. Zhang, X. Xiao, D. Wang, Y. Jiao, C.A.H. Price, B. Jiang, J. Liu, Three-dimensional assemblies of carbon nitride tubes as nanoreactors for enhanced photocatalytic hydrogen production, *Journal of Materials Chemistry A*, 8 (2020) 305-312.
- [148] S. Wan, M. Ou, Q. Zhong, W. Cai, Haloid acid induced carbon nitride semiconductors for enhanced photocatalytic H<sub>2</sub> evolution and reduction of CO<sub>2</sub> under visible light, *Carbon*, 138 (2018) 463-474.
- [149] Y. Zhang, H. Gao, Z. Chen, A solid-state electrochemical reduction approach to synthesize graphitic carbon nitride with tunable nitrogen defects for efficient visible-light photocatalytic hydrogen evolution, *Journal of Colloid and Interface Science*, 535 (2019) 331-340.
- [150] F. Li, X. Yue, H. Zhou, J. Fan, Q. Xiang, Construction of efficient active sites through cyano-modified graphitic carbon nitride for photocatalytic CO<sub>2</sub> reduction, *Chinese Journal of Catalysis*, 42 (2021) 1608-1616.
- [151] L. Muniandy, F. Adam, A.R. Mohamed, A. Iqbal, N.R.A. Rahman, Cu<sup>2+</sup> coordinated graphitic carbon nitride (Cu-g-C<sub>3</sub>N<sub>4</sub>) nanosheets from melamine for the liquid phase hydroxylation of benzene and VOCs, *Applied Surface Science*, 398 (2017) 43-55.
- [152] A. Jin, Y. Jia, C. Chen, X. Liu, J. Jiang, X. Chen, F. Zhang, Efficient photocatalytic hydrogen evolution on band structure tuned polytriazine/heptazine based carbon nitride heterojunctions with ordered needle-like morphology achieved by an in situ molten salt method, *The Journal of Physical Chemistry C*, 121 (2017) 21497-21509.
- [153] T. Mahvelati-Shamsabadi, H. Fattahimoghaddam, B.-K. Lee, H. Ryu, J. Jang, Caesium sites coordinated in Boron-doped porous and wrinkled graphitic carbon nitride nanosheets for efficient charge carrier separation and transfer: Photocatalytic H<sub>2</sub> and H<sub>2</sub>O<sub>2</sub> production, *Chemical Engineering Journal*, 425 (2021) 130097.
- [154] L. Chen, X. Zhao, X. Duan, J. Zhang, Z. Ao, P. Li, S. Wang, Y. Wang, S. Cheng, H. Zhao, Graphitic carbon nitride microtubes for efficient photocatalytic overall water splitting: The morphology derived electrical field enhancement, *ACS Sustainable Chemistry & Engineering*, 8 (2020) 14386-14396.
- [155] H. Ma, Y. Jia, G. Zhu, F. Zhang, S. Rhee, B. Lee, C. Liu, Study of cyano and hydroxyl groups modification on the properties of porous carbon nitride synthesized by using a salt assistant method, *Applied Surface Science*, 507 (2020) 144885.
- [156] J. Ding, W. Xu, H. Wan, D. Yuan, C. Chen, L. Wang, G. Guan, W.-L. Dai, Nitrogen vacancy engineered graphitic C<sub>3</sub>N<sub>4</sub>-based polymers for photocatalytic oxidation of aromatic alcohols to aldehydes, *Applied Catalysis B: Environmental*, 221 (2018) 626-634.
- [157] C. Chuaicham, K. Sekar, Y. Xiong, V. Balakumar, Y. Mittraphab, K. Shimizu, B. Ohtani, I. Dabo, K. Sasaki, Single-step synthesis of oxygen-doped hollow porous graphitic carbon nitride for photocatalytic ciprofloxacin decomposition, *Chemical Engineering Journal*, (2021) 130502.

- [158] Z. Zhao, Y. Sun, Q. Luo, F. Dong, H. Li, W.-K. Ho, Mass-controlled direct synthesis of graphene-like carbon nitride nanosheets with exceptional high visible light activity. *Scientific reports*, [159] A.N. Oliveros, J.A.I. Pimentel, M.D.G. de Luna, S. Garcia-Segura, R.R.M. Abarca, R.-A. Doong, 5 (2015) 1-15.
- Visible-light photocatalytic diclofenac removal by tunable vanadium pentoxide/boron-doped graphitic carbon nitride composite, *Chemical Engineering Journal*, 403 (2021) 126213.
- Toward a visible light-driven photocatalyst: the effect of midgap-states-induced energy gap of undoped TiO<sub>2</sub> nanoparticles, *Acs Catalysis*, 5 (2015) 327-335.
- [160] H. Yaghoubi, Z. Li, Y. Chen, H.T. Ngo, V.R. Bhethanabotla, B. Joseph, S. Ma, R. Schlaf, A. Takshi, electron transition of porous P-doped g-C<sub>3</sub>N<sub>4</sub> nanosheets for improved photocatalytic H<sub>2</sub> evolution
- [161] C. Su, Y. Zhou, L. Zhang, X. Yu, S. Gao, X. Sun, C. Cheng, Q. Liu, J. Yang, Enhanced n→π\* performance, *Ceramics International*, 46 (2020) 8444-8451.
- [162] A. Meng, Z. Teng, Q. Zhang, C. Su, Intrinsic Defects in Polymeric Carbon Nitride for Photocatalysis Applications, *Chemistry - An Asian Journal*, 15 (2020) 3405-3419.
- loading on photodegradation efficiency of urea derived graphitic carbon nitride towards methylene blue [164] T. Li, P. Zhang, H. He, Z. Wang, X. Tu, D.D. Dionysiou, Highly efficient photoelectrocatalytic dye solution, *RSC Advances*, 9 (2019) 15381-15391.
- degradation of cefotaxime sodium on the MoSe<sub>2</sub>/TiO<sub>2</sub> nanotubes photoanode with abundant oxygen [165] A. Akhundi, A. Badiei, G.M. Ziarani, A. Habibi-Yangjeh, M.J. Muñoz-Batista, R. Luque, Graphitic vacancies, *Journal of Solid State Chemistry*, (2021) 122455.
- carbon nitride-based photocatalysts: toward efficient organic transformation for value-added chemicals [166] M. Wu, X. He, B. Jing, T. Wang, C. Wang, Y. Qin, Z. Ao, S. Wang, T. An, Novel carbon and defects production, *Molecular Catalysis*, 488 (2020) 110902.
- co-modified g-C<sub>3</sub>N<sub>4</sub> for highly efficient photocatalytic degradation of bisphenol A under visible light, [167] A. Kondrakov, A. Ignatev, F. Frimmel, S. Bräse, H. Horn, A. Revelsky, Formation of genotoxic quinones during bisphenol A degradation by TiO<sub>2</sub> photocatalysis and UV photolysis: a comparative study, *Journal of hazardous materials*, 384 (2020) 121323.
- [168] D. Li, X. Zhang, W. Zhang, Designing a new reaction system by stacking use of Ti mesh supported Applied Catalysis B: Environmental, 160 (2014) 106-114.
- Ag/N-TiO<sub>2</sub> nano-sheets for enhanced photocatalytic degradation of bisphenol A, *Chemical Engineering Journal*, 405 (2021) 126867.
- [169] X. Dong, B. Ren, Z. Sun, C. Li, X. Zhang, M. Kong, S. Zheng, D.D. Dionysiou, Monodispersed CuFe<sub>2</sub>O<sub>4</sub> nanoparticles anchored on natural kaolinite as highly efficient peroxydisulfate catalyst for bisphenol A degradation, *Applied Catalysis B: Environmental*, 253 (2019) 206-217.
- [170] W.H. Abdelraheem, M.K. Patil, M.N. Nadagouda, D.D. Dionysiou, Hydrothermal synthesis of photoactive nitrogen-and boron-codoped TiO<sub>2</sub> nanoparticles for the treatment of bisphenol A in wastewater: Synthesis, photocatalytic activity, degradation byproducts and reaction pathways, *Applied Catalysis B: Environmental*, 241 (2019) 598-611.
- [171] E. Ioannidou, A. Ioannidi, Z. Frontistis, M. Antonopoulou, C. Tselios, D. Tsikritzis, I. Konstantinou, S. Kennou, D.I. Kondarides, D. Mantzavinos, Correlating the properties of hydrogenated titania to reaction kinetics and mechanism for the photocatalytic degradation of bisphenol A under solar irradiation, *Applied Catalysis B: Environmental*, 188 (2016) 65-76.
- [172] X. Xu, S. Zong, W. Chen, D. Liu, Comparative study of Bisphenol A degradation via heterogeneously catalyzed H<sub>2</sub>O<sub>2</sub> and persulfates reactivity, products, stability and mechanism, *Chemical Engineering Journal*, 369 (2019) 470-479.
- [173] J. Peng, L. Lai, X. Jiang, W. Jiang, B. Lai, Catalytic ozonation of succinic acid in aqueous solution using the catalyst of Ni/Al<sub>2</sub>O<sub>3</sub> prepared by electroless plating-calcination method, *Separation and Purification Technology*, 195 (2018) 138-148.

- [174] X. Li, Z. Wang, B. Zhang, A.I. Rykov, M.A. Ahmed, J. Wang, Fe<sub>x</sub>Co<sub>3-x</sub>O<sub>4</sub> nanocages derived from nanoscale metal–organic frameworks for removal of bisphenol A by activation of peroxymonosulfate, *Applied Catalysis B: Environmental*, 181 (2016) 788-799.
- [175] H. Chen, Y. Xu, K. Zhu, H. Zhang, Understanding oxygen-deficient La<sub>2</sub>CuO<sub>4-δ</sub> perovskite activated peroxymonosulfate for bisphenol A degradation: The role of localized electron within oxygen vacancy, *Applied Catalysis B: Environmental*, 284 (2021) 119732.
- [176] C.-Y. Wang, X. Zhang, H.-B. Qiu, W.-K. Wang, G.-X. Huang, J. Jiang, H.-Q. Yu, Photocatalytic degradation of bisphenol A by oxygen-rich and highly visible-light responsive Bi<sub>12</sub>O<sub>17</sub>Cl<sub>2</sub> nanobelts, *Applied Catalysis B: Environmental*, 200 (2017) 659-665.
- [177] L. Jing, M. He, M. Xie, Y. Song, W. Wei, Y. Xu, H. Xu, H. Li, Realizing the synergistic effect of electronic modulation over graphitic carbon nitride for highly efficient photodegradation of bisphenol A, *Applied Catalysis B: Environmental*, 200 (2017) 659-665.
- [178] L. Wang, J. Jiang, S.-Y. Pang, Y. Zhou, J. Li, S. Sun, Y. Gao, C. Jiang, Oxidation of bisphenol A by and 2-mercaptobenzotriazole: Mechanism, degradation pathway and density functional theory calculation, *Journal of Colloid and Interface Science*, 583 (2021) 115-127.
- [179] B. Perić, J. Sierra, E. Martí, R. Cruañas, M.A. Garau, Quantitative structure–activity relationship (QSAR) prediction of (eco) toxicity of short aliphatic protic ionic liquids, *Ecotoxicology and environmental Engineering Journal*, 352 (2018) 1004-1013.
- [180] Z. Li, F. Wang, Y. Zhang, Y. Lai, Q. Fang, Y. Duan, Activation of peroxymonosulfate by CuFe<sub>2</sub>O<sub>4</sub>-safety, 115 (2015) 257-262.
- [181] J. Lin, Y. Hu, L. Wang, D. Liang, X. Ruan, S. Shao, M88/PS/Vis system for degradation of bisphenol A: Environmental factors, degradation pathways, and toxicity evaluation, *Chemical Engineering Journal*, 423 (2021) 130093.
- [182] Y. Zhou, J. He, J. Lu, Y. Liu, Y. Zhou, Enhanced removal of bisphenol A by cyclodextrin in photocatalytic systems: degradation intermediates and toxicity evaluation, *Chinese Chemical Letters*, 31 (2020) 2623-2626.
- [183] R. Bhalla, R. Tehrani, B. Van Aken, Toxicity of hydroxylated polychlorinated biphenyls (HO-PCBs) using the bioluminescent assay Microtox®, *Ecotoxicology*, 25 (2016) 1438-1444.